EXPERIMENTAL STUDY OF NANOMAGNETS FOR MAGNETIC QUANTUM-DOT CELLULAR AUTOMATA (MQCA) LOGIC APPLICATIONS

A Dissertation

Submitted to the Graduate School

of the University of Notre Dame

in Partial Fulfillments of the Requirements

for the Degree of

Doctor of Philosophy

by

Alexandra Imre, M.S.

_____

Wolfgang Porod, Director

_____

Gary H. Bernstein, Co-director

Graduate Program in Electrical Engineering

Notre Dame, Indiana

April 2005

EXPERIMENTAL STUDY OF NANOMAGNETS FOR MAGNETIC QUANTUM-DOT CELLULAR AUTOMATA (MQCA) LOGIC APPLICATIONS

Abstract

By

Alexandra Imre

Nanomagnets that exhibit only two stable states of magnetization can represent digital bits. Magnetic random access memories store binary information in such nanomagnets, and currently, fabrication of dense arrays of nanomagnets is also under development for application in hard disk drives. The latter faces the challenge of avoiding magnetic dipole interactions between the individual elements in the arrays, which limits data storage density. On the contrary, these interactions are utilized in the magnetic quantum-dot cellular automata (MQCA) system, which is a network of closely-spaced, dipole-coupled, single-domain nanomagnets designed for digital computation. MQCA offers very low power dissipation together with high integration density of functional devices, as QCA implementations do in general. In addition, MQCA can operate over a wide temperature range from sub-Kelvin to the Curie temperature. Information propagation and inversion have previously been demonstrated in MQCA. In this dissertation, room temperature operation of the basic MQCA logic gate, i.e. the three-input majority gate, is demonstrated for the first time.

The samples were fabricated on silicon wafers by using electron-beam lithography for patterning thermally evaporated ferromagnetic metals. The networks of nanomagnets were imaged by magnetic force microscopy (MFM), with which individual magnetization states were distinguished and mapped. Magnetic dipole-ordering in the networks was investigated in different samples. Average ordering lengths were calculated by statistical analysis of the MFM images taken after several independent demagnetization processes.

The average ordering length was found to be dependent on the shape and size of the nanomagnets and limited by defects introduced during fabrication. Defect tolerant shape-design was investigated in samples of many different ring-shaped and elongated nanomagnets. The shape-effects were explained by means of micromagnetic simulations.

The majority gate was demonstrated by employing NiFe polycrystalline nanomagnets with 70 nm x 120 nm lateral sizes. Inputs were provided by additional nanomagnets fabricated together with the gate, and the operation was tested by MFM.

The work presented here is an experimental proof of the MQCA concept. The theoretical calculations can be found in the dissertation of György Csaba.[#]

[#] György Csaba, "Computing with field-coupled nanomagnets," PhD dissertation, University of Notre Dame, 2004.

CONTENTS

FIGURES

SYMBOLS

A	Exchange stiffness
$\mathbf{B}$	Magnetic induction
c_L	Spring constant
$\mathbf{E}$	Energy
E	Energy density
F	Force
$\mathbf{H}$	Magnetic field
H_C	Coercivity field
H_{Ci}	Intrinsic coercivity field
$\mathbf{H}_{eff}$	Effective magnetic field
J	Dipolar coupling energy
k	Boltzmann's constant
K_1	Magneto-crystalline anisotropy
K_U	Induced uniaxial anisotropy
l_{exch}	Exchange length
m	mass
$\mathbf{M}(\mathbf{r}, t)$	Magnetization distribution
M_R	Remanent magnetization
M_S	Saturation magnetization
$\mathbf{r}$	Spatial position

t	Time
T	Temperature
T_C	Curie temperature
α	Damping constant of the Landau-Lifshitz equation
γ	Gyromagnetic ratio
δ_{BW}	Width of the Bloch wall
ε_0	Vacuum permittivity
λ_S	Magnetostriction
μ_0	Vacuum permeability

ACKNOWLEDGMENTS

Firstly, I would like to thank to my advisors, Prof. Wolfgang Porod and Prof. Gary H. Bernstein. Their guidance and support made me successful in scientific research.

I would like to thank kindly the members of our research group: Dr. Alexei Orlov, Dr. György Csaba and Ms. Lili Ji, for their help with my experiments, and for their contribution to the research on MQCA.

I am grateful to the welcoming "magnetic" community, with special thanks to Vitali Metlushko at Univ. of Illinois at Chicago and Peter Kappenberger at EMPA, Switzerland, for the test-samples and for the discussions.

I would like to acknowledge the National Science Foundation, the W. M. Keck Foundation and the Office of Naval Research whose financial support made this research possible.

Finally, I would like to thank all the members of our community, from whom I got infinite support during my stay at Notre Dame.

CHAPTER 1

MOTIVATION

The magnetic quantum-dot cellular automata concept is a version of the field-coupled QCA architecture that was first proposed in [1]. The original idea was introduced for a quantum dot system, in which electrons tunnel between the quantum dots under the influence of repelling Coulomb forces. The basic QCA geometries and their functions are shown in Fig. 1.1. An elementary building block contains four quantum dots in a square arrangement, having one dot in each corner. With two electrons in the four-dot cell, two stable states are defined by the configuration of the electrons as they occupy the corners of the squares along the diagonals. Electron tunneling occurs only inside the cells, and the neighboring boxes are coupled by long-range electrostatic fields. This architecture can propagate and process binary information when a feasible clocking method is applied [2].

From a more general point of view, the field-coupled QCA architecture is a signal processing system built from simple, identical, bistable units that are locally connected to each other solely by electromagnetic forces; consequently, the signal processing function is defined by the placement of the building blocks and their physical interactions. The QCA concept can be realized in different physical systems.

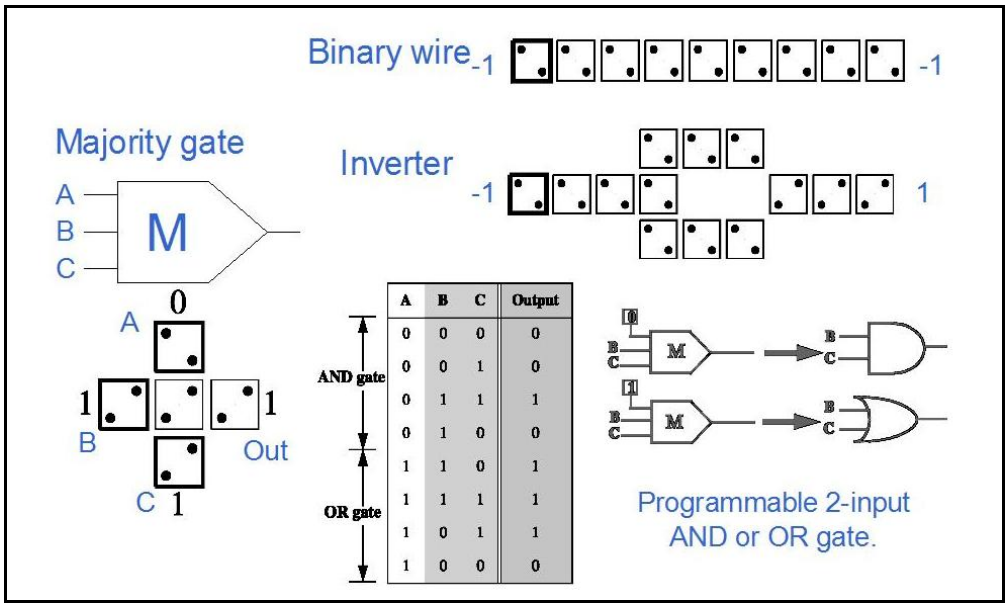

Figure 1.1 Quantum-dot cellular automata devices.

The first experimental demonstration of a working electronic QCA cell was published in 1997 [3], the logic gate in 1999 [4], and the shift register in 2003 [5], by the same group at the University of Notre Dame. In this approach, the quantum dots are realized by aluminum islands that are separated by a few-nanometer thick layer of aluminum oxide. Good agreement with the theoretical results was demonstrated at 50 mK. Room temperature operation is expected only when the sizes are reduced to the molecular scale [6], however the realization of molecular QCA requires more advanced fabrication technology.

We proposed to realize the QCA concept using ferromagnetic dots and magnetic field coupling in 2002 [7][8]. As an advantage compared to the above mentioned electrostatic devices, logic gates featuring single-domain magnets in the size scale of 100 nm are expected to operate at room temperature, because of the relatively high energy coupling energy.

CHAPTER 2

MAGNETIC LOGIC DEVICES

Ferromagnetic materials have been considered for applications in digital computing since the appearance of the first magnetic memory device. As is very well summarized by Hans Gschwind in his book "Design of digital computers" published in 1967 [9], "magnetic components are rather attractive to the computer designer for several reasons:

- They possess an inherent high reliability.
- They require in most applications no power other than the power to switch their state.
- They are potentially able to perform all required operations, i.e., logic, storage and amplification."

The key feature of such ferromagnetic components is magnetic hysteresis, which describes the internal magnetization of the components as a function of external magnetizing force and magnetization history. Hysteresis curves may take a variety of different forms, and many non-trivial aspects contribute to the picture of the underlying physical mechanism. A schematic hysteresis loop is shown in Fig. 2.1.

Nearly all applications rely heavily on particular aspects of hysteresis. A number of primary magnetic properties of a component can be determined from its hysteresis loop:

- The saturation magnetization is the magnetization value when magnetizing the material fully with a magnetizing force.

- The remanent magnetization, or remanence, is the magnetization value that remains in a material when the magnetizing force is zero. The remanent magnetization is called retentivity when the material has been magnetized to the saturation point. The level of residual magnetism may be lower than the retentivity value when the magnetizing force did not reach the saturation level.

- The coercive field, or coercivity, is the amount of reverse magnetic field that must be applied to a magnetic material to make the magnetic flux return to zero. Soft magnetic materials have small coercive fields compared to other magnetic materials.

- The permeability (μ) is a property that describes the ease of establishing a magnetic flux in the component. It is the ratio B/H:

$$\mathbf{B} = \mu_0\mu_R\mathbf{H} = \mu_0(\mathbf{H}+\mathbf{M}) \qquad (2.1)$$

where **B** is the magnetic flux density vector, (units: $1T = 10^4$ G,)
H is the magnetic field strength vector, (units: $1\ A/m = 4\pi 10^{-3}$ Oe,)
M is the magnetization vector, (units: $1\ A/m = 10^{-3}$ emu/cm^3,)
$\mu_0 = 4\pi 10^{-7}$ H/m is the permeability of free space, and μ_R is the relative permeability.

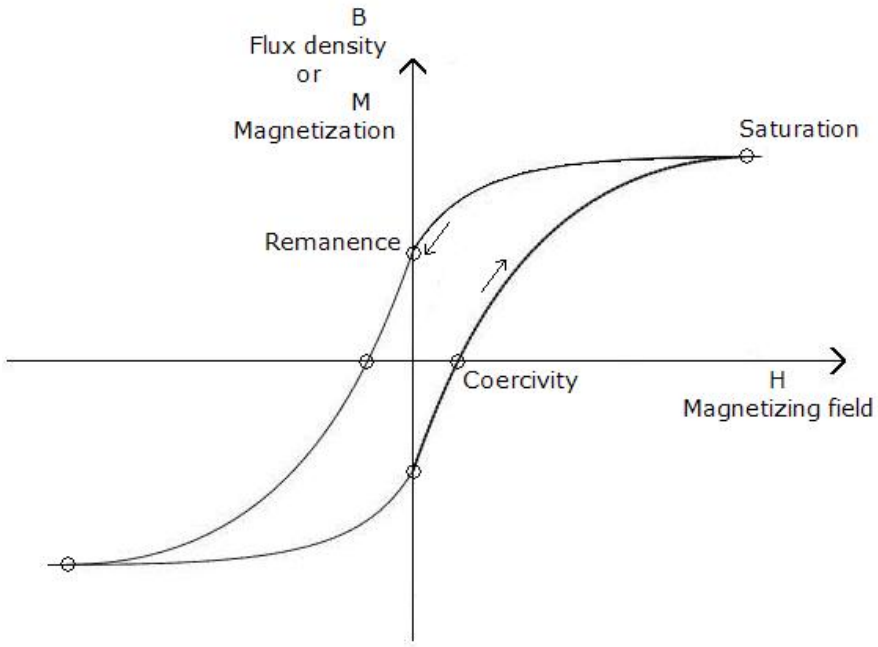

Figure 2.1 Magnetic hysteresis curve B vs. H, or M vs. H is a property of ferromagnetic materials.

The field of magnetostatics was extensively studied in the last two centuries because of the early applications of magnetic materials in simple machines. The accumulated knowledge then was able to provide magnetic components for the early stage of digital computing.

Prior to integrated circuit technology, data in a computer was stored using magnetic cores. Cores were generally constructed by two methods. The first, called a tape wound core, was fabricated by wrapping a magnetic tape around a nonmagnetic toroidal form. The second, called a ferrite core, was made by molding finely ground ferrite (a ceramic iron oxide) into a toroidal form. Magnetic core memories were constructed by threading current-carrying copper wires through the apertures of the cores, and arranging the approximately 1 mm diameter rings into an array. Current pulses through the wires were able to set the magnetization of the cores to clockwise or counter clockwise directions, which represented the binary information 0 and 1. The operation principle of the device was similar to today's random access memories (RAM). The core memories became widely used in computers by the early sixties, but even after the rise of silicon, they were utilized in certain critical applications (for example NASA used ferrite core memories until 1991). The cores were also investigated for logic applications. A review can be found in Gschwind's book [9], page 460. The core is introduced as a magnetic amplifier, and logic gates and shift registers constructed from several cores are explained. An alternative physical variation of cores with additional apertures, called a "transfluxor," is also described. The multi-aperture transfluxors were developed mainly by Hew Crane, working from the notion of controlling the direction of bit flow to achieve complete logic capability. Crane introduced the basic all-magnetic logic approach at the Fall Joint

Computer Conference in 1959. In 1961, the world's first, and only, all-magnetic computer with multi-aperture core logic system was demonstrated [10].

While magnetic cores are individual magnetic elements, one can think of a continuous magnetic medium that could host a whole memory or logic device if the digital information were represented and conserved in restricted volumes of the medium. Such volumes can be uniformly magnetized regions, called magnetic domains, which are separated from each other by regions where the magnetization vector rotates from the magnetization direction of one domain to the other, called domain walls. The most prominent domain walls, the 180º Bloch and the 180º Néel wall are depicted in Fig. 2.2. The type of the domain walls, as well as the preferred direction of the magnetic domains depends on magnetic anisotropies of the actual material system.

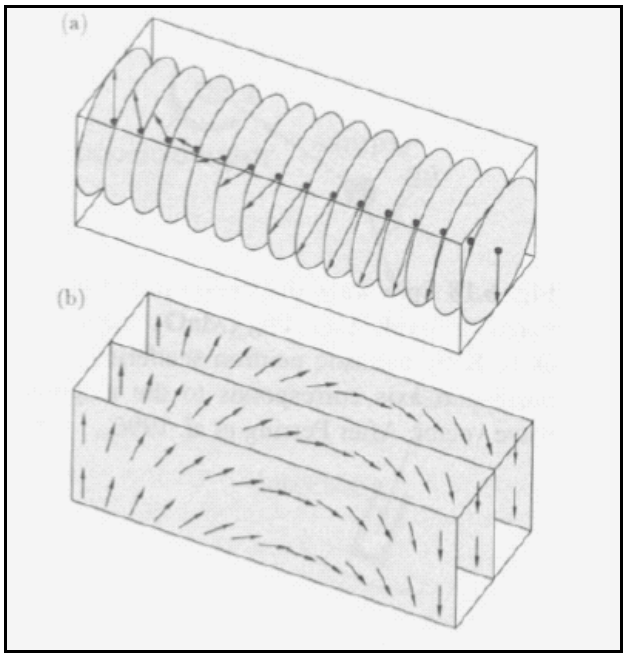

Figure 2.2 (a) Bloch wall. (b) Néel wall. From Hubert and Schafer [11], page 216.

For instance, in thin films with strong out-of-plane anisotropy, magnetic stripe-domains evolve spontaneously guided by energy minimization within otherwise unstructured samples. Such materials include garnets, orthoferrites and hexaferrites, which were studied exhaustively for application in magnetic bubble technology. Magnetic bubbles are cylindrical domains of reversed magnetization in the thin film. Individual bubbles can be created in the film either by locally creating a vertical magnetic field strong enough to reverse the magnetization, or by spawning a secondary bubble from a seed bubble. Information can be represented then by the presence or absence of "isolated" bubbles or in a dense array of bubbles by different bubble "states". This was the main idea of the research on magnetic bubble memories in the late 60s [12]. Memory is provided here in that the bubbles persist as long as there is a static magnetic field present and in that there is latitude in the magnitude of that field provides necessary tolerances. Bubbles can be propelled by creating a gradient in the bias field along the film. Bubbles move into the region of lower bias, since the field is opposite to the bubble magnetization and the magnetic energy decreases by the bubble movement. The gradient in the bias field can be created by current carrying conductors on the surface of the film. Continuous propagation can then be achieved by alternating pulses in an array of conductors. In most devices, however, propagation was done by coupling a rotating in-plane field to a track of permalloy bars which came in a variety of shapes.

Bubbles might also be used to perform logic, but the storage application was more obvious and was the only one that received significant attention.

The scheme of propagating domain walls in a rotating external magnetic field is employed by a contemporary research project as well. Professor Cowburn's group

previously at the University of Durham, UK, and presently at the Imperial College London, UK, is working on specially designed loops of permalloy wires, inside which head-to-head and tail-to-tail domain walls are swept around [13][14]. Logic functionality is coded in the geometrical design of the wire loops.

Finally, another contemporary work that uses single-domain nanomagnets as basic components should be mentioned. The proposed architecture, by Ney in [15], describes a programmable logic element that is based on a single magnetic random access memory (MRAM) cell. It combines the inherent advantage of a non-volatile output, with flexible functionality that can be selected at run-time to operate as an AND, OR, NAND or NOR gate. This is an alternative approach to enhance computational power considering magneto-electronic logic elements.

In addition to such applications; research in magnetic matter today focuses on understanding dynamic processes on the nanoscale and engineering new materials with special magnetic properties.

CHAPTER 3

INTRODUCTION TO THE MAGNETIC QUANTUM-DOT CELLULAR AUTOMATA (MQCA) CONCEPT

It already has been demonstrated that propagating magnetic excitations (domain walls, solitons) in magnetic nanostructures are suitable for digital signal processing [16][17]. According to our theoretical studies [7][8][18], nanomagnets with a sufficiently large anisotropy, low coercivity and a remanence equal to their saturation state may be utilized practically as stray-field-coupled QCA building blocks. In such a QCA block, the digital information is represented by the magnetization states of an individual nanomagnet, just as in magnetic random access memory (MRAM) [19] or patterned media hard disk drive (HDD) [20] devices. The number of stable magnetization states of a nanomagnet is determined by its magnetic anisotropy, for example crystalline or shape anisotropy. The nanomagnets are required to be magnetically bistable, as shown in Fig. 3.1(a), so that the bit values '0' and '1' can be assigned to the two stable states.

Consider an elongated-shape, single-domain magnet that provides the hysteresis curve sketched in Fig. 3.1(a). This nanomagnet is strongly bistable, as its remanent magnetization (magnetization at zero external magnetic field) always points along the long axis due to shape anisotropy. Even though a magnetizing force can rotate the magnetization away from the long axis, when the force is removed, the nanomagnet switches to either of the two remanent states. Placing many of these magnets side by side

along the long axis may result in an array of dipole-coupled nanomagnets that favor antiparallel alignment of the magnetization directions. This is due to the stray field of the magnets acting on each other in close vicinity, trying to magnetize their neighbors in the opposite direction. The antiparallel alignment that develops is called antiferromagnetic ordering. In MQCA, this phenomenon drives the computation. Figure 3.1(b) illustrates a nanomagnet network in which the information propagates from left to right, influenced by the interface devices. The network is driven by an external magnetic field into a magnetic state that is allowed to relax to the antiferromagnetically-ordered ground state. The input and output of the nanomagnet network can be realized in a similar fashion to an MRAM, but the vast majority of the magnets (the interior of the array) is influenced only by the field of their neighbors, and need not be accessed externally.

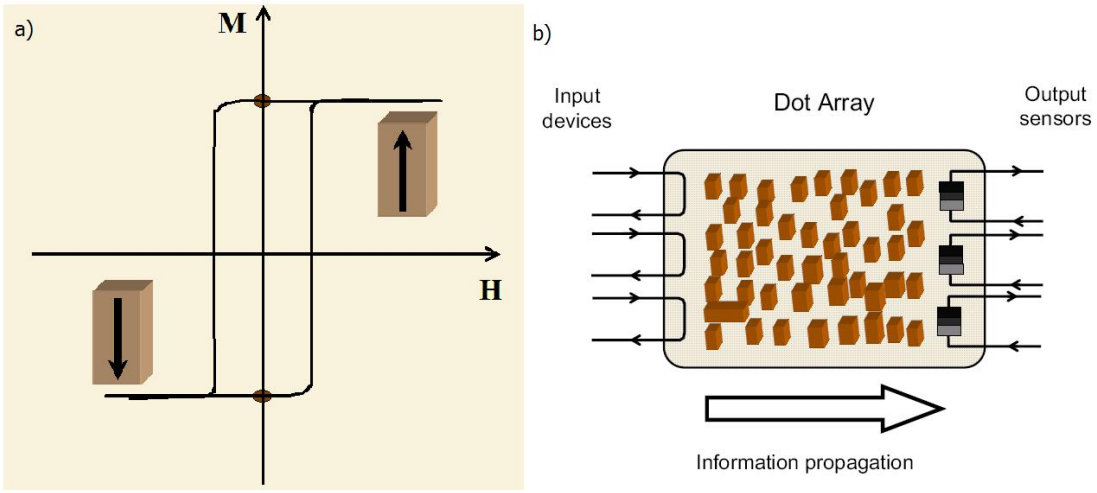

Figure 3.1 (a) Schematic hysteresis curve of an elongated nanomagnet : magnetization versus applied magnetic field, both displayed along the longest axis of the magnetic particle. (b) Illustration of a magnetic computing array. The information flows from the input devices toward the output devices via magnetic interactions.

The field-coupled QCA devices are operated by an external clock, a periodically oscillating external magnetic field in our case, which is able to drive the system into an initial state and to control the relaxation to a ground state. The calculated total magnetostatic energy of two coupled single-domain permalloy nanomagnets as a function of the magnetization direction of the right dot is shown in Fig. 3.2(a) [18]. The magnetization of the left magnet is fixed. The magnetostatic energy is dominated by shape anisotropy of the elongated magnets, which keeps the magnetization of the dots bistable and results in two deep energy minima for magnetization directions parallel to the magnetic easy axis (for 0º and for 180º). The ground state is found for 180º due to the dipolar coupling, which favors the antiparallel alignment; while the parallel alignment is found for 0º and represents a metastable state. The energy difference between ground state and metastable state is approximately 150 kT at room temperature, and the energy barrier from metastable to ground state is approximately 100 kT; both are significantly large for application at room temperature.

The role of the external clock-field is to overcome the energy barriers between metastable states and ground state. Clocking can be performed by applying the magnetic field along the short axis of the dots, as explained in Fig. 3.3 [8]. In Fig. 3.3(b) the external field turns the magnetic moments of all magnets horizontally into a neutral logic state, later referred as “null” state, against the preferred magnetic anisotropy. This is an unstable state of the system, and when the field is removed, the nanomagnets relax into the antiferromagnetically ordered ground state, as shown in Fig.3.3(d). If the first dot of the chain is influenced by an input device during relaxation, then its induced switching sets the state of the whole chain due the dipolar coupling. To effect line switching, the

input device must produce a local magnetic field that influences only the first nanomagnet in the chain, and which is oriented parallel with the long geometrical axis. This can be realized by a current carrying electrical wire, for example, as shown in Fig. 3.3.

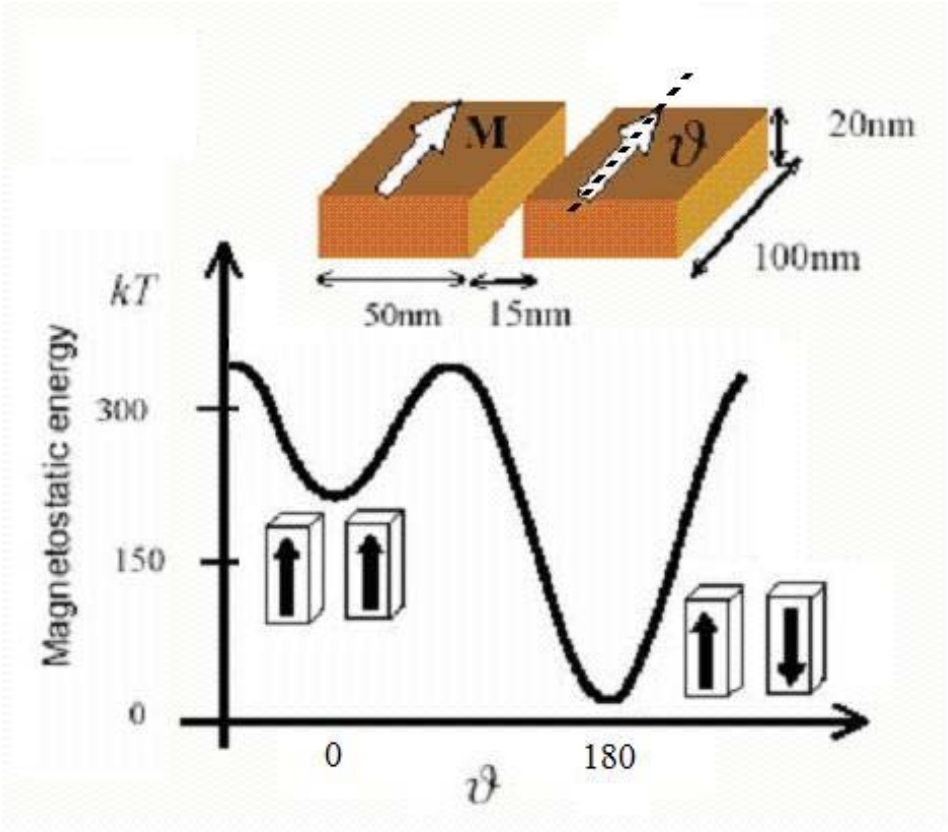

Figure 3.2 Room-temperature energy diagram of two coupled nanomagnets in the function of angle of magnetization of the right nanomagnet as against the fixed magnetization direction of the left nanomagnet.

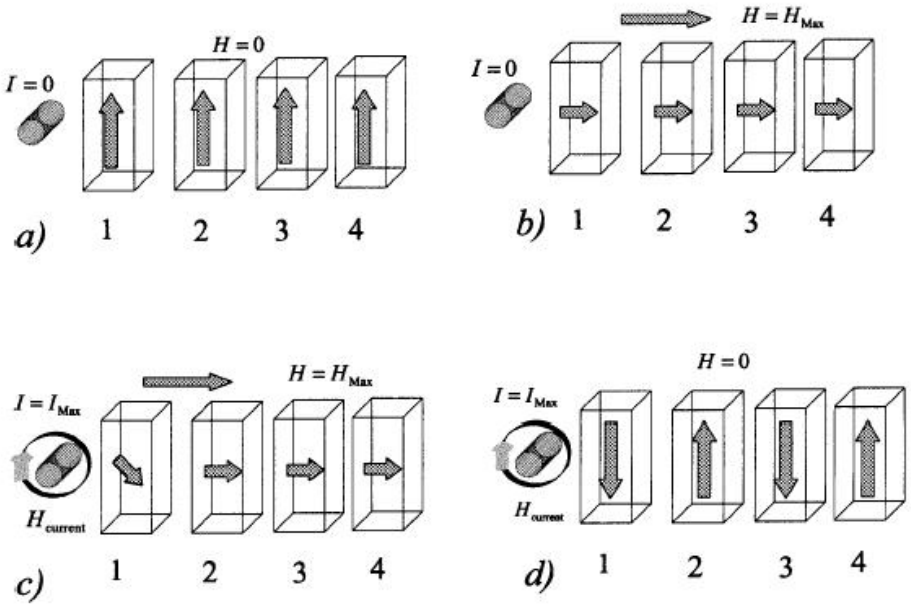

Figure 3.3 Operating scheme of the nanowire: (a) Initial configuration, (b) high-field state ("null" state) before and (c) after the application of the input. (d) final ordered state. [8]

One can think of this chain of coupled nanomagnets as an inverter chain. Chains containing an odd number of dots simply transmit the state of the input, and those containing even numbers of dots operate as an inverter. The clock field affects the whole chain, thus all the inversions are done in one clock cycle. This brings up the first question that needs to be answered by experimental investigations, i.e. is there a critical length for these chains for which the antiferromagnetic ordering tends to be perfect (errorless)? If the answer is yes, then is it large enough to support more complicated arrangements of dots that work as a logic gate?

CHAPTER 4

INVESTIGATION OF FABRICATION TECHNIQUES

The technology for fabricating arrays of nanomagnets is currently under development in the HDD and MRAM industrial research.

Patterned magnetic media are under consideration for used in HDDs to further increase the areal density [20][21]. Replacing thin-film media, patterned media consist of a regular array of magnetic nanoelements with uniaxial anisotropy. The bits are stored in the magnetization of the single domain nanoelements, just as in the case of MQCA. The patterned media development is still at an early stage. Fabrication techniques involve electron-beam lithography (EBL), X-ray and interference lithography, nanoimprinting, magnetic material deposition and pattern transfer. The deposition of the magnetic material is usually done by electroplating, sputtering or evaporation; the pattern transfer applies reactive ion etching (RIE) or low-energy ion irradiation. Focused ion beam (FIB) techniques are also under consideration [22][23].

There is a significant effort directed toward fabricating nanomagnets with an easy axis perpendicular instead of parallel to the surface, and many papers present fabrication of nanopillars [24], or patterning of metallic multilayers [25][26][27], which both provide out of plane domain orientation.

In addition to the research using the conventional fabrication techniques listed above, there is progress in self assembly of magnetic nanoparticles from colloidal solution [28][29].

Finally, there are some attempts to employ biomineralization of magnetic particles, as it can produce single and perfect crystals [30][31][32].

4.1 CoPt deposition on pre-patterned surfaces, and focused ion beam patterning of continuous CoPt thin films

We investigated patterning CoPt multilayer thin films that exhibit perpendicular magnetic anisotropy, i.e. the preferred magnetization direction points out of plane, due to interface effects between cobalt and platinum layers. The most critical issue in this approach is to have a good control on the deposition, because the anisotropy is very sensitive to the thickness and to the interface of the layers.

Two methods were followed in this study, deposition on pre-patterned surfaces, and focused ion-beam patterning of pre-deposited films, as illustrated in Fig. 4.1.

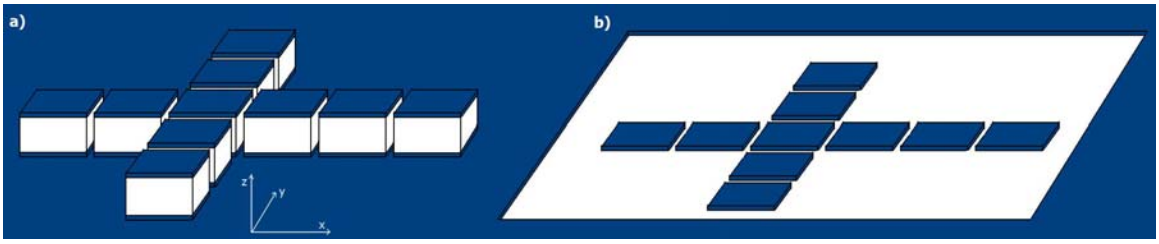

Figure 4.1 Schematic of majority gate geometries fabricated (a) by CoPt deposition on pre-patterned substrate, and (b) by focused ion beam (FIB) milling.

In the case of deposition on pre-patterned surface, the fabrication process was the following:

- Define the pattern by EBL on PMMA (on SiO_2 and on Si surfaces)
- Create mask by Pt evaporation (35 nm) and lift-off
- Transfer pattern by RIE (CF_4 25 sccm, O_2 5 sccm, 250 W, chamber at 30 mTorr)
- Sputter deposit CoPt (EMITECH K-675X sputter coater, $9 \cdot 10^{-3}$ mbar Ar plasma, one cobalt and two platinum targets, 200 mA, co-deposition with rotating sample stage, 36 rotations overall)

The approach to define fine patterns by high-resolution lithography, and then to transfer them into the substrate by RIE is described in [33] and [34] in the context of patterned perpendicular magnetic media for data storage.

The sputtering parameters in our case were optimized for largest domain size by means of magnetic force microscopy (MFM). The sputtered magnetic deposit covers the top of the islands, the bottom of the trenches and to a lesser extent the sidewalls of the islands. Stripes of domains inside which the magnetization points out-of-plane, were found to form on the top of the islands, while the anisotropy was destroyed in the trenches, where the surface was rough after the RIE, as is seen in Fig. 4.2(b). We could not observe clear a single-domain magnetic configuration even for the smallest islands (see Fig. 4.2(d)). This might be because further reduction of the island size is required, or because the magnetic moments relax into the plane at the edges. The effect of the sidewall deposition is also questionable, as it is exchange coupled to the top. We abandoned this fabrication method because answering these questions would require more sophisticated methods such as very high resolution scanning electron microscopy with polarization analysis (SEMPA).

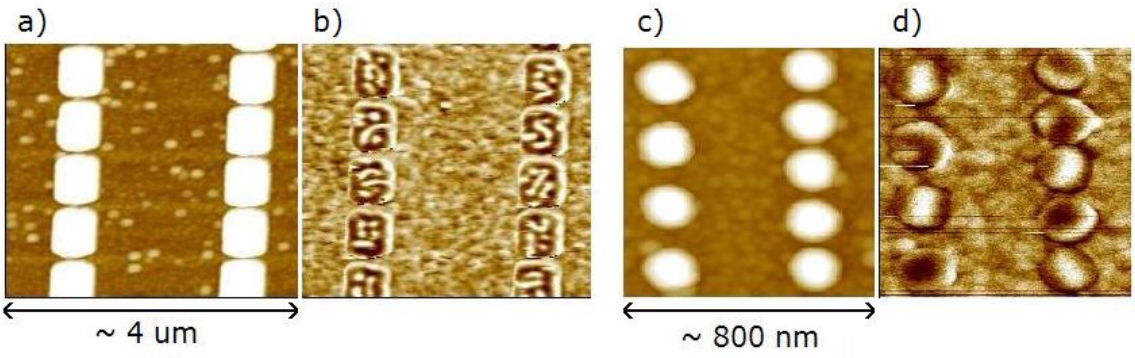

Figure 4.2 (a) and (c) AFM, (b) and (d) MFM images show the result of CoPt deposition on pre-patterned silicon surface.

For the other method we investigated, we used a pre-deposited CoPt thin film, which was prepared at the IBM Almaden research center by Olav Hellwig, alternating up to 50 layers of sputter-deposited cobalt and platinum. The hysteresis curves of this sample, which we measured by SQUID, indicated strong perpendicular anisotropy.

The focused ion-beam milling was done by a LEO 1540 Crossbeam microscope at the Research Institute for Technical Physics and Materials Science, in Budapest, Hungary, with the following parameters: Ga liquid-metal ion source, 30kV acceleration voltage, 5-6 mm working distance, 2-5 pA probe current, 9-10 nm spot size. Figure 4.3 shows a representative image of the patterned surface. According to the MFM data, single-domain magnets were fabricated successfully. However, long range ordering on the chains was not observed. The accumulated dust from the milling process may have disturbed the designed patterns since it appeared to be magnetic on the MFM images generating a small contrast.

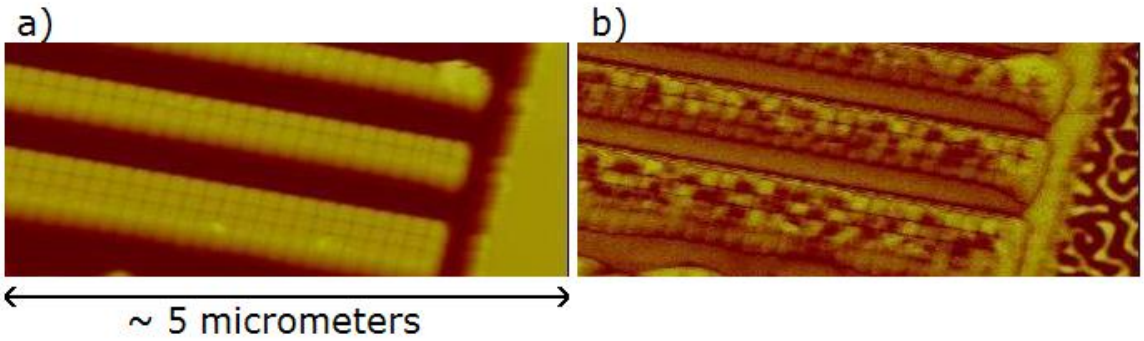

Figure 4.3 (a) AFM and (b) MFM images show the result if FIB milling of CoPt multilayer thinfilm.

This work was presented in [35].

4.2 NiFe alloy and Co structures made by electron-beam lithography and lift-off

For the MQCA studies, we fabricated our test samples by means of EBL, thermal evaporation and lift-off. First, poly-methyl-methacrylate (PMMA) was spun on the surface of an oxidized silicon wafer. PMMA is available in different solutions with various molecular weights and widely used as a high contrast, high resolution e-beam resist [36]. PMMA is a positive resist, which undergoes chain scission and a reduction in molecular weight with exposure to an electron-beam at normal doses of 300-500 $\mu C/cm^2$. The developer is strongly selective toward the dissolution of the low molecular weight components of the resist. The role of molecular weight and developer strength on etch rate of PMMA was analyzed extensively by Greeneich [37]. Generally, a high molecular weight material is chosen for high contrast and resolution performance. In order to improve the lift-off, an additional co-polymer layer (a mixture of methyl methacrylate and methacrylic acid) can be employed under the PMMA layer. The resist thickness that we use varies between 60 and 240 nm for the PMMA and between 150

and 550 nm for the co-polymer. Pre-bake is done on a 175 ºC hotplate for a few minutes for each layer. Figure 4.4 illustrates the steps of the fabrication process for both single layer and double layer samples.

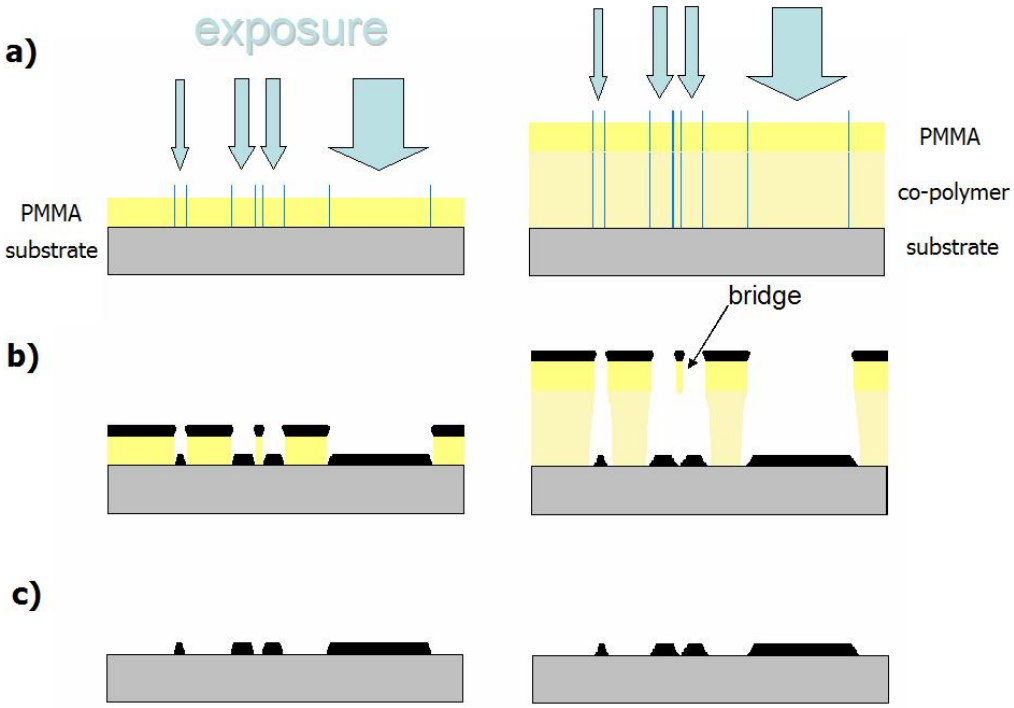

Figure 4.4 Electron-beam lithography and lift-off technology process steps.
(a) Exposure, (b) metal deposition and (c) lift-off.

The EBL was carried out on an AMRAY 1400 converted scanning electron microscope driven by the Nanometer Pattern Generator System by J. C. Nabity [38]. Using a thermal emission tungsten cathode in the gun with 50 kV acceleration voltage, we have a lithography resolution of about 15-20 nm, a minimum line width of 30-35 nm and a minimum of 60-80 nm pitch. To develop the exposed image, we use a solution of methyl-isobuthyl ketone (MIBK), isopropanol (IPA) and methyl-ethyl ketone (MEK), 1:3:1.5% respectively, which has been identified as a high contrast developer by Bernstein et al. [39]. In Fig. 4.4(b) the difference between the single layer and the double

layer resist is shown by the larger undercut in the co-polymer. On the one hand, this can prevent the formation of thin, walls along the border of the dots as seen in Fig 4.5(a). On the other hand, the patterns are less defined in the presence of the co-polymer because of its larger shadow angle. As a result, the evaporated material that does not arrive perfectly perpendicular to the surface of the substrate most of the time, spreads out. Another property of the double layer resists is the development of PMMA bridges. These bridges appear to be quite elastic, and can cause pattern deformation if they stick together before evaporation as Fig. 4.5(b) reveals. We evaporated cobalt or permalloy as magnetic material in an Airco Temescal FC1800 e-beam evaporator. Both ferromagnetic materials have a melting point of around 1750 K. After evaporation, the lift-off is done in a mixture of methylene chloride (MC) and acetone (ACE) at a ratio of 8:1 respectively, at room temperature.

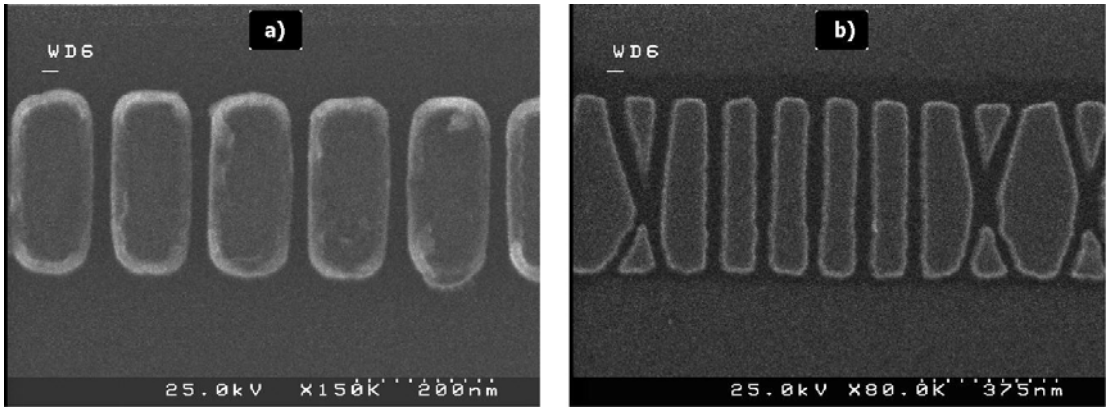

Figure 4.5 Top view SEM micrographs after lift-off. The elongated and flat, identically defined cobalt dots in the chains were fabricated (a) on single layer and (b) on double layer resist. In case of single-layer resist, there is material accumulation of the edges of the elements. In case of using double-layer resist, the pattern can get deformed as the PMMA bridges stick together.

The nanomagnets that can be fabricated by lift-off technique are necessarily planar.

Building of pillar type nanomagnets, which would have perpendicular anisotropy due to their shape, fails, because of the closing of the PMMA windows as the evaporated metal accumulates on the circumference. If high aspect ratio pits are developed in the resist, the windows may close totally before the end of the deposition, as it has happened in case of the permalloy cones shown in Fig. 4.6.

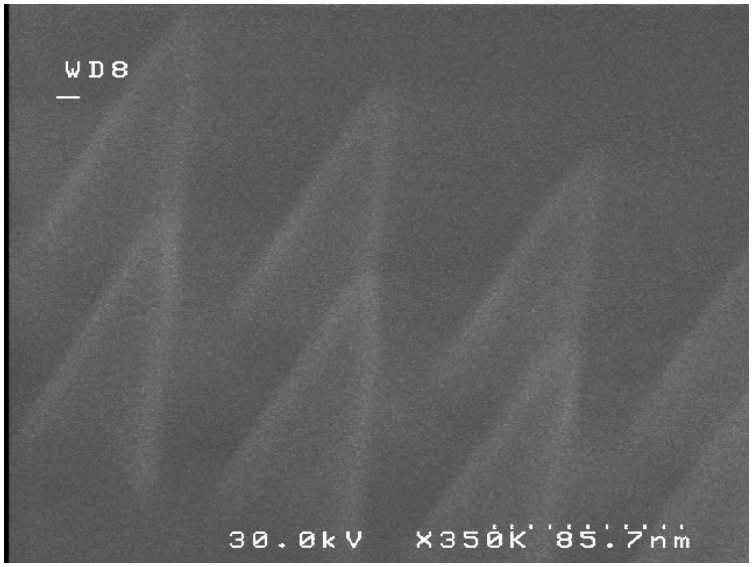

Figure 4.6 Tilted SEM image of magnetic cones fabricated by lift-off.

The resolution of our e-beam lithography system is approximately 15-20 nm. With this resolution we can fabricate lines of approximately 30-35 nm wide, and can place elements approximately 20 nm apart at the closest, but still separated. Given this resolution, elements in the order of 100 nm can be fabricated with some control over the shape.

CHAPTER 5

PROPERTIES OF NANOMAGNETS

Magnetism at the nanoscale exhibits different physical phenomena than at macro scales. These phenomena arise because the physical size of the magnetic element is comparable to or smaller than the characteristic magnetic length scales. Many of the magnetic characteristic length scales, such as the domain size, the domain-wall width, the exchange length, or the thin-film perpendicular anisotropy threshold, are ruled by energy minimization. Some others, such as the spin diffusion length or the spin precession length, are the result of diffusion processes. The magnetic phenomena that appear in mesoscopic systems may be very diverse depending on the combination of the characteristic length scales involved. For an extensive review of characteristic length scales, see [40] from Dennis.

5.1 Characteristic ferromagnetic material constants and the energy terms

Ferromagnets are characterized by intrinsic and extrinsic magnetic properties. Intrinsic properties, such as Curie temperature (T_C), saturation magnetization (M_S), magnetostriction (λ_S) and magneto-crystalline anisotropy (K_1), are independent of microstructure or nanostructure. Extrinsic properties, such as induced anisotropy (K_U), remanence magnetization (M_R) or the coercivity field (H_C), however, derive from the

physical dimensions. The design of nanomagnets for specific applications therefore involves a careful selection of material and physical structure.

The main intrinsic properties of the *3d* metallic ferromagnetic elements, such as iron, cobalt and nickel, are collected in Fig. 5.1 after Coey [41]. The values refer to room temperature.

	Structure / density (kg/m^3)	T_C (K)	M_S (MA/m)	λ_S (10^{-6})	K_1 (kJ/m^3)	A (pJ/m)	l_{EX} (nm)	δ_{BW} (nm)
Fe	bcc 7874	1044	1.71	-7	48	8.3	1.5	41
Co	hcp 8836	1388	1.45	-62	530	10.3	2.0	14
Ni	fcc 8902	628	0.49	-34	-5	3.4	3.4	82

Figure 5.1 Characteristic constants of iron, cobalt and nickel, after Coey [41].

Each of the three elements has a different crystal structure, namely body centered cubic (bcc) for Fe, hexagonal closely packed (hcp) for Co, and face centered cubic for Ni. The crystal structure is responsible for the magneto-crystalline anisotropy K_1.

T_C is the Curie temperature above which the material loses its magnetic long range order and becomes paramagnetic.

The magnetostriction parameter, λ_S, describes the change of a material's physical dimension due to change in its magnetization. The mechanical-strain-induced magnetic anisotropy is related to σ, the stress on the crystal, by:

$$K_{U,STRESS} = (3/2)\lambda_S\sigma \tag{5.1}$$

A is the exchange stiffness with which the exchange length, l_{EX}, is derived as

$$l_{EX} = \sqrt{A / \mu_\circ M_S^2} \tag{5.2}$$

δ_{BW} is the width of the Bloch wall, derived as

$$\delta_{BW} = \sqrt{A / K_1} \tag{5.3}$$

The intrinsic magnetic properties of the materials can be tailored by alloying. Permalloy is an fcc Ni_XFe_{1-X} alloy with composition range $0.78<X<0.81$, and it is probably the best-studied soft magnetic material. The particular feature of permalloy is that K_1 and λ_S change sign at nearly the same composition by chance, which makes it possible to achieve an excellent soft material with basically no intrinsic magnetic anisotropy. The main drawback of permalloy is its relatively weak polarization of $\mu_0 M_S \approx 1.0$ T.

Designing extrinsic properties of nanomagnets, one needs to consider an energy balance between exchange, self-demagnetizing, and anisotropy energies of the magnetic body. In summary, the contributing energies are the following:

- The exchange energy is associated with quantum mechanical interactions among atomic moments that tend to align with each other in ferromagnetic materials.
- The self-demagnetizing or magnetostatic energy is associated with the potential energy per volume of the magnetization M in its own self-field.

- The anisotropy energy is associated with the tendency of the magnetic moments to align in certain directions. Magnetic anisotropy can be exerted by a non-symmetric crystal structure or stress, which both have an effect on electron spin-orbit coupling and crystal fields; or it can be induced by the shape of the particle, considering the self-demagnetizing effect at the boundaries.

The magnetic domain and domain wall formation is the result of an energy balance in the magnetic materials. In magnetic materials that exhibit anisotropy, the magnetization within the domains points into one of the easy axis directions. Figure 5.2 displays different magnetic domain structures that were made visible with the help of polarization optics.

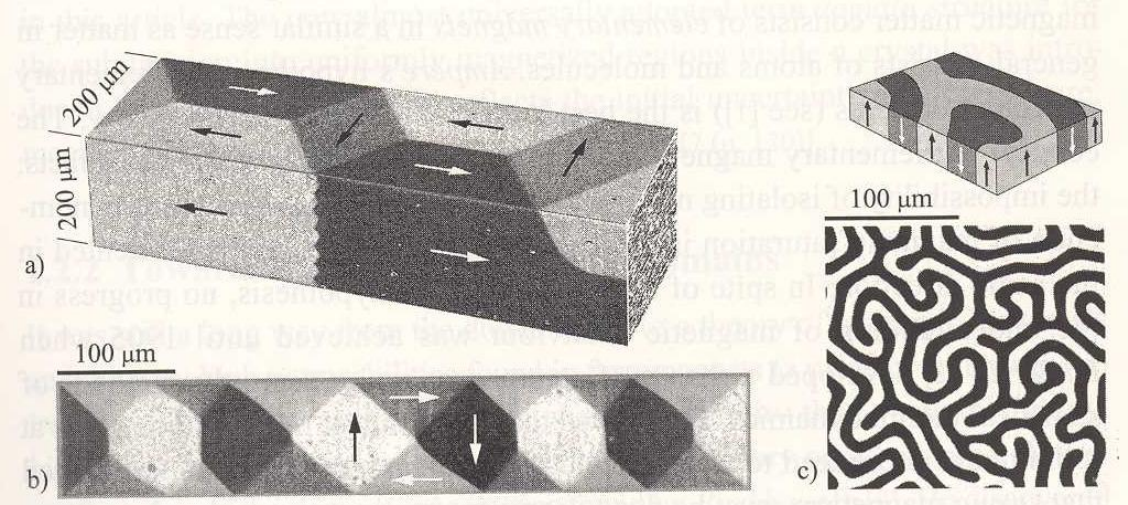

Figure 5.2 Domains observed with magneto-optical methods on homogeneous magnetic samples. (a) Images from two sides of an iron whisker, combined in a computer to simulate a perspective view. (b) Thin film NiFe element (thickness 130 nm) with a weak transverse anisotropy. (c) Faraday effect picture of domains in a single-crystal garnet film (bottom) with perpendicular anisotropy, together with a schematic of the magnetization (top). From Hubert and Schafer [11], page 1.

5.2 Magnetic force microscopy (MFM) studies

Our technique to study magnetic nanostructures, magnetic force microscopy (MFM), provides close to the best magnetic spatial resolution available today. However, MFM can obtain only steady-state magnetic images due to the scanning-probe approach. We use a multimode scanning probe microscope (SPM) that performs the full range of atomic force microscopy (AFM) and scanning tunneling microscopy (STM) techniques to measure surface characteristics including topography, elasticity, friction, adhesion, and magnetic/electrical fields.[*] Magnetic force microscopy is a secondary imaging mode of the SPM, and it is derived from tapping mode (TM), that is a patented technique (by Veeco Instruments). TM maps topography by lightly tapping the surface with an oscillating probe tip. The cantilever's oscillation amplitude changes with sample surface topography, and the topographic image is obtained by monitoring these changes and closing the z feedback loop to minimize them.

Dynamic MFM maps the magnetic force gradient (F_{grad}) above the sample surface. This is performed through a two-pass technique, i.e. the "Lift Mode". Lift Mode separately measures topography and another selected property (magnetic force, electric force, etc.) using the topographical information to track the probe tip at a constant height (lift height) above the sample surface during the second pass as illustrated in Fig. 5.3.

[*] Digital Instruments Nanoscope IV

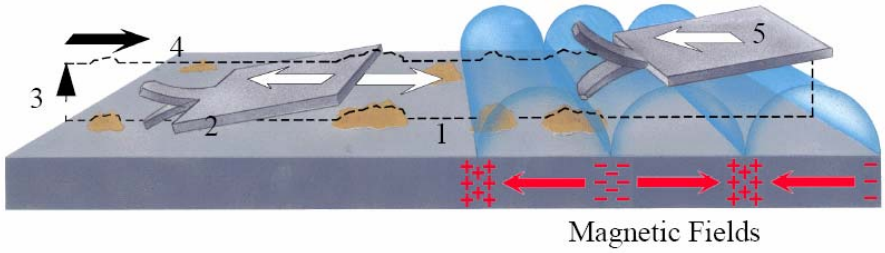

Figure 5.3 MFM Lift Mode principles, from DI support notes [42]. (1&2) Cantilever traces surface topography on first trace and retrace. (3) Cantilever ascends to the lift scan height. (4&5) Lifted cantilever profiles topography while responding to magnetic influences on second trace and retrace.

We use standard and low-moment etched silicon MFM probes with a cantilever length of 225 μm and a corresponding spring constant (c_L) of approximately 1 N/m. The tip is coated with a ferromagnetic thin film, and it can be viewed as a magnetic dipole oriented in the z-direction because of its shape.

While scanning, the vibrating cantilever behaves to first approximation as a driven harmonic oscillator, and its equation of motion is:

$$F = m\frac{\partial^2 z(t)}{\partial t^2} = -c_L z + F_0 \cos 2\pi f_0 t + F_{z,\text{grad}} z \tag{5.4}$$

where m is the effective mass of the cantilever,
c_L is the spring constant of the cantilever,
F_0 is the driving force of the oscillation,
and $F_{z,\text{grad}}$ is force gradient of a magnetic field acting on the tip in the direction of motion:

$$F_{z,grad} = \frac{1}{\mu}\left(M_x \frac{\partial^2 H_x}{\partial z^2} + M_y \frac{\partial^2 H_y}{\partial z^2} + M_z \frac{\partial^2 H_z}{\partial z^2} \right). \tag{5.5}$$

This can be simplified if we assume the tip to behave as a magnetic dipole.

(Mz >> Mx, My).

In general, every spatially varying force field changes the resonant frequency of the cantilever. In the case of our microscope, the tip is driven to oscillate at a fixed frequency, and the MFM signal is the change of phase, which is recorded as a function of x, y, and z. The recorded phase-shift of the cantilever oscillation is directly proportional to the second derivative of the spatially varying magnetic force field. In this mode, the amplitude is controlled to be constant. Alternatively, the amplitude could be recorded and the phase could be kept constant.

Figure 5.4 shows stray field of a single-domain magnet, and the second derivative of the stray field above the magnet at a particular distance, calculated by György Csaba. The colors blue and red represent opposite signs. Thus opposite poles of a magnet (i.e. South and North) appear with opposite contrast on the MFM phase image (an image that is constructed tracking the phase changes of the output signal).

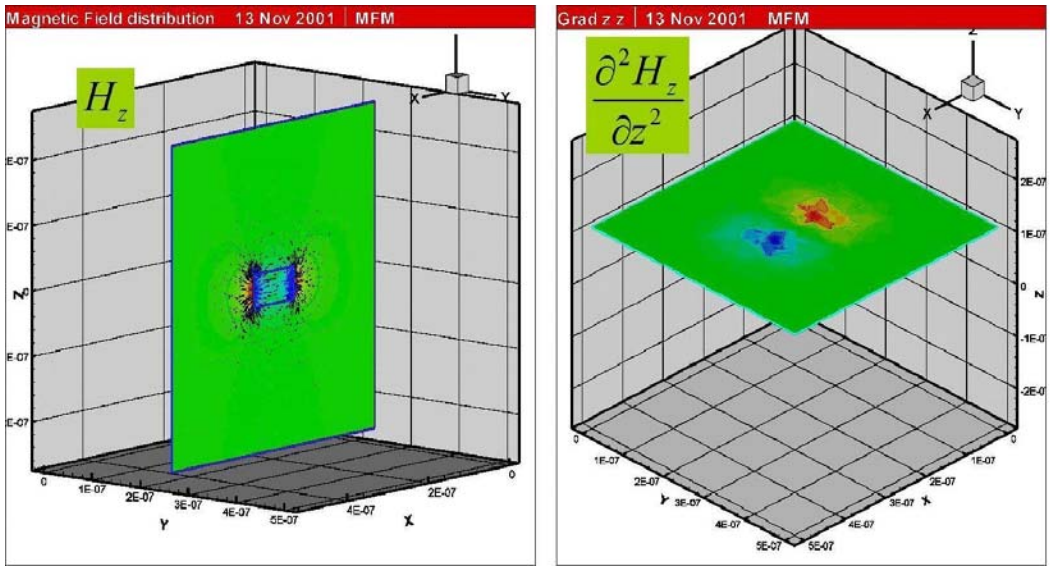

Figure 5.4 Calculated stray field of a planar elongated magnet shown in a vertical plane that cuts through the magnet (on the left), and calculated second derivative of the stray field in a plane above the magnet (on the right).

Figure 5.5 illustrates the topographic and the magnetic phase images of a single-domain permalloy magnet. The magnetic poles are clearly visible in Fig. 5.5(b).

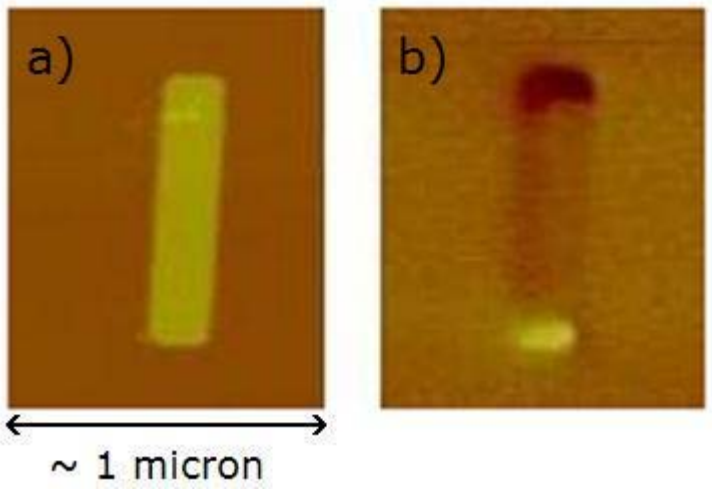

Figure 5.5 (a) Topography and (b) Lift Mode phase images of a single-domain permalloy magnet.

If the lateral magnetic resolution allows, MFM can map the internal domain structure of multi-domain magnets too. For example, see Fig. 5.6. In this case the contrast is generated by the stray field of domain walls. Magnets with just slightly different parameters, or the exact same magnet after different magnetization processes can exhibit different domain structures.

In order to understand the dynamics of magnetic domain formation and to confidently reconstruct magnetization states based on MFM images, we use a popular micromagnetic simulator, called object oriented micromagnetic framework (OOMMF), developed by the National Institute of Standards and Technology (NIST). Reconstructing the magnetization from an MFM image is not straightforward. The reconstruction method is described in [43].

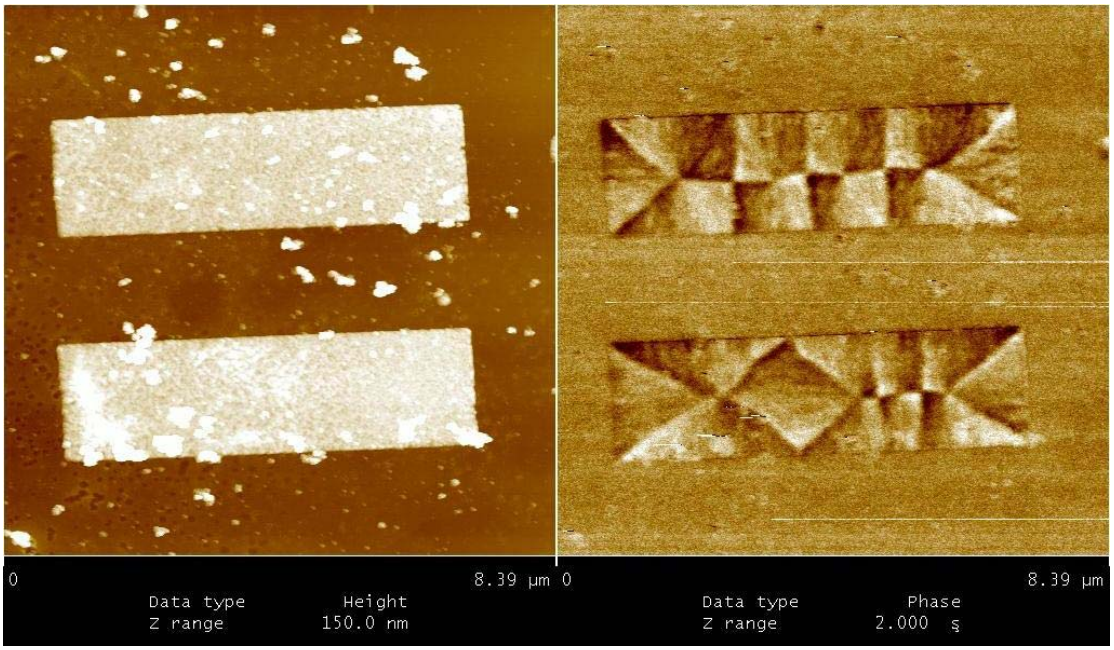

Figure 5.6 Topography and Lift Mode phase images of two micron-size permalloy magnets.

5.3 Micromagnetic simulator studies

OOMMF is a project of the Mathematical and Computational Sciences Division of the Information Technology Laboratory at NIST, in close cooperation with the micromagnetic activity group (µMAG) of the Center for Theoretical and Computational Materials Science at NIST. OOMMF is package of portable, extensible public domain programs and tools for micromagnetics [44]. The code forms a completely functional micromagnetics package, and also has a well documented, flexible programmer's interface so that people developing new code can swap their own code in and out as desired. The main contributors to OOMMF are Mike Donahue and Don Porter.

The core of the code is written in C++ with an open source scripting language Tcl/Tk interface. Target systems include a wide range of Unix and Windows platforms. The OOMMF applications communicate over Internet (TCP/IP) connections in modular architecture.

The micromagnetic problem, i.e. the geometrical description of a magnetic element, is impressed upon a regular 2D grid of squares, with 3D magnetization spins positioned at the centers of the cells. For each cell, the solver integrates the Landau-Lifshitz equation:

$$\frac{d\mathbf{M}}{dt} = -\gamma\,\mathbf{M}\times\mathbf{H}_{\text{eff}} - \frac{\gamma\alpha}{M_s}\,\mathbf{M}\times(\mathbf{M}\times\mathbf{H}_{\text{eff}}), \tag{5.6}$$

where **M** is the pointwise magnetization (A/m),
γ is the gyromagnetic ratio (m/(A·s)),
α is the damping coefficient (dimensionless),
$\mathbf{H}_{\text{eff}}$ is the pointwise effective field (A/m), defined as:

$$\mathbf{H}_{\text{eff}} = -\mu_0^{-1}\frac{\partial E}{\partial \mathbf{M}}. \tag{5.7}$$

The average energy density, E, is a function of **M** specified by Brown's equations, including crystalline anisotropy, exchange, self-magnetostatic (demagnetization) and applied field (Zeeman) terms; thus the effective field depends on the magnetization in a very complex way: partly through Maxwell's equations, and partly through phenomenological forces, which take into account quantum mechanical effects quasi-classically. The steady state solutions are usually complex domain patterns for larger size bulk materials. Apart from some very special cases, the Landau-Lifshitz equation must be treated numerically, and for larger structures (>5-10 μm) this becomes increasingly time consuming.

Figure 5.7 illustrates a 2D simulation in which the 3 nm cell size used is visible. Small asymmetries are introduced to the simulated shape when the bitmap file, which is used as an input, is mapped onto the simulator's grid.

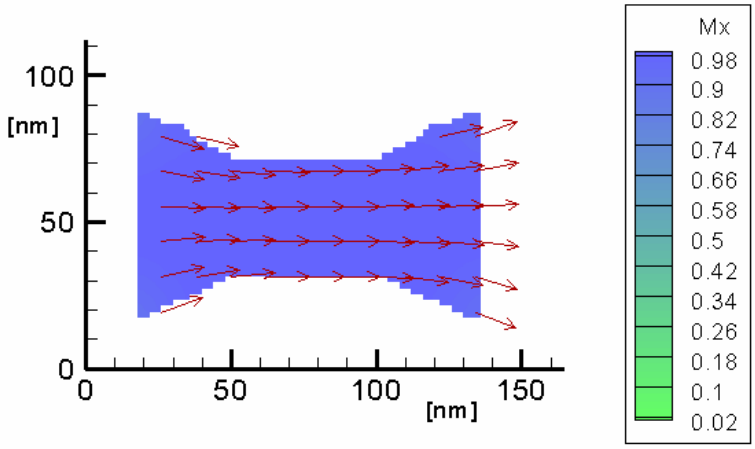

Figure 5.7 Simulation of a nanomagnet in OOMMF [44].

Arrows in a figure of a simulation represent magnetization direction, while the coloring is assigned to one of the normalized vector components (i.e. x, y or z) in each cell.

In addition to the description of geometry in a BMP file, the simulator requests characteristic material constants, and external magnetic field description of the simulated experiment. Figure 5.8 shows the characteristic parameters that are used in our simulations. For the damping coefficient, α, a default value of 0.5 is set, which allows the solver to converge in a reasonable number of iterations. Physical materials have α typically in the range 0.0004 to 0.15. The anisotropy type is set to uniaxial in the plane, as we consider stable magnetization to point solely in the plane.

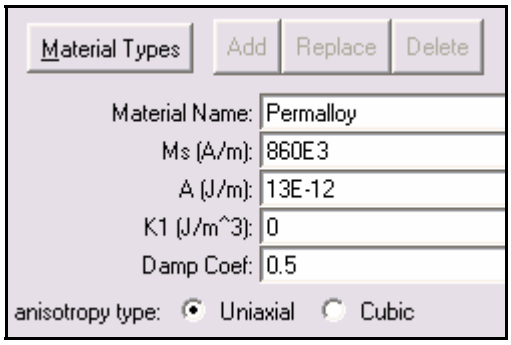

Figure 5.8 Screen-shot of the characteristic parameters setting.

As a further example, we introduce the simulated hysteresis loop of the nanomagnet that was already shown above, in Fig. 5.7. The hysteresis curve simulated in the direction of the easy magnetic axis is displayed in Fig. 5.9. In general, at the microscale the hysteresis curve tends to appear like a staircase, where the steps correspond to sudden transitions, i.e. partial magnetization reversals. At the nanoscale, the magnetization reversal can occur in a single step, which results in a square-like hysteresis curve, such as shown in Fig. 5.9.

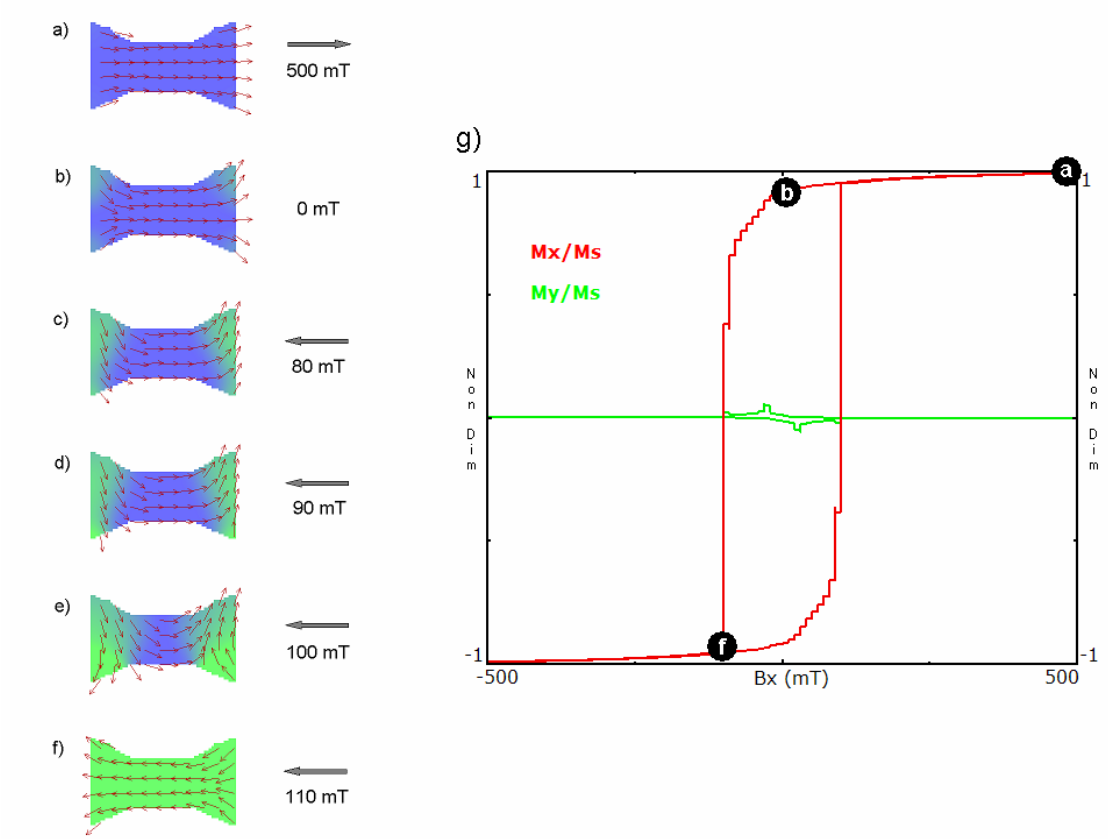

Figure 5.9 Simulated magnetization reversal along the easy axis of a nanomagnet.

Figure 5.10 displays the hysteresis loop simulated in the direction of the hard magnetic axis.

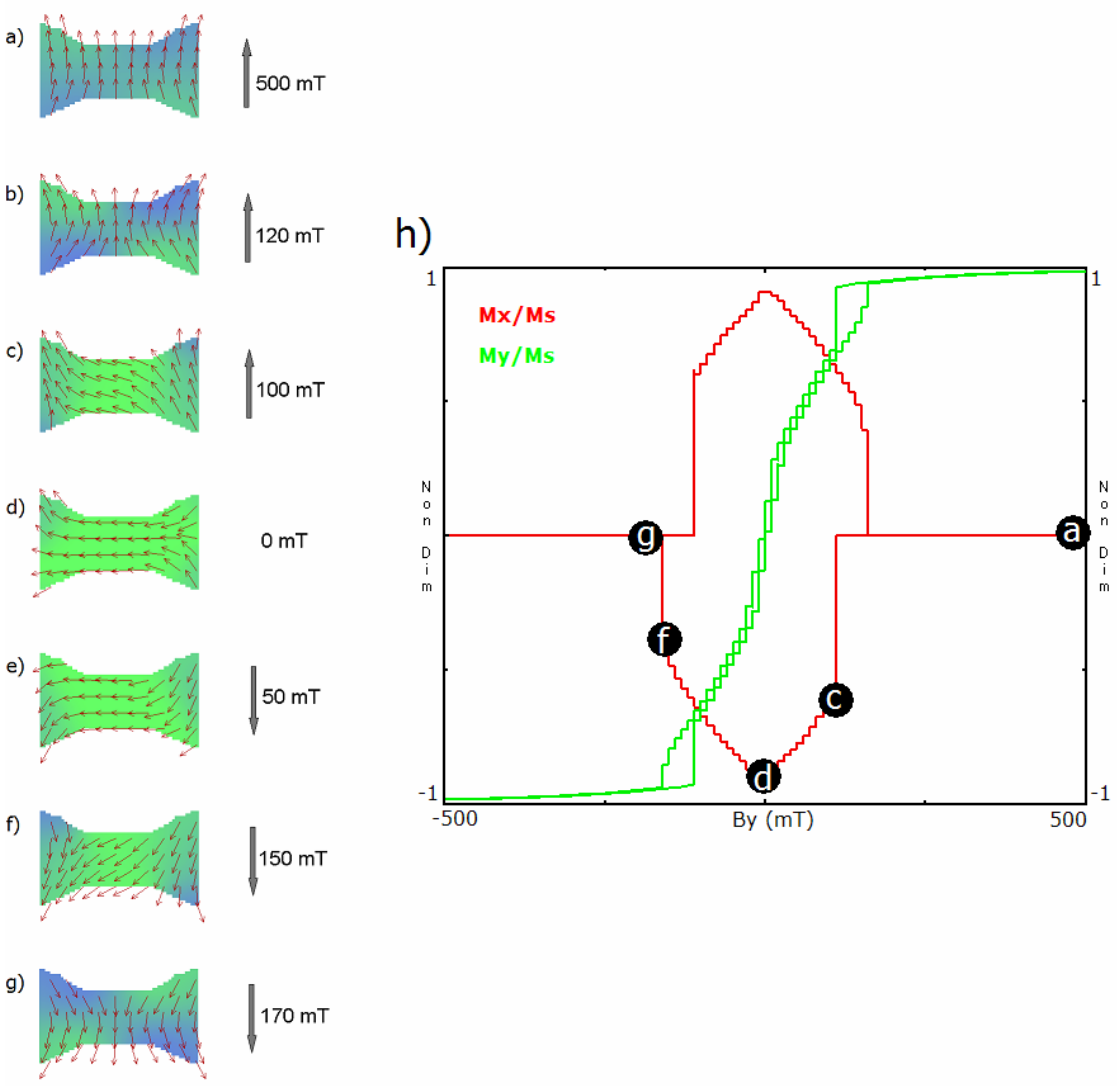

Figure 5.10 Simulated magnetization reversal along the hard axis of a nanomagnet.

Not only magnetization, but magnetic fields can also be simulated by OOMMF. Figure 5.11 shows a study of stray field of a nanomagnet. Outside the nanomagnet, the strongest stray fields occur at the close vicinity of the corners, where they reach 250 mT as is shown in Fig. 5.11(b). At 10 – 15 nm away from the corner boundaries, the magnetic stray-field is still of the order of 100 mT, as displayed in Fig. 5.11(c). Stray

fields larger than 10 mT can be found everywhere around the nanomagnet within a distance of approximately 50 nm, as shown in Fig. 5.11(d).

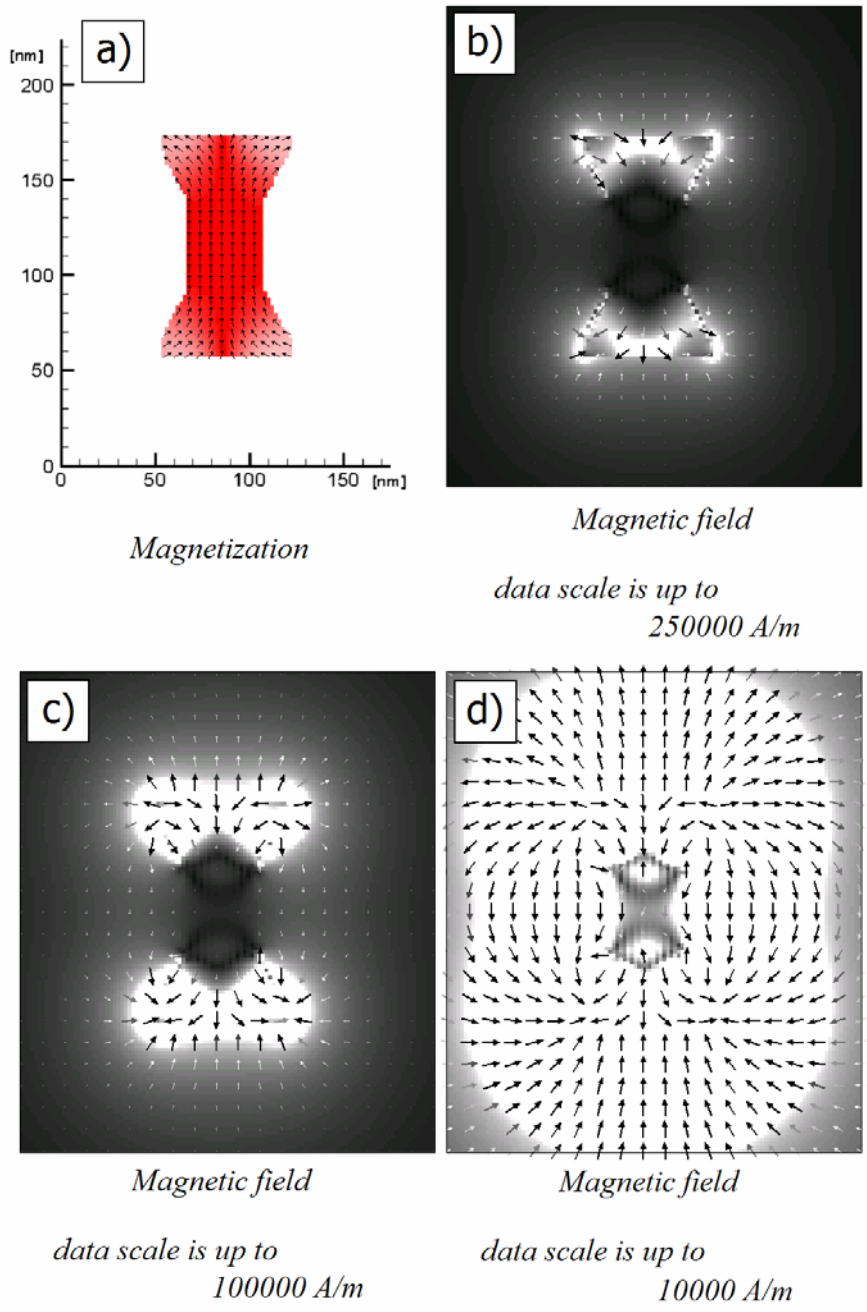

Figure 5.11 Simulated stray field of a nanomagnet. (a) Magnetization of the nanomagnet. On the stray field images white areas correspond to magnetic fields higher than (b) 250,000 A/m, (c) 100,000 A/m, and (d) 10,000 A/m.
The magnetic field values can be converted to induction by the SI equation $B = \mu_0 H$

CHAPTER 6

MAGNETIC RINGS AND FLUX-CLOSURE MAGNETIC DOTS FOR QCA

Nanomagnets display well-defined domain patterns that evolve into each other at specific applied fields. The domain patterns can be designed by choosing proper shape for the magnets. Thus, it is possible to design nanomagnet devices that show intended functionality. We demonstrate such functionality in the last chapter. Both multi-domain and single-domain structures, however, suffer from a relatively wide distribution of domain nucleation fields, which is referred to as the switching field distribution.

Circular rings attracted special attention recently [45] due to the lack of strong stray fields in their flux-closure states, which ensures narrower switching field distribution than for nanomagnets with sharp ends.

6.1 Investigation of micron size square-rings

We investigated the static domain structures and the magnetization reversal processes of square-rings. Figure 6.1 (b) demonstrates a common magnetic state of such ring, where two oppositely ‘charged’ domain walls are localized in the opposite corners.

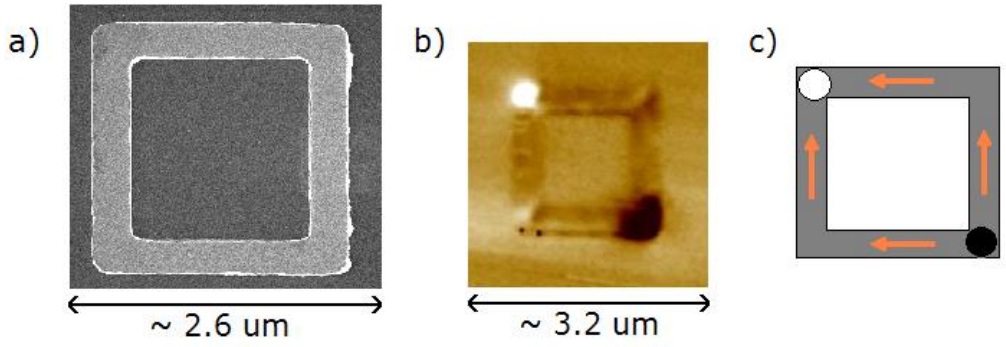

Figure 6.1 Micron size cobalt square-ring fabricated by e-beam lithography and lift-off, sample is courtesy of Vitali Metlushko, University of Illinois. (a) SEM, (b) MFM image of the fabricated sample, and (c) schematic drawing of the magnetization direction inside the ring that corresponds to the MFM image.

Domain walls can be either charged (when a net magnetization points inward or outward at the corner) or neutral (when the magnetization simply 'bends' at the corner). By putting domain walls with positive, negative, or zero net volume charge to the corners (and only to the corners) in all possible combinations, we obtain a set of basic domain configurations of square rings, as summarized in Fig. 6.2.

We have fabricated permalloy square rings with a size of 2.1 μm x 2.1 μm, 180 nm wide, and 25 nm thick, and investigated domain-wall motion in them [46]. Micromagnetic simulations confirm the stability of the above introduced magnetic states in our samples. If no charged domain walls are present in a ring, it displays a clockwise or counterclockwise flux-closure magnetization distribution (see Fig. 6.2(b)). The next simplest configuration arrangement consists of two, oppositely-charged walls. The walls may occupy either opposite (as shown in Fig. 6.2(a)) or neighboring corners (Fig. 6.2(c)); we will refer to the former as 'diagonally magnetized' and the latter as the 'horse-shoe' state. Putting charged domain walls at all corners yields to a four-domain configuration. The four-domain state represents the highest energy, and it cannot be

produced by a homogenous external field. Hence it is rather unlikely to appear in observations.

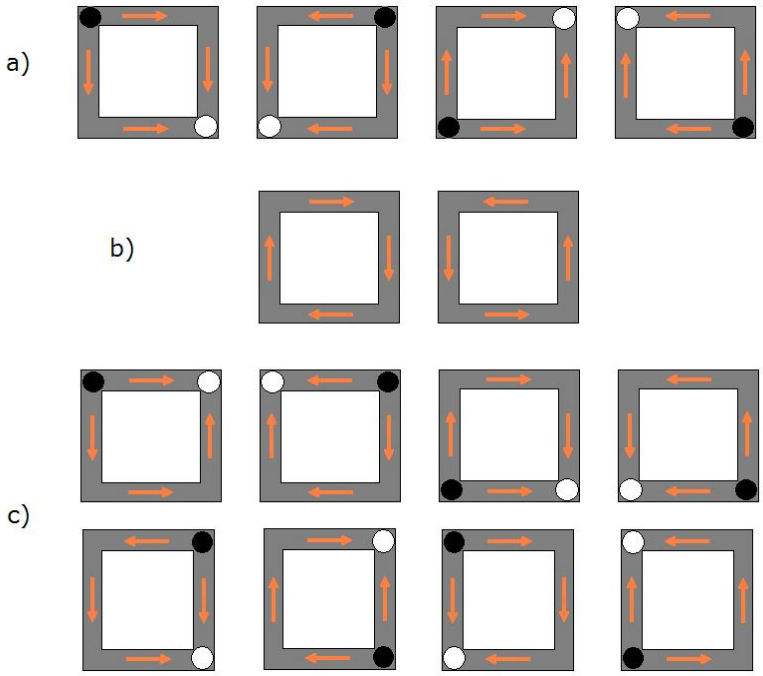

Figure 6.2 Schematic drawings of magnetic states of square-rings. The arrows represent the magnetization direction inside the rings, the black and the white spots represent tail to tail, and head to head domain walls respectively. (a) Diagonally magnetized, (b) flux-closure, and (c) horse-shoe states.

According to OOMMF simulations of our fabricated rings, a neutral wall with zero net charge contributes 190 eV to the total energy of a ring, while a charged wall contributes 402 eV [46]. Most of this energy comes from the demagnetizing term, while the contribution of the exchange energy is much smaller. The zero-field degenerate ground states of the system are the two flux-closure configurations. The most accessible configuration is the diagonally magnetized state, which can easily be produced from any other configuration by a diagonal field larger than 500 Gauss. The creation of domain walls requires relatively high energy, but their displacement involves only small fields

and energies. Domain walls initially present in the structure can move and annihilate each other, forming other domain configurations. MFM observations confirmed this simple, qualitative picture.

We demonstrated switching between magnetic states in a controlled manner in [46] also. In order to gain control over the domain-wall displacements, local fields should be applied that overwhelm the effect of pinning-field distributions. The simplest way to accomplish this is to fabricate magnetic elements in close proximity to the square rings such that the localized field of these nanoelements will be superimposed onto the homogenous external field. Figure 6.3(a) displays such a fabricated structure. The additional two rectangles were placed next to the ring with 40 nm separation. After magnetizing them along their longer axis, the rectangular magnets stay in a simple and stable single domain state with two oppositely-charged regions at their ends. Simple magnetostatic calculations show that the peak magnetic field generated by these rectangles at the corners of the square rings is around 200 Gauss; this value is definitely larger than the switching-field variations of the 'stand-alone' rings. We estimate the switching field of these rectangles (i.e., when their single-domain state is destroyed) to be approximately 300 Gauss, which is considerably larger than the value required for domain-wall displacement in the square rings. Hence, their magnetization remains intact during experiment, and they act solely as a 'driver' in this process providing well-localized magnetic fields for the rings.

The controlled switching process, as recorded by MFM, is illustrated in Fig. 6.3(b), (c) and (d). The initial state is a diagonally magnetized two-domain configuration, with the additional magnetic poles of the two uniformly magnetized rectangular elements.

This state was produced by a 4600 Gauss diagonally-oriented external magnetic field. As a result, there are three positively charged regions concentrated in the lower left corner in Fig. 6.3(b). Because of the demagnetizing effect of the additional poles, the positively charged domain wall of the ring is more mobile than the negatively charged domain wall in the opposite corner. In fact, the positively charged domain wall can be displaced by a 130 Gauss external magnetic field, which keeps the other domain wall intact. Figure 6.3(c) shows the result of this step, where the external field was applied vertically on the structure. As the left side's magnetization reversed, the ring switched to a horse-shoe magnetic state. At this point, the positively charged domain wall is stabilized in the upper left corner of the ring, due to the negatively charged magnetic pole of the vertical rectangular element. In the last step, a horizontally applied magnetic field is used to reverse the top side of the ring. During switching, the positively and the negatively charged domain walls annihilate each other, and the ring relaxes to a counterclockwise-rotating flux-closure domain configuration, as seen in Fig. 6.3(d). If opposite magnetic fields were applied at each step (including the initialization), a clockwise field would result. The control elements determine which wall moves first, and such control over the final state would not be possible without these coupler elements.

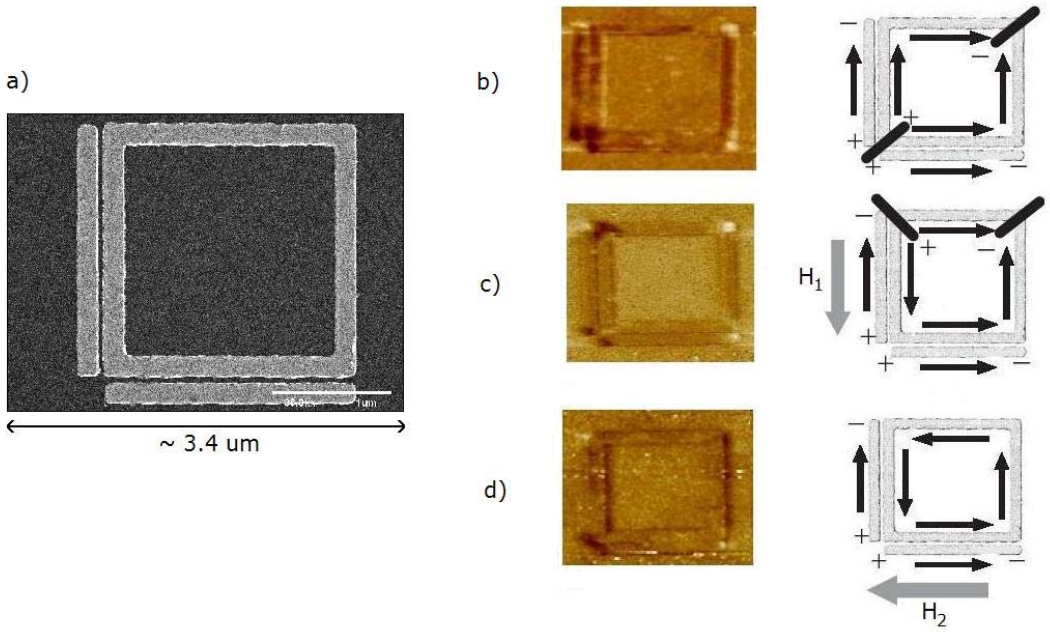

Figure 6.3 Controlled square-ring.(a) SEM micrograph of the structure. The purpose of the neighboring rectangles is to provide localized magnetic fields that influence the ring's switching characteristics. (b) MFM image and schematic of the magnetic state after initialization. The square-ring is in a diagonal state. (c) The vertically applied magnetic field reversed the left side of the ring and moved the tail to tail domain wall to the upper left corner. The square-ring is in a horse-shoe state. (d) The horizontally applied magnetic field reversed the top side of the ring and annihilated the domain walls. The square-ring is in a flux-closure state.

In the experiment described above, we presented an example of designed control of a simple micromagnetic system, namely square rings coupled to rectangular magnets. We have shown experimentally and theoretically that these rings can display a few qualitatively straightforward domain configurations, which can be transformed into each other via properly designed external field pulses. The rings can be designed in such a way that uncontrollable deviations from the perfect shape play only a little role in their operation.

6.2 Investigation of the flux-closure magnetic state in rings

As discussed earlier, the degenerate ground states of magnetic rings are the two flux-closure configurations. If the relaxation process can be controlled by other relaxing rings, then a network of such rings can perform QCA operation, with the digital bits '0' and '1' being assigned to the two flux-closure states.

The idea of storing binary information in magnetic rings comes from the era of magnetic core memories for computers in the early sixties. Even after the rise of silicon, ferrite cores of a size of a millimeter in diameter were utilized in certain applications [9]. At a thousand times smaller size, ring-like designs are attractive due to their low switching-field distribution, compared to other submicron geometries. Narrow circular rings were found to possess two types of stable magnetic states: polarized, so-called onion states (field lines split around the center in opposite directions with head-to-head and tail-to-tail domain walls at opposite sides), and totally flux-closed vortex states with clockwise and counterclockwise rotation (field lines encircle the center). Zhu et al. [47] proposed to use the chiralities of the vortex states (the rotation direction of magnetization) in circular rings as the carriers of information for data storage.

Micromagnetic simulations show that wide rings compared to the earlier-investigated narrow rings support only the two flux-closure magnetic states in remanence, which makes them eligible for implementing bistable switches. Figure 6.4 summarizes the simulated remanent states of an in-plane magnetized 800 nm outer diameter ring with varying width. In the case of the narrowest ring in Fig. 6.4(a), the remanent state is the onion state. In wider rings (with large outer and inner circle

diameter ratio) the domain walls are expected to undergo a transition from a transverse domain wall of head-to-head domains to a local vortex structure. This transition was predicted by McMichael and Donahue [48] for the case of magnetic strips. The formed vortex cores can provide a stable magnetization as shown in Fig. 6.4(b). However, if the vortex cores are not constrained by local shape anisotropy, they can move along and be annihilated on the borders, and as a result, wide rings are able to relax to flux-closure remanent state as the external field is removed (Fig. 6.4(c)). This work was presented in [49].

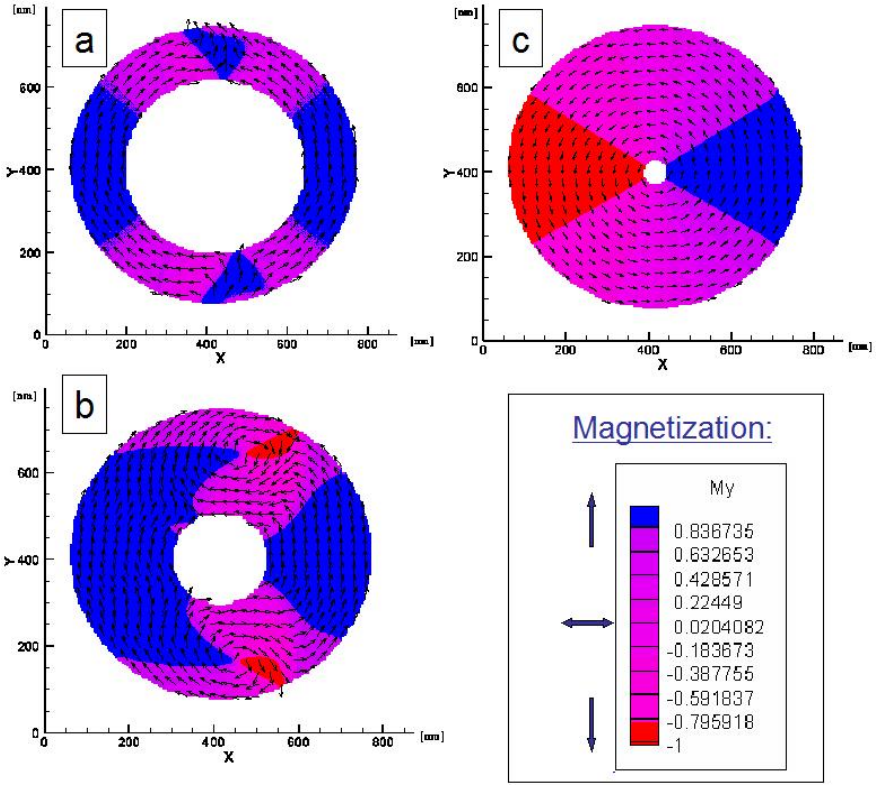

Figure 6.4 OOMMF simulation of remanent states as a result of relaxation from fully magnetized state in plane: (a) onion state, (b) vortex-core state, and (c) flux-closure state.

For providing flux-closure magnetic states in remanence, thus, the magnetic element has to be either a wide ring or a disk.

However, for the disk-shape element, the flux-closure magnetization can be maintained only if the element is sufficiently large. When the disk diameter is reduced, the exchange energy becomes comparable to the magnetostatic energy, and the disk becomes single domain. Different hysteresis curves that show different switching behavior for various disk sizes were measured by Cowburn [50]. In Fig. 6.5 we show simulated hysteresis curves for permalloy disks with 10 nm thickness in three sizes: 900, 300 and 100 nm diameters. The external magnetic field is applied in the x direction, in the plane of the disks. A 100 mT applied field can completely saturate the disks in the direction of the field. As the field is reduced, reversed, and increased to 100 mT to the opposite direction, the 300 nm and the 900 nm disks switch their magnetization through a vortex domain structure, while in the 100 nm diameter disk the elementary magnetic moments rotate around coherently, which is called single-domain behavior. In Fig. 6.5(d) ranges of single-domain and multi-domain magnetic behavior of the spherical geometry are given as a function of sphere diameter (D) after Cullity [51]. Particles with diameters close to D_S are between the single-domain and the multi-domain region, and can be referred as quasi-single domain magnets. Quasi-single domain particles have single domain remanent state, but the magnetization reversal occurs through domain wall (ie. vortex-core) formation, propagation, and annihilation. The formation of the vortex-core takes a relatively large amount of energy that is provided by the external field. As the particle size is increased into the multi-domain region, the magnetostatic energy overcomes the exchange term, and domain wall(s) will exist already in the remanent state. This is the case with the 900 nm diameter disk in Fig. 6.5(c). With decreasing particle size in the single-domain region, the external field that required flipping the

magnetization is decreasing as well, simply because the overall magnetic moment of the sphere becomes smaller, as seen in Fig. 6.5(a) for the 100 nm diameter disk. Hence, the highest coercivity fields correspond to quasi-single domain spheres, such as the one with 300 nm diameter in Fig. 6.5(b).

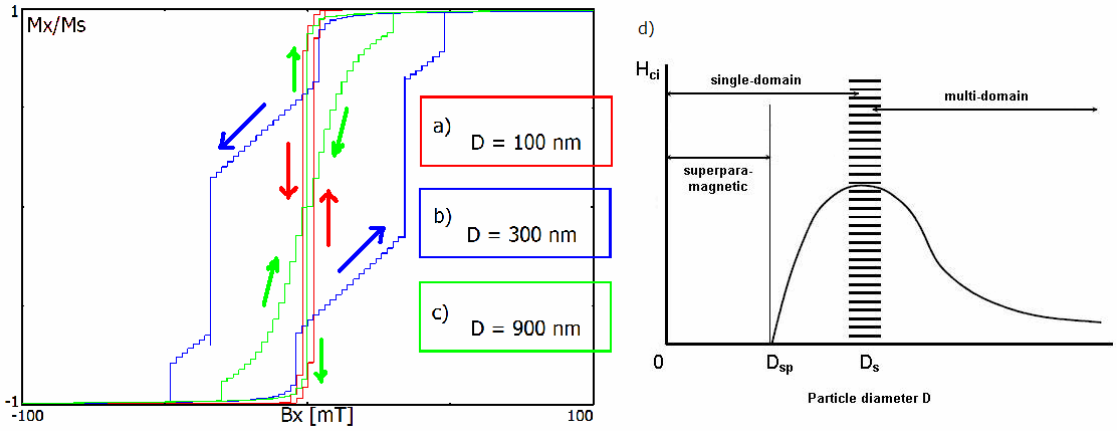

Figure 6.5 (a)-(c) Normalized magnetization vs applied magnetic field: simulated hysteresis curves of permalloy disks. (d) Schematic variation of intrinsic coercivity Hci with particle diameter D after Cullity [51].

The smallest diameter size of disks that support a flux-closure state in remanence is somewhere between 300 nm and 900 nm in the above simulation. The smallest diameter size of annular dots that support flux-closure state in remanence is smaller than for disks. This is because the introduction of the inner edge reinforces the circular magnetization by shape anisotropy. In conclusion, in the size of 500 nm and below, rings are the best candidates for computing elements that switch between two flux-closure states.

The problem with using the bi-directional flux-closure state for field-coupled QCA applications is the lack of fringing fields. We proposed to physically connect submicron annular dots instead of placing them near each other with a finite separation [49]. It was found earlier [52] [53] that the magnetization process of chains of micron-size touching

rings displays a clear anisotropy. For applied magnetic fields perpendicular to the chain direction, the switching occurs pair-wise. For fields applied parallel to the chains, the switching of the edge ring element triggers the switching process, and extended sections of the chains were found to switch simultaneously. In these sections, neighboring rings display vortices of alternating chirality similar to the interlocking gears in gear trains as shown in Fig. 6.6(b). A chain of touching rings switching into alternating vortex states can be seen as an inverter chain and represents the basic digital computation.

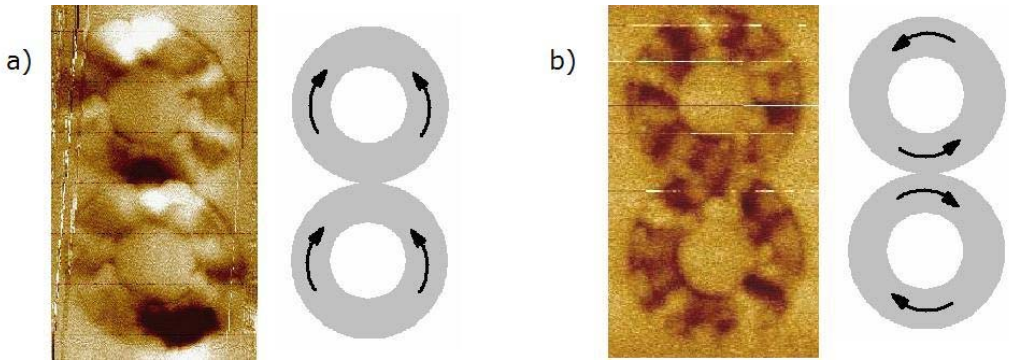

Figure 6.6 MFM image and schematic magnetization of (a) onion states and (b) flux-closure states of two exchange-coupled 250 nm wide, 25 nm thick permalloy rings (contrast in flux-closure state is due to magnetic ripples).

However, with the application of touching (i.e. exchange-coupled) rings, we are outside of the focus of this dissertation on field-coupled QCA architectures.

CHAPTER 7

DIPOLAR COUPLING OF SINGLE-DOMAIN NANOMAGNETS

Magnetostatic interaction between planar, circular nanomagnets in arrays with varying spacing was studied by Cowburn [54]. Figure 7.1 summarizes the experiment. The nanomagnets were made of 7 nm thick layer of $Ni_{80}Fe_{14}Mo_5$ ('supermalloy') by means of electron-beam lithography and lift-off. In this experiment, the magnetization of the dots is oriented in the plane. Modulating the lattice spacing in one direction can cause fundamental changes in the behavior of the array. In Cowburn's description, a nanomagnet can be analogous to a single giant atom of a "new magnetic element", and "new artificial magnetic materials" can be constructed from a lattice of these artificial atoms. He demonstrated that the magnetic properties of a lattice of nanomagnets can be profoundly changed by scaling the magnetostatic interactions between nanomagnets within the lattice. The lattice of giant spins can change from a magnetically disordered state to an ordered state as the lattice parameter is decreased. The effect appears in the measured hysteresis loops. In panel (d) hysteresis curves for X=180 nm and X=120 nm show the lattice to be magnetically disordered. The hysteresis curve for X=90 nm show the lattice to be magnetically ordered, with a magnetic easy axis in the direction of the chains and a magnetic hard axis perpendicular to the chains. For X=100 nm the array is near to the transition point between an ordered and disordered lattice.

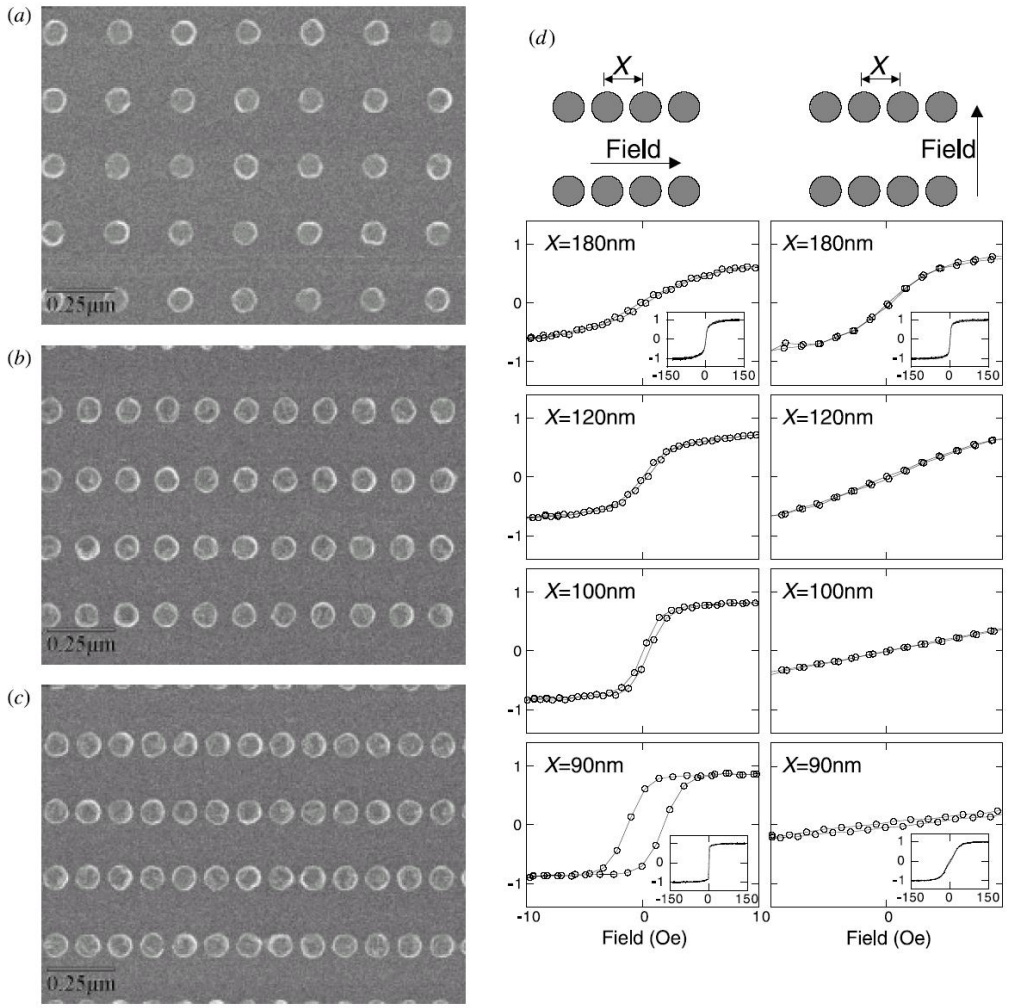

Figure 7.1 Scanning electron micrographs of some of the nanomagnet lattices studied by Cowburn [54]. Each nanomagnet is of 60 nm diameter and has a y-direction lattice parameter of 180 nm. The x-direction lattice parameter is (a) 180 nm, (b) 110 nm and (c) 90 nm. In (d), measured hysteresis loops for different lattice spacing (X) and applied field directions. All loops were measured within the field range ±150 Oe: the large panels show high-magnification views around zero field; insets show the full measured loop. The vertical axis of all loops is magnetization normalized by the saturation value.

Cowburn's experiment examined magnetostatic coupling between the nanomagnets (especially, but not exclusively, between nearest neighbors), which becomes stronger as the separation of the dots (X) is reduced. This is directly analogous to the onset of ferromagnetism in an atomic lattice.

The lesson is the following: in the case of interacting arrays, the magnetic ground state of the magnets can be different from their isolated ground state. If the magnets are placed close to each other in the array, the coupling between them will be strong, and the array will exhibit the collective behavior of the magnets.

The evidence that networks of interacting submicrometer magnetic dots can be used to perform logic operations and to propagate information at room temperature was demonstrated by Cowburn in 2000 [16]. The QCA concept was applied to nanomagnets for the first time in this work.

In this demonstration [16], the logic states are assigned to the magnetization direction of single-domain, disk-shape supermalloy dots, each of diameter 110 nm, with 10 nm thickness. The disks are arranged into chains in which they are ferromagnetically coupled to their nearest neighbors through magnetostatic interactions. The separation between the dots in the chain is 20 nm. Magnetic solitons carry information through chains of 69 circular dots driven by an elongated additional input dot, and an applied oscillating magnetic field provides energy to the system and serves as a clock. Figure 7.2 shows SEM images of two of the fabricated chains.

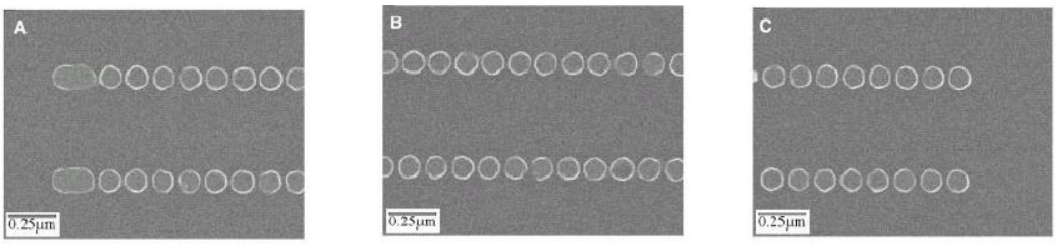

Figure 7.2 Scanning electron micrographs of the left (A), center (B), and right (C) regions of two ferromagnetically-coupled chains of circular nanomagnets. From Cowburn [16].

The experimental setup was the following: the chains are inspected by magneto-optical measurement based on the longitudinal Kerr effect. This is done by measuring the polarization state of a reflected linearly-polarized laser beam that is focused on the chains. The plane of incidence of the light is set to lie along the length of the chains. The laser spot covers almost the entire 9-mm length of the networks, and so the recorded signal is a measure of the total component of magnetization lying along the chain of dots and, once correctly calibrated, is a measure of the number of dots switching in a network. The elongated input dots are set by applying a single magnetic field pulse of either +300 Oe (for a logic 1) or -300 Oe (for a logic 0) directed along the chain of dots. A weak oscillating magnetic field of ±25 Oe amplitude and 30 Hz frequency combined with a -10 Oe bias magnetic field is then applied along the chain of dots. The magneto-optical signal from the networks is recorded over several cycles.

It was found that almost the entire chain of 69 dots is switching as the solitons sweep along the chains.

A computational study using the Landau–Lifshitz magnetization dynamics into the dynamic properties of a magnetic soliton on a chain of above described single-domain nanomagnets was published in [50] by Cowburn. A simulation result is shown in Figure 7.3 that predicts a possible uniform soliton velocity of approximately 1000 m/s, and a nanomagnet reversal time of 240 psec.

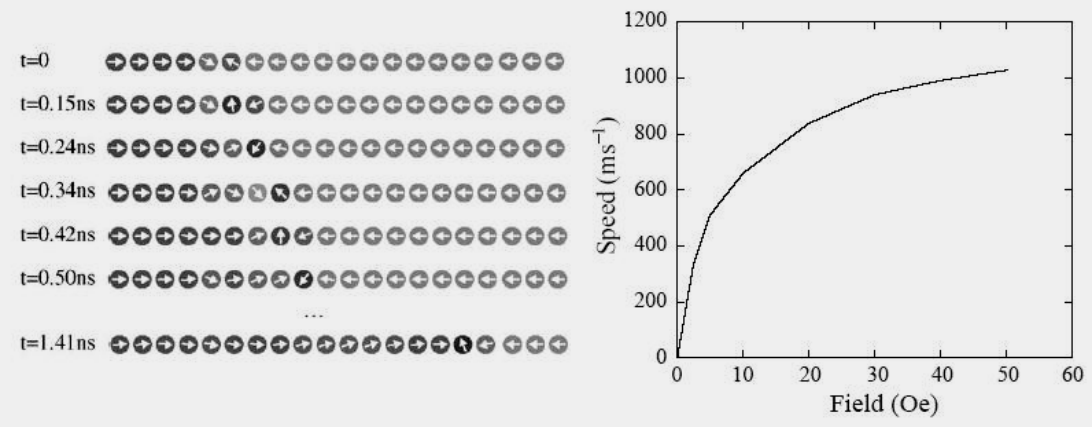

Figure 7.3 Calculated evolution of a soliton propagating along a chain of coupled nanomagnets under the action of a 30Oe field applied from left to right in x-direction, and the calculated propagation speed of the soliton as a function of applied field strength.

We have seen that ferromagnetically-coupled disk-shape nanomagnets can be applied in QCA-type systems.

Single-domain, circular nanomagnets with additional uniaxial anisotropy transverse to the chains show more complex behavior, as summarized in Fig. 7.4 after Cowburn [55]. The three simplest configurations are considered here: ferromagnetic lateral (FL), ferromagnetic transverse (FT), and antiferromagnetic transverse (AFT). The energy of each configuration, U, consists of two terms: uniaxial anisotropy energy (K_U) and dipolar coupling energy (J).*

If the uniaxial anisotropy is weak, then the most favorable configuration is the ferromagnetic lateral. The uniaxial anisotropy has to be larger than J for antiferromagnetic ordering of the magnetic moments to occur.

* J is defined here as the dipolar coupling energy between two antiparallel magnets.

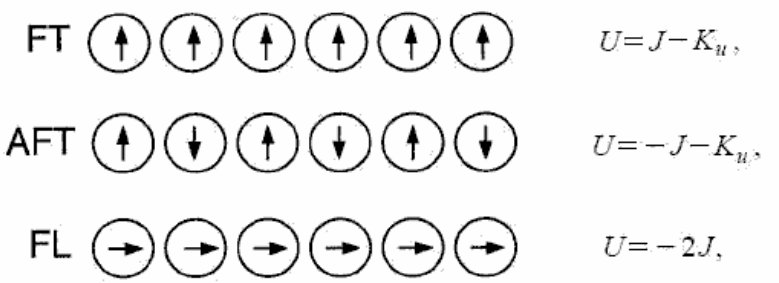

Figure 7.4 Ferromagnetic transverse (FT), antiferromagnetic transverse (AFT) and ferromagnetic lateral (FL) configurations of single-domain, disk-shape nanomagnets with uniaxial anisotropy transverse to the chain (after Cowburn [55]).

Slightly elongated supermalloy nanomagnets with sizes of 100 nm x 120 nm, and with thickness of 10 nm were shown by Cowburn in [55] to prefer the antiferromagnetic transverse configuration. Representative chains of the fabricated sample can be seen in Fig. 7.5(a), (b), (c) and (d). An alternating and decaying external magnetic field transverse to the chains was used for demagnetization, and the final magnetization of the chains was checked by magneto-optical Kerr measurements. The largely elongated nanomagnet at the left end of the chains was used as an input, as their magnetization remained intact during the demagnetization process. The experimentally determined antiferromagnetic ordering parameter measured for different numbers of nanomagnets (n) in the chains is plotted in Fig. 7.5(e). From this plot, the antiferromagnetic ordering length was found to be 4 or 5 nanomagnets. This relatively small number was explained by a frustration-propagation model, in which the ordering process was claimed not to be well supported by the external demagnetizing field, unlike in the case of the ferromagnetically-coupled circular dots introduced earlier.

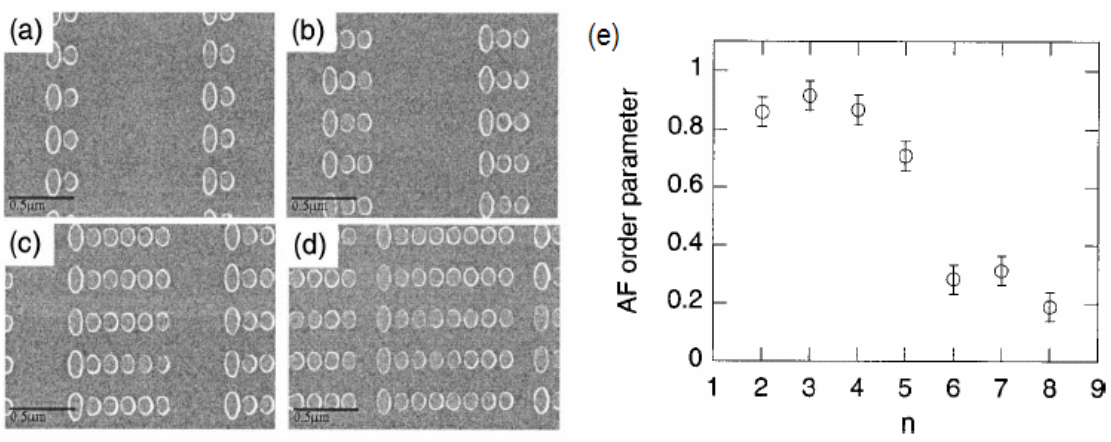

Figure 7.5 Antiferromagnetically-coupled chains of (a) one, (b) two, (c) five, and (d) seven nanomagnets fabricated by Cowburn [55]. (e) Experimentally determined ordering parameter as a function of nanomagnet-number (n) in the chains.

As we will show in the next chapters, the antiferromagnetic ordering length indeed can be improved by choosing an appropriate demagnetizing method, and by introducing more complex nanomagnet shapes.

CHAPTER 8

SHAPE ENGINEERING OF NANOMAGNETS

The shape design of the nanomagnets is a very important part of this study because the shape anisotropy that we introduce to the dots is the one mainly responsible for the switching dynamics when interplaying with the external clock-field and the stray field of the neighboring dots. If the switching dynamics can be controlled, then the most fundamental requirement of the MQCA systems will be satisfied, i.e. each elementary building block will operate reliably.

8.1 Investigation of the quasi single-domain size

As we have seen before, nanomagnets have four ranges of volume size: superparamagnetic, true single-domain, quasi single-domain and multi-domain sizes. Nevertheless, these ranges cannot be unambiguously determined for a given ferromagnetic material due to the strong influence of the shape, stress and crystalline anisotropies on the domain structure.

For a simple demonstration of the effect of shape, we have fabricated samples of differently shaped and sized permalloy elements. After demagnetization, the samples were imaged by MFM with no external field present. Figure 8.1 shows 4 x 12 arrays of elliptical, rectangular and triangular shapes. In the four rows, the lengths of the elements'

vertical axes are: 2, 3, 4 and 5 μm. In the 12 columns, the lengths of the elements' horizontal axes vary between 450 nm and 3 μm. The thickness of the evaporated permalloy is 25 nm. The separation between the elements is more than a micron, so it is assumed that the coupling between them is negligible.

On the left side of the rows, the elements are in the single-domain magnetic state, as only two strong contrast dark and bright spots can be seen for each (except the first row of Fig. 8.1(b)). The spots correspond to the magnetic South and North poles. Along the rows to the right, the length of the horizontal axis of the elements is increasing, and at some point, the single-domain configuration is replaced by a multi-domain configuration. In multi-domain state, the MFM contrast is generated by the domain walls. The elliptical shapes develop two, the rectangular shapes develop four, while the triangular shapes develop three domains in the multi-domain states of these samples. Note that the number of domains can be increased for the same patterns if the thickness of the elements (ie. the third dimension) is increased.

Looking at the columns, however, the increasing length of the vertical axis ensures the single-domain configuration. Even though the additional volume increases the magnetostatic energy of an element, which tends to break up the magnetization configuration into domains, the anisotropy of the elements is also increased, and has a stronger effect. This because the elementary moments at the boundary of the magnets align with the edge of the body (shape anisotropy). In fact, it is the aspect ratio between the length of the two lateral axes that matters as mentioned by Zhu et al. [56].

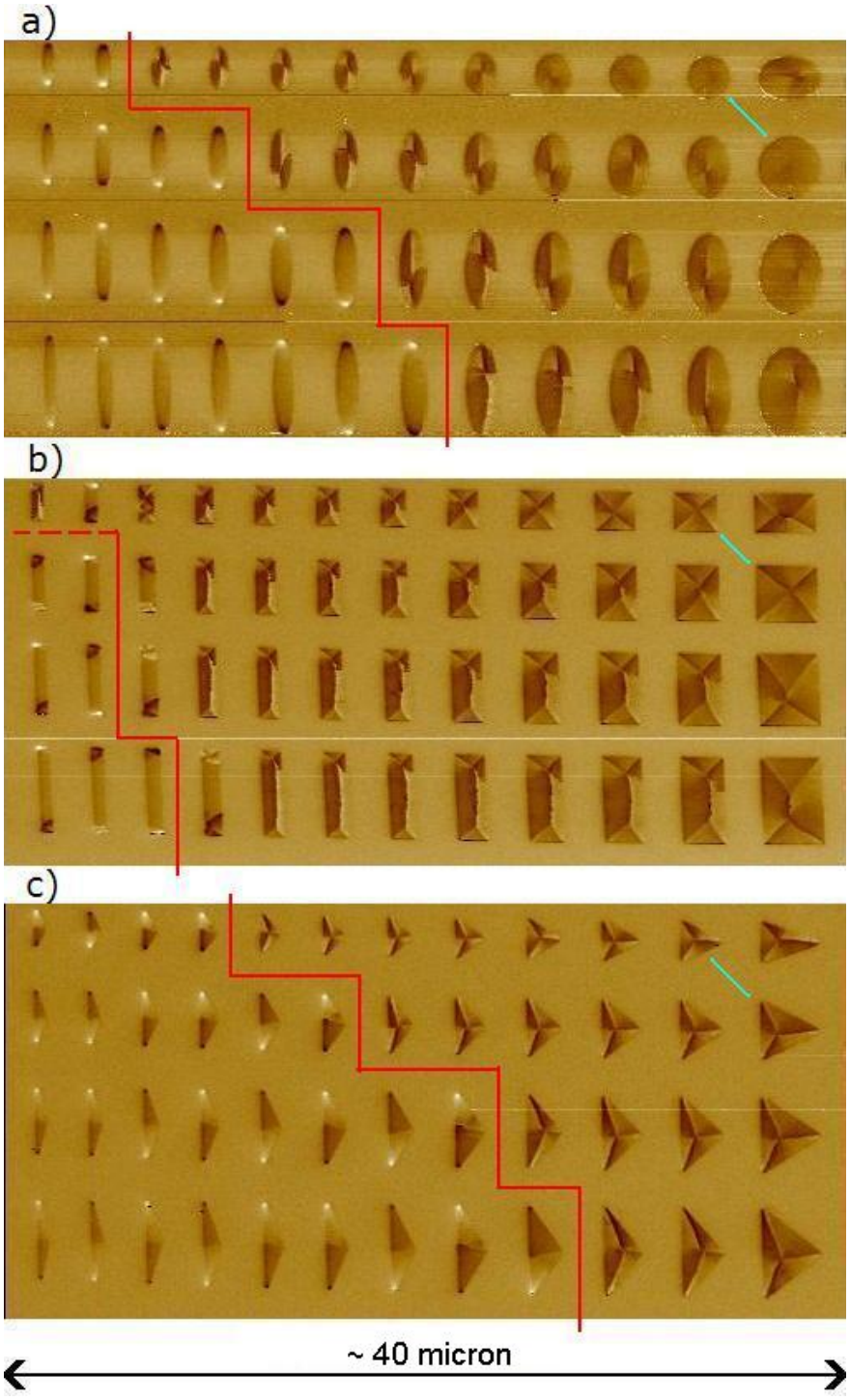

Figure 8.1 MFM images of arrays of differently shaped planar permalloy magnets in various sizes. The red lines mark the transition between single-domain and multi-domain remanent state. The green lines mark the two elements with 1:1 aspect ratio of axes in each array.

Another important observation is that the pointed ends of the elongated elements, like for the elliptical or for the triangular shapes, can also encourage the single-domain state.

Due to our limitations in lithography resolution, the majority of our studies were done on quasi single-domain nanomagnets with around 100 nm width. At this size, we found that an aspect ratio (length/width) of 2 is sufficient to ensure single-domain remanence. Wider magnets might need larger aspect ratio, unless their ends are pointed.

Note that closely spaced nanomagnets can show ordering in their magnetic patterns, even if they develop multi-domain configuration in remanence. See Fig. 8.2 for example.

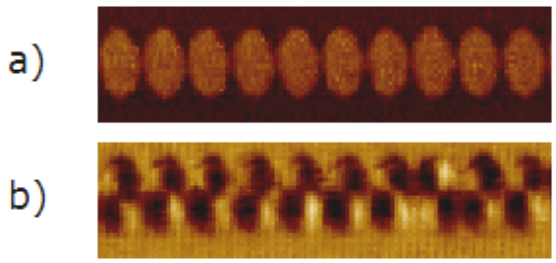

Figure 8.2 Multi-domain, closely spaced cobalt dots show ordering in their magnetic pattern. (a) AFM, and (b) MFM image of a 10-dot long chain.

8.2 Effects of shape on the magnetization reversal of quasi single-domain nanomagnets

Elongated triangular elements are especially interesting due to their asymmetry on the magnetic easy axis. The assymetry can provide different sensitivity to local fields on the two different sides, which for example, can define a preferred direction of the antiferromagnetic ordering process in a chain of such dots. From our viewpoint of MQCA, this is equal to rectified signal propagation along the chain. Our simulations

show such a phenomenon, however we did not have an appropriate experimental setup with which to confirm the dynamics.

Figure 8.3 demonstrates the relaxation of pairs of nanomagnets, one with an asymmetric trapezoid shape, and one with a symmetric rectangle shape. The coupling is through an approximately 10 nm separation between the magnets in both pairs. A horizontal external field of 200 mT is applied on the pairs in Fig. 8.3(a) and (b), which forces the magnetization to point along the hard axis of the nanomagnets. The rectangles are almost uniformly magnetized under this field, except at the 'outer' corners, where the magnetization is slightly pinned. The 'inner' corners (the corners that are next to the other magnet) are not pinned because the elementary magnetic moments at the boundary of the two magnets couple ferromagnetically. As the external field is removed from the rectangle-shaped dots, in Fig. 8.3(d), (f) and (h), the two magnets switch together, as if one's magnetization would be a mirrored image of the other's. In contrast, the two trapezoids show different relaxation dynamics. The reason is that the two sharp corners are on the 'inner' side of the pairs for the nanomagnet on the left, while they are on the 'outer' side for the nanomagnet on the right. The corners on the 'outer' side are pinned more strongly. As the external field is removed, in Fig. 8.3(c), (e) and (g), the more weakly pinned nanomagnet on the left starts the switching, and induces the final state of the nanomagnet on the right.

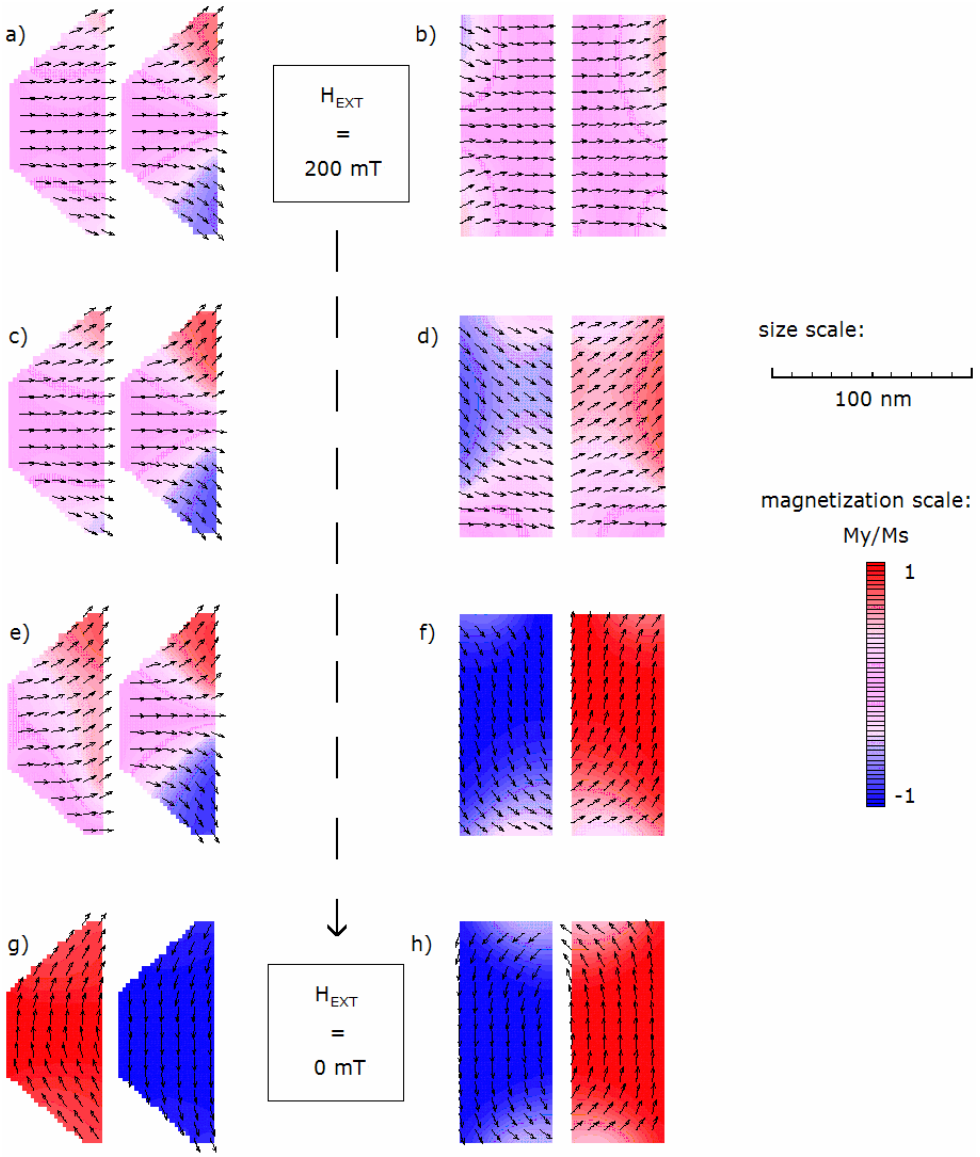

Figure 8.3 Simulated relaxation of coupled pairs of two trapezoid-shape and two rectangle-shape permalloy nanomagnets. The color is coded to the normalized magnetization vector's vertical component (*My*), and the arrows point in the direction of the local magnetization.

Note that when the external clock-field is oriented along the magnetic hard axis, assymetry introduced in shape on the magnetic easy axis can possibly enhance the performance of nanomagnet networks. However, assymetry in shape on the magnetic hard axis may not be allowed to avoid preferential magnetization switching that would be introduced by the external field.

We performed an experimental shape study by investigating chains of antiferromagnetically-coupled permalloy nanomagnets in the sizes of 75, 95, and 125 nm for the short axes and three aspect ratios of 2, 2.5, and 3. These magnets exhibit a magnetic easy axis along the direction of their long axis. As a general rule, we found that shapes with well-defined nucleation sites (i.e. sharp corners) for domain walls can control magnetic domain formation during magnetization reversal, making the switching process more predictable and resulting in longer correlation lengths in arrays of coupled nanomagnets [57]. In other words, switching-field variations that arise from fabrication variations, like the imperfect shape or rough surface of the dots, may be overcome to some extent by means of fault-tolerant shape design. For a representative example of the idea of fault-tolerant design see Fig. 8.4. In this shape, the pointed corners focus the magnet's stray-field.

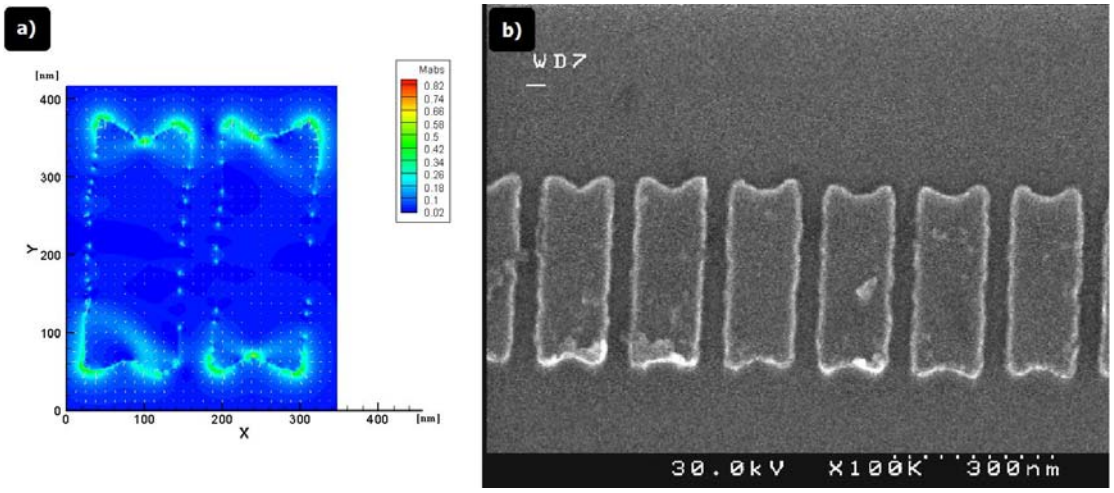

Figure 8.4 Coupled planar nanomagnets with sharpened corner. (a) Simulated stray field of two coupled dots, and (b) SEM image of a corresponding chain of permalloy dots.

Corners can also be used to ensure single-domain remanent magnetization for nanomagnets with lower aspect ratio. In Fig. 8.5(b) and (d), MFM images of chains of cornered and rounded nanomagnets are introduced. Each MFM image shows three

chains of 64 dots. The width of the dots is 125 nm in each chain, while the aspect ratio of the nanomagnets is 2 for the top chain, 2.5 for the middle chain, and 3 for the bottom chain. SEM images of the bottom chains are shown in Fig. 8.5(a) and (c). The MFM images were taken after demagnetization of the samples. As seen in Fig. 8.5(b), in case of the rounded shape even the aspect ratio of 3 was not sufficient to keep every nanomagnet in the bottom chain single-domain. On the contrary, for the cornered rectangular shape, the aspect ratios 3 and 2.5 were both sufficient.

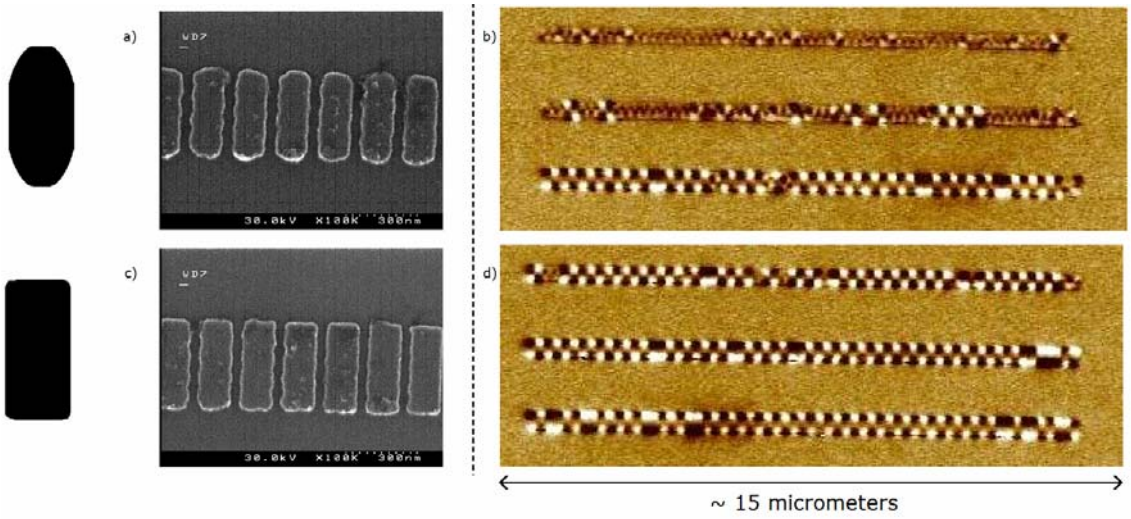

Figure 8.5 Study of two different shapes. (a) and (c) are SEM images of a section of the investigated chains with the highest aspect ratio nanomagnets. (b) and (d) are MFM images of three 64-dot long chains with different aspect ratio nanomagnets.

Being much simpler systems than the chains, we fabricated and studied pairs of coupled nanomagnets, which we refer to as double-dots. Double-dots have four possible magnetic configurations assuming that the nanomagnets are single-domain. An applied magnetic field along the longer axis of the nanomagnets can set both domains parallel, as shown in Fig. 8.6(b). This is a metastable state of the double-dot. In the ground state, the magnetization of the domains is antiparallel due to the dipole coupling. The ground state

can be produced by demagnetizing the double-dot, for example by a rotating external magnetic field that is slowly reduced from a high level to zero.

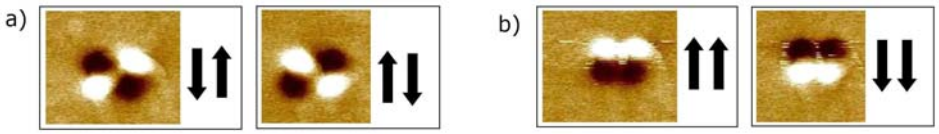

Figure 8.6 MFM images show the four possible magnetic states of two coupled, planar single-domain nanomagnets. The arrows represent the magnetization direction inside the nanomagnets. (a) The two antiparallel magnetic configurations, and (b) the two parallel magnetic configurations.

We have investigated arrays of double-dots that are shown in Fig. 8.7. Each array is divided into two halves in which the asymmetric shapes we studied are oriented oppositely. Double-dots in a row are designed identically, and each six rows in a half-array have a different size. We performed rotating-field demagnetization on the arrays, and took MFM images. We have found that the different shapes develop different numbers of parallel configurations of the double-dots. Moreover, the parallel configurations tend to appear at the same double-dots when the demagnetization process is repeated. This suggests that the parallel configurations do not develop randomly, but are related to the actual geometry and physical structure of the double-dots. Variation of the physical structure from double-dot to double-dot is a result of our fabrication technology, which randomly alters the design. Assuming that the 'fabrication variations' are distributed evenly in each array, we can state that the different asymmetric shapes we studied have different sensitivities to fabrication variations.

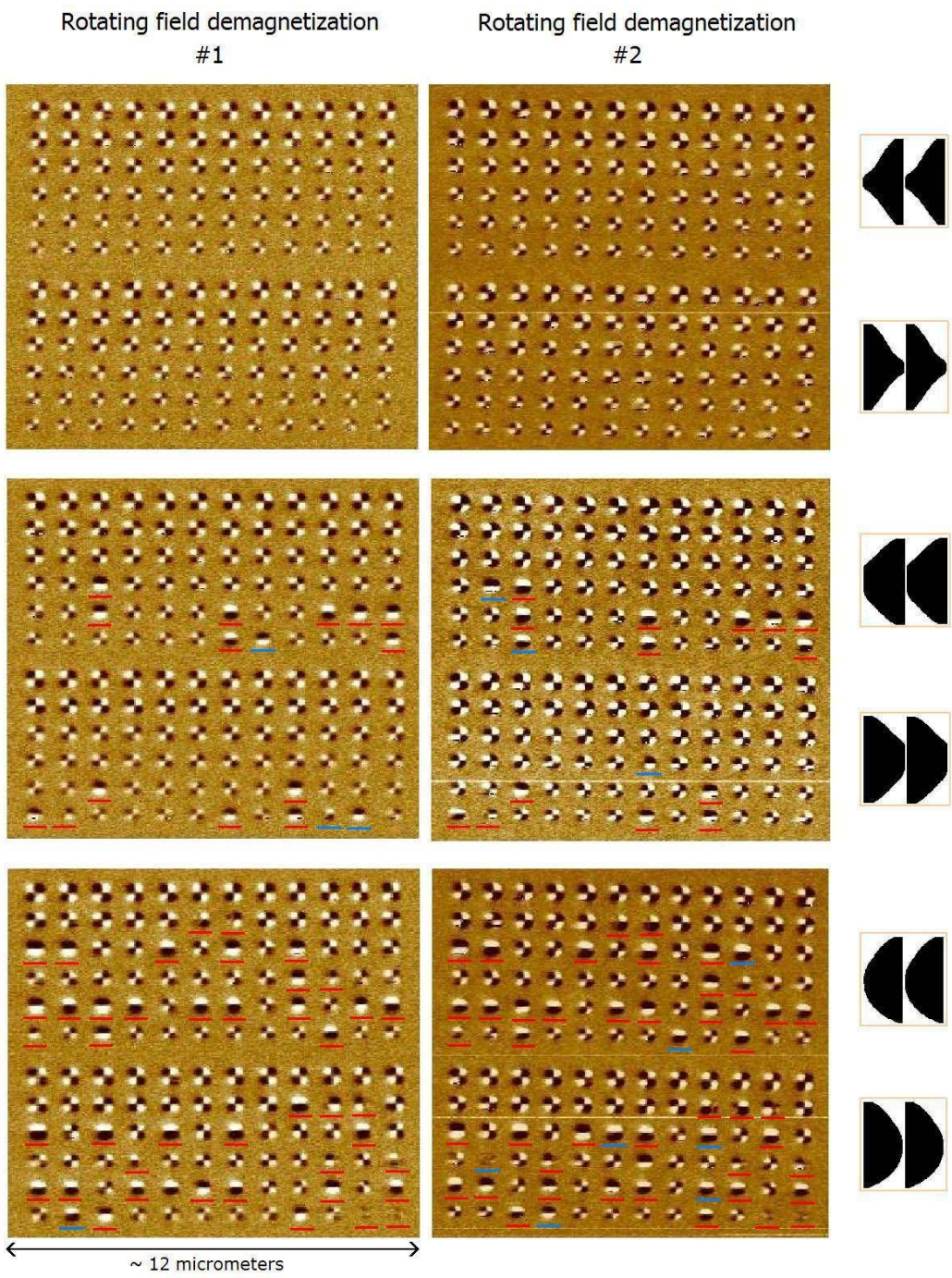

Figure 8.7 Repeated rotating-field demagnetizations of double-dot arrays reveal that different shapes can show different sensitivity to fabrication variations. The parallel magnetic configurations (and configurations with multi-domain states) are underlined with red if they appear as a result of both independent demagnetizations at the same double-dot. The rest of the parallel magnetic configurations (and configurations with multi-domain states) are underlined with blue.

In addition to the nanomagnet-shape dependence of the magnetic configuration of a coupled system in ground state, we also found a dependence on the demagnetization process. Figure 8.8 illustrates an experiment in which chains of two different shapes were demagnetized by using two different demagnetizing methods. The MFM images were taken on 9 chains of 64 antiferromagnetically-coupled permalloy nanomagnets with sizes of 75, 95, and 125 nm for the short axes and three aspect ratios of 2, 2.5, and 3 for each width. To compare the performance of the 'I'- and the 'H'-shaped nanomagnets, see the bottom three chains with 125 nm magnet-width first. The blue arrows mark sections of the bottom three chains where either parallel alignment of two neighboring magnets or multi-domain magnetization of a magnet occurred. These are 'errors' of the antiferromagnetic ordering. In the case of rotating-field demagnetization, there are 8, 14 and 10 'errors' in Fig. 8.8(a) for the aspect ratios 2, 2.5 and 3 respectively. This gives an average of 10.6 'errors' in the inspected chains, which results in an approximate average ordering length of 6 nanomagnets by simply dividing the whole length of 64 by 10.6. While this calculation results in an approximate average ordering length of 6 nanomagnets for the 125 nm wide 'I' shapes, it gives an average ordering length of 19 for the 125 nm wide 'H' shapes. This is a remarkable difference. Repeated independent rotating-field demagnetization of the samples produced similar results. However, when applying horizontal clock-field on the chains, the 'errors' appear in different number. While the average ordering length of the 125 nm wide 'I' shapes had increased to 16, in the case of the 'H' shapes it decreased to 0 basically, due the evolving multi-domain magnetization of the dots. Even for the 75 nm wide 'H' shapes (in Fig. 8.8(d) upper three

chains), which maintained single-domain state, the number of ‘errors’ increased significantly as compared to rotating-field demagnetization.

The difference between the two demagnetizing methods is that while the horizontal clock field is applied exclusively along the magnetic hard axis of the dots, the rotating-field demagnetization process introduces external field in all directions, and most probably acts along the magnetic easy axis of the dots. The geometry of the ‘I’ shape may support the horizontal external field by shape anisotropy originating from the straight top and bottom side of the nanomagnets. On the contrary, the ‘H’ shape has no side parallel to the horizontal clock-field, but has a relatively large percentage of its boundary oriented vertically, parallel to the magnetic easy axis, along which the rotating-field demagnetization acts.

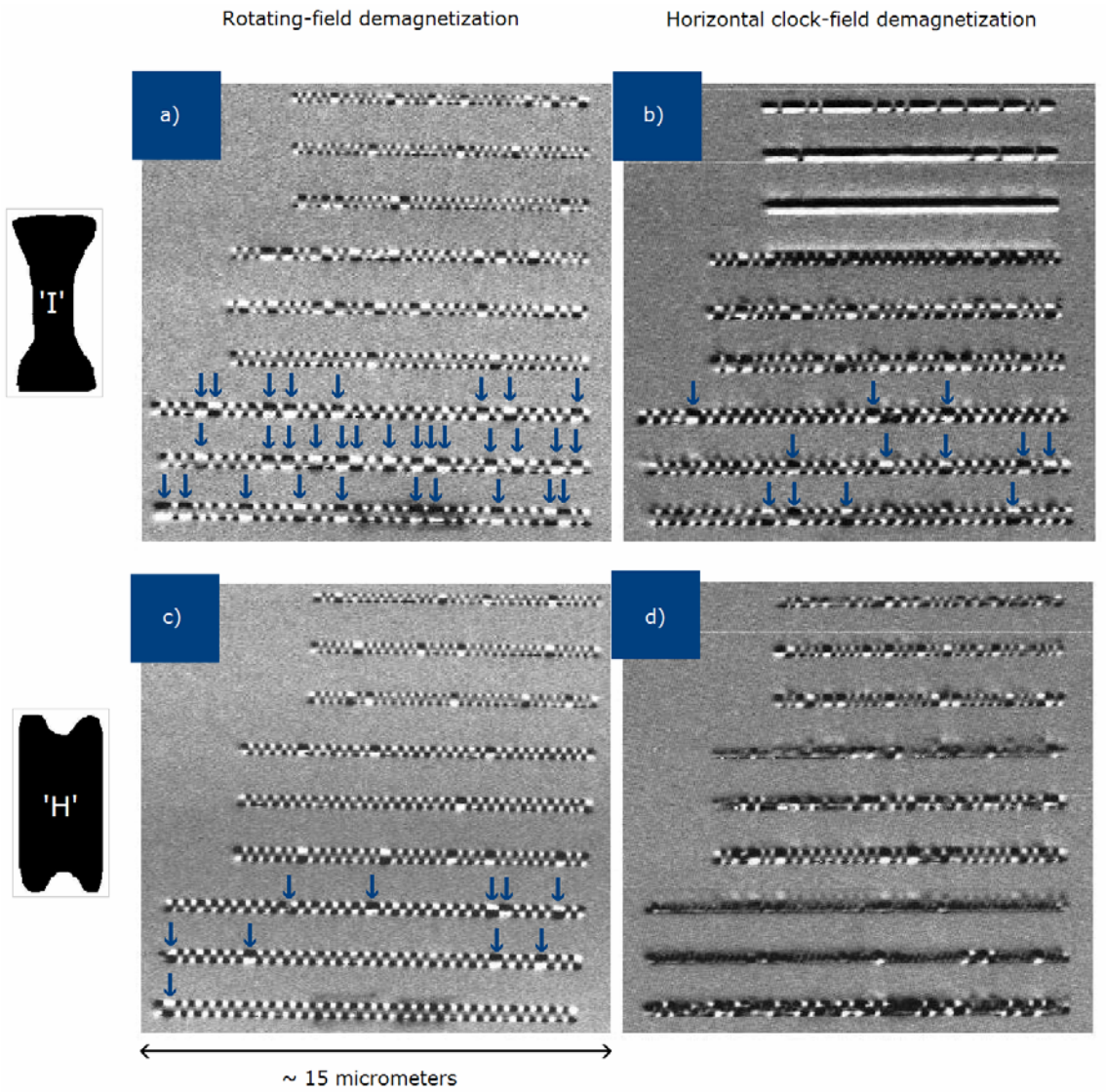

Figure 8.8 Two samples with different nanomagnet-shapes show different magnetic configurations when demagnetized by a decaying rotating field (a) and (c) or by a horizontally applied clock-field (b) and (d). (a) and (b) MFM images were taken on the same 9 chains of nanomagnets with 'I' shape, and (c) and (d) with 'H' shape. In (a), (b) and (c), the blue arrows mark sections of the bottom three chains where either parallel alignment of two neighboring magnets or multi-domain magnetization of a magnet occurred. In (d), most of the nanomagnets show multi-domain magnetization in the bottom three chains.

In conclusion, both the nanomagnet shape and the demagnetizing process have to be considered together for specific operations of nanomagnet networks.

8.3 Correlation lengths of antiferromagnetic ordering along chains of coupled nanomagnets

The antiferromagnetic ordering length in chains of coupled nanomagnets was first studied by Cowburn [55]. It was found that the antiferromagnetic arrangement of the magnetic moments in chains of 100 x 120 nm sized, 10 nm thick, slightly elongated permalloy dots with a separation of 15 nm lasted not longer than only 4-5 dots.

We investigated extending the antiferromagnetic ordering length in different samples. For cobalt nanomagnets at the size of approximately 120 x 250 nm, 25 nm thick, with a separation less than 25 nm, experimental data demonstrated a long-range ordering of an average 7-8 dots, often reaching 20-30 dots [58]. This is significantly larger than previously published.

In other work, we fabricated 30 nm thick permalloy dots in 9 different sizes: 75, 95, and 125 nm widths and three aspect ratios of 2, 2.5, and 3. We designed 64-dot long chains, with a separation approximately 40 nm between the nanomagnets. Both rotating-field demagnetization and adiabatic clock-field demagnetization were tested on the sample. We have shown that ordering persists over chain lengths of some 20 dots [57]. On some occasions we found whole chains in a perfectly ordered antiparallel configuration, such as the one in Fig. 8.9.

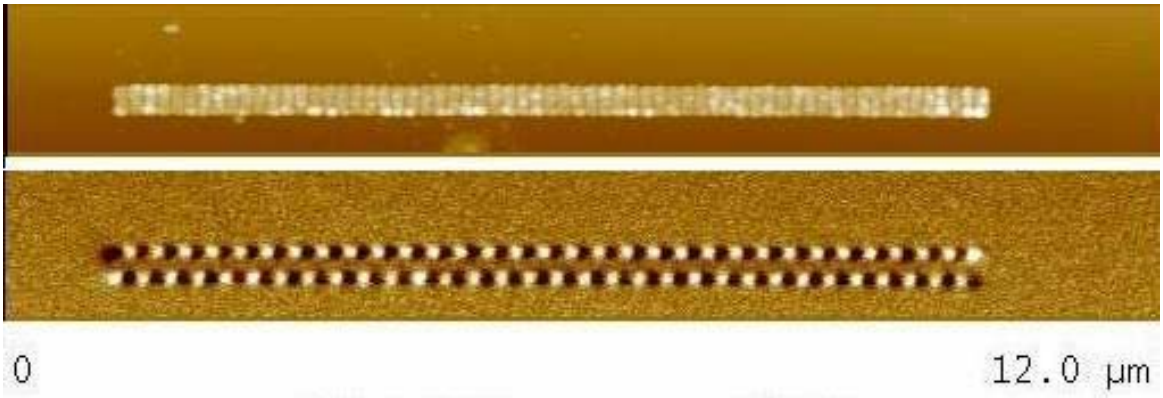

Figure 8.9 AFM and MFM micrograph of a chain of 64 permalloy nanomagnets. The perfect antiferromagnetic ordering was achieved by rotating-field demagnetization.

Even though with special shape designs we could achieve fairly large ordering lengths of 20-22 nanomagnets in our antiferromagnetically coupled chains, avoiding fabrication defects remains an important and critical issue. However, from the prospective of future MQCA devices, our results are encouraging since they do not indicate any inherent fault intolerance of the antiferromagnetic ordering.

CHAPTER 9

DEMONSTRATION OF MQCA DEVICES

For the demonstration of MQCA devices we have fabricated a sample with 30 nm thick, elongated, polycrystalline permalloy dots of size 70 x 120 nm. Using ferromagnetic and antiferromagnetic ordering along dipole-coupled chains of nanomagnets, we designed inverter, wire, and majority logic functionality. The sample was tested by using a homogeneous external clock-field and the resulting magnetic configurations of our devices were imaged by MFM.

9.1 Antiferromagnetically-coupled chain as MQCA inverter or wire

An antiferromagnetically coupled chain of single-domain nanomagnets can be used to propagate and/or to invert binary information if an input is provided at one end of the chain. Inputs can be introduced by adding nanomagnets that are oriented along the external clock-field. Varying the position of such horizontally elongated nanomagnets, the first vertically elongated dot of the chain can be set by the input to either vertical up or vertical down magnetic states.

Figure 9.1 shows a fabricated chain with an input dot on the right end. Inversion, the basic digital operation is demonstrated in a physical area smaller than 0.07 μm^2. In this

particular chain, 15 inversions of the binary information are done by the time the ordering reaches the last dot on the left.

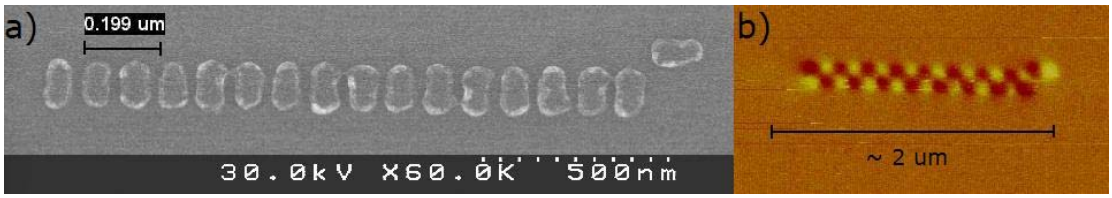

Figure 9.1 Antiferromagnetically-coupled chain of 16 dots with an additional input dot. (a) SEM, and (b) MFM image of the same chain that showed perfect ordering after demagnetization.

Figure 9.2 illustrates the simulated relaxation of a 16-dot long chain that was triggered by a horizontally oriented input dot on the left as the horizontally applied external magnetic field was reduced from 150 mT to 100 mT in one step. Fig. 9.2(a) to (q) are screen-shots of the time evolution.

The degree of ordering of the fabricated chains was investigated by means of micromagnetic simulations. Errors in the antiferromagnetic ordering (i.e. parallel moments of adjacent magnets) can occur when an undesired magnetization switching starts somewhere in the middle of a chain. This can happen if the applied clock-field changes too quickly, or if the switching-field distribution of the nanomagnets is too wide, i.e. they are not uniform.

The applied clock field is appropriate, if it is sufficiently strong to keep the dots magnetized along the hard magnetic axis when there is no other magnetic field present; but it is weak enough so that the dots can switch to one of their stable states if a local magnetic field appears in the direction of the easy axis. The triggering local field originates from the input dot, or from a switching neighboring dot. Appropriate clock

field can be applied readily by slowly decreasing a homogenous external field from a relatively large value. At the critical value, the ordering starts with the first dot driven by the input dot. The decreasing clock-field needs to be sufficiently slow to leave enough time for the ordering process.

Figure 9.3 illustrates faulty operation of the same chain that was introduced in the previous simulation (in Fig. 9.1). In this simulation, the faulty operation was caused by suddenly decreasing external field from 500 mT to 0 mT in one step. Figure 9.3(a) to (n) are screen-shots of the time evolution. As marked by the red lines in Fig. 9.3(d), in addition to the main ordering process propagating from the input, there are two other places in the chain where ordering processes initiate. 'Error' in the antiferromagnetic ordering occurs if the local ordering processes propagating against each other meet 'in the same phase'. As an example, see the dot in Fig. 9.3(i) marked by the red arrow. This nanomagnet maintains its 'null' state for longer time than any other in the chain, because it experiences opposite magnetizing (triggering) fields from its two neighbors. Finally, when it relaxes to one of its stable states, '0' or '1', it must align parallel with one of its neighbors, thus introducing an 'error'.

Even if the external clock-field is slow, undesired switching in the chain can start if the dots' properties vary too much, so different critical clock-field values are defined.

Figure 9.2 Simulated relaxation of an antiferromagnetically-coupled chain of nanomagnets shows as the switching propagates in time from (a) to (q) along the chain.

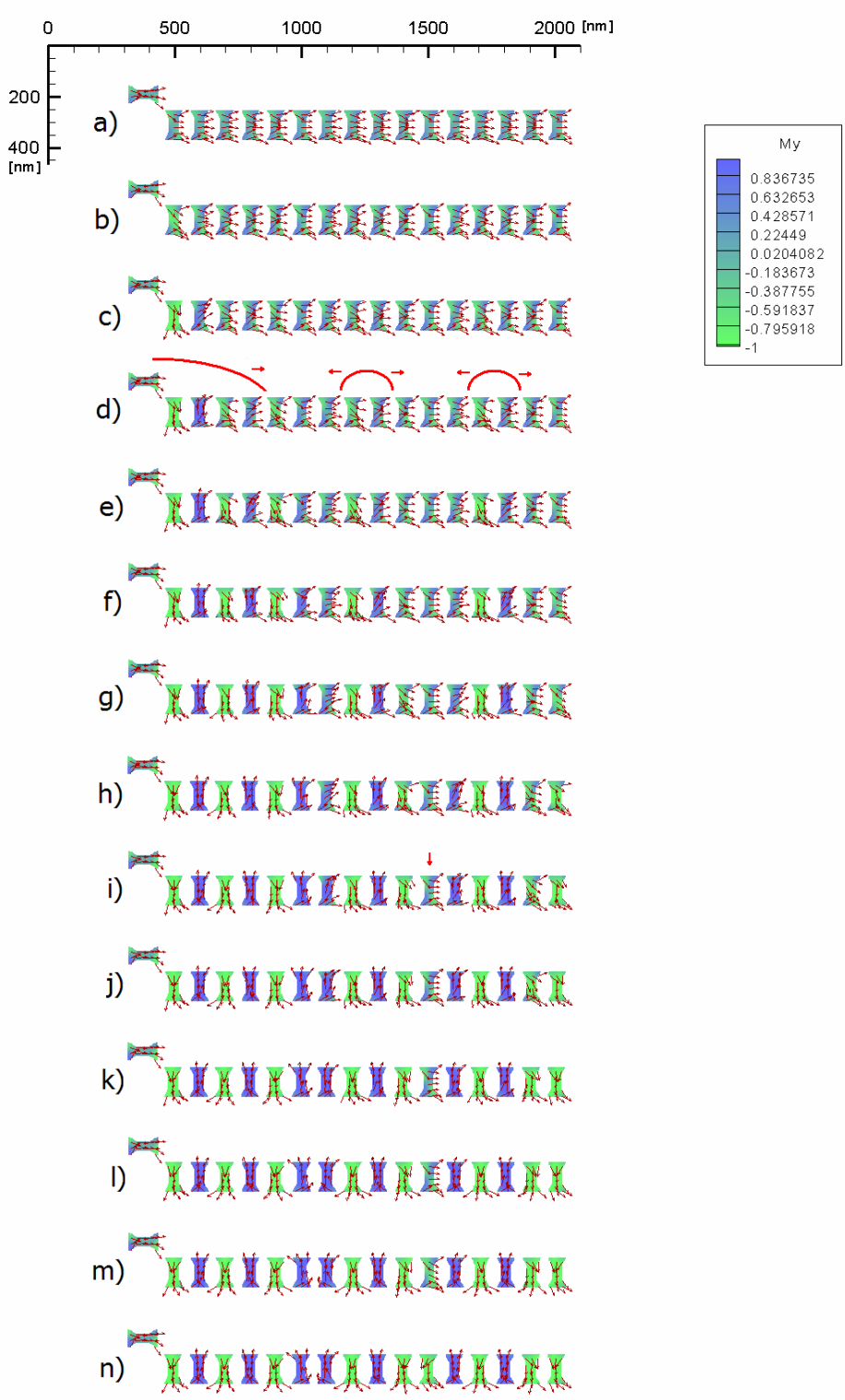

Figure 9.3 Simulated relaxation of an antiferromagnetically-coupled chain of nanomagnets shows that switching can start at multiple places in the chain. Time evolution is illustrated from (a) to (n).

Figure 9.4 demonstrates four 16-dot long antiferromagnetically-coupled chains, of which only one has a faulty, parallel aligned pair of dots, and the other three show perfect ordering. However, one cannot be sure that the ordering process was undisturbed in all three chains, since propagating local ordering processes can meet in opposite phase and remain unrevealed. For further investigation of the antiferromagnetic ordering along chains of nanomagnets, a high resolution, time-resolved measurement technique would be desired.

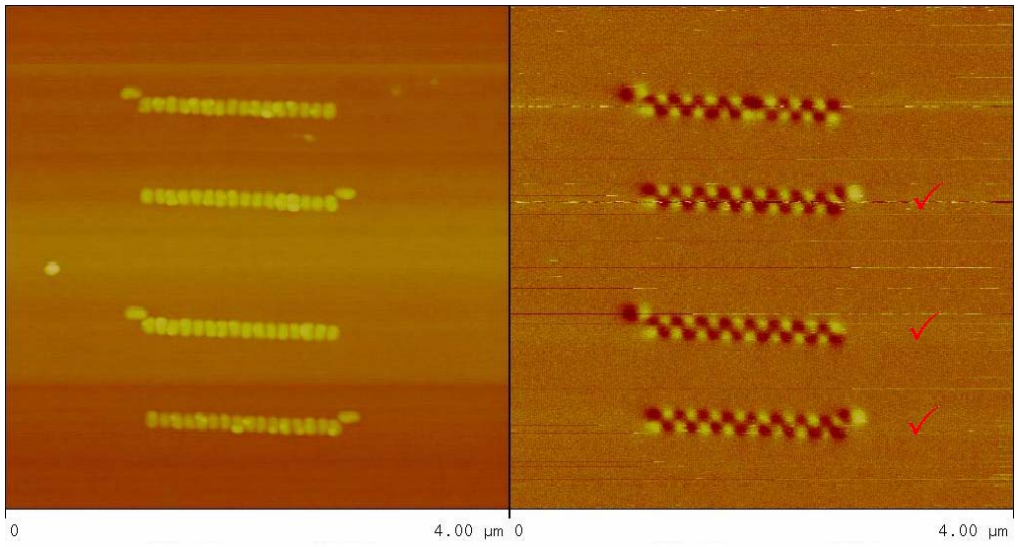

Figure 9.4 AFM and MFM images of four 16-dot long inverter chains, of which one shows error in the antiferromagnetic ordering, while the other three are errorless.

9.2 Ferromagnetically-coupled chain as MQCA wire

Nanomagnets that orient along their long axis in a chain couple ferromagnetically. This means that a perfectly ordered chain would have all nanomagnets pointing to the same direction along the chain. A ferromagnetically-coupled chain may be used for propagating information.

According to our experiments, ferromagnetically-coupled chains can be operated by external clock-field in the same manner as in case of the antiferromagnetically-coupled chains discussed before. Figure 9.5 demonstrates ordering as a result of a horizontally applied clock field.

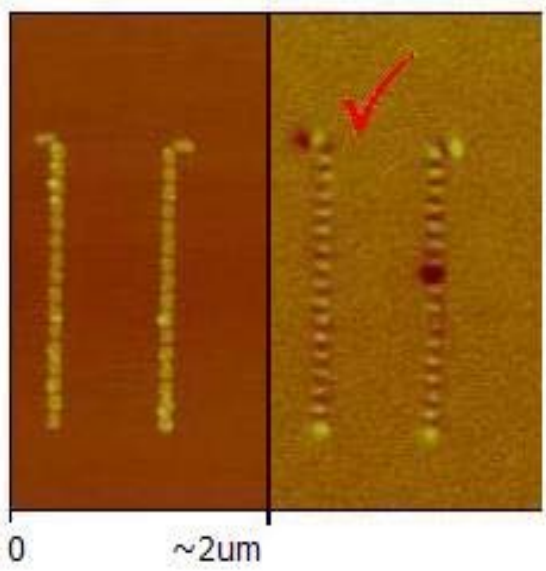

Figure 9.5 AFM and MFM image of two 16-dot long ferromagnetically-coupled chains with additional input dots. The chain on the left is ordered perfectly, while the chain on the right shows an error.

Note that the two coupling schemes do not perform exactly the same. Having the same separation (30 nm) between the dots, we observed, for example, a higher sensitivity of the ferromagnetically-coupled chains to clock-field misalignments. If the applied external clock field has a small component in the direction of the chain, it can overcome the effect of the input magnet and set the remanent magnetization direction in the chain.

9.3 Demonstration of MQCA majority logic operation

A planar majority gate using elliptical dots was proposed by Parish and Forshaw [60] for the first time. Their design is simply a cross of a ferromagnetically- and an antiferromagnetically-coupled planar wires, similar to the one shown in Fig. 9.6(b) that we propose. Consider, that the magnetic state of nanomagnets “A”, “B”, and “C” can be set by some inputs, and that a clock-field can allow the system to relax to its ground state. Then, majority logic operation can be performed by the central nanomagnet “M”, and the result can be transferred to another nanomagnet labeled as “out”. The binary values are assigned to the two stable magnetic states of the dots are referred to as A, B, C, M, and out, and the truth-table of the gate is introduced in Fig. 9.7. Because dot “B” is coupled antiferromagnetically to the middle dot, the majority function is performed on the binary values: negated B, A and C. Another negation appears during information propagation between the middle dot and the “out” dot, so the overall function of our cross-geometry can be represented by the schematic drawing in Fig. 9.6(c).

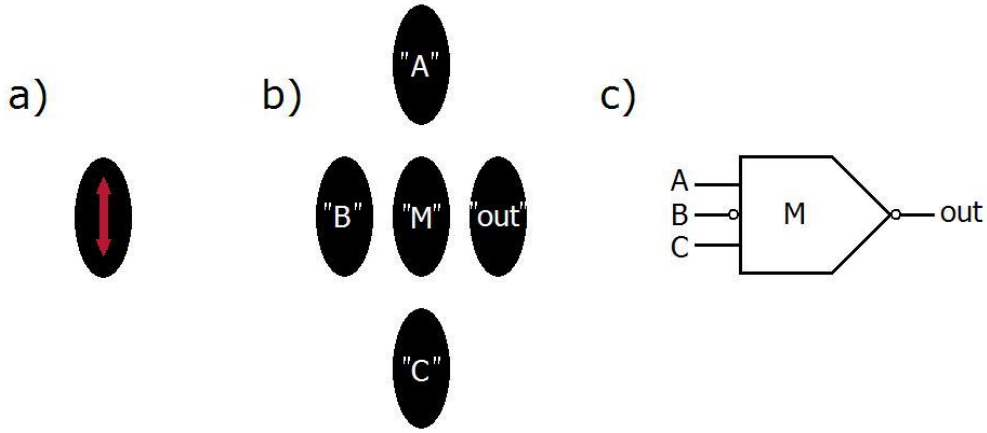

Figure 9.6 (a) An elongated polycrystalline NiFe alloy nanomagnet exhibits two stable magnetic states in the direction of its longest axis. (b) Majority gate geometry built up from elongated nanomagnets, and (c) its symbol.

A	B	C	$A\bar{B}C$	M	out	
0	0	0	0 1 0	0	1	if B=0 then out=NOR(A,C)
0	0	1	0 1 1	1	0	
1	0	0	1 1 0	1	0	
1	0	1	1 1 1	1	0	
0	1	0	0 0 0	0	1	if B=1 then out=NAND(A,C)
0	1	1	0 0 1	0	1	
1	1	0	1 0 0	0	1	
1	1	1	1 0 1	1	0	

Figure 9.7 Truth-table of the majority gate geometry.

Since the nanomagnets must be elongated in order to possess magnetic anisotropy, mixing of the two coupling schemes (ie. antiferromagnetic and ferromagnetic coupling) is inevitable in the plane, and it requires very careful gate design. Having the orientation of all the elongated nanomagnets kept the same in every subcircuit, however, provides the direction of the external clock-field to be defined uniformly throughout the whole system along the short axis of the dots.

Figure 9.8 demonstrates the cross-geometry. Dot ‘A’, the middle dot, and dot ‘C’ are coupled ferromagnetically, and their magnetization points alike in the MFM image. Dot ‘B’, the middle dot, and the dot ‘Out’ are coupled antiferromagnetically, and their magnetization points alternating in the MFM image. The image was taken after demagnetizing the sample.

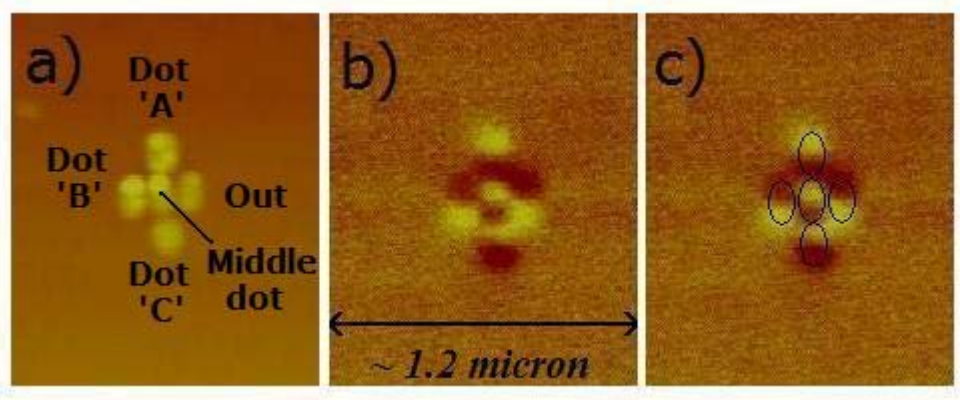

Figure 9.8 (a) AFM and (b) MFM image of a majority gate geometry fabricated without inputs. (c) is the same MFM image as (b) supplemented by black ellipses marking the location of the individual nanomagnets. This is a guide for the eye, and makes it easy to identify the two magnetic states of the dots.

The majority gate geometry was fabricated with approximately 25 nm dot-separation in the antiferromagnetically-coupled chain, and with approximately 35 nm dot-separation in the ferromagnetically-coupled chain. The difference was intended to balance the two coupling schemes, and to set approximately the same critical clock-field values for the two chains.

For further testing the majority gate geometry we added three input dots to the design that are able to determine the state of dots “A”, “B” and “C”. These additional nanomagnets have their magnetic easy axis oriented along the external clock-field (just as the ones we used for driving the chains), so their magnetic state is stable during the

operation of the gate. Varying the position of the input dots, the whole truth-table of the majority gate geometry can be tested. Figure 9.9 explains how the input dots affect the majority gate geometry.

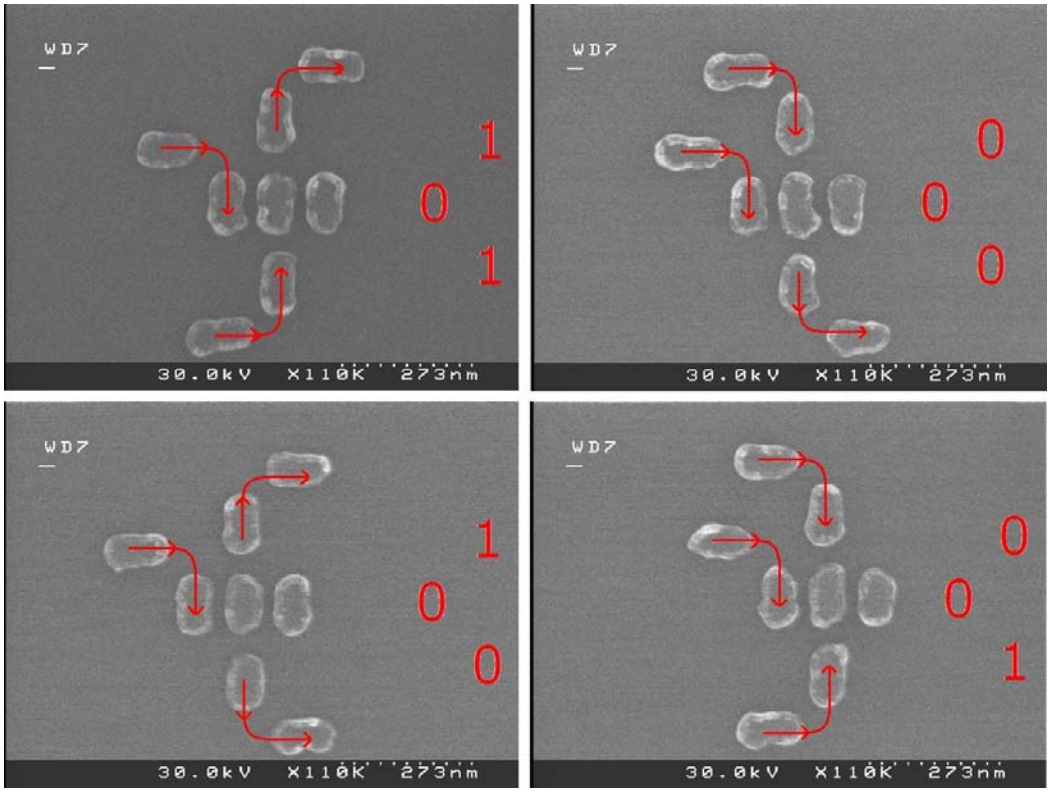

Figure 9.9 SEM micrographs of fabricated majority gate geometries providing four different inputs. The red arrows explain the effect of the horizontally oriented input dots assuming that the clock-field is applied horizontally to the right. The digital value '1' is assigned to the dot magnetization ↑, and '0' is assigned to ↓ in this figure.

The magnetic state of the gates was imaged after applying a horizontal clock-field of 500 Oersted with approximately 30 second rise and fall times. Simulations show that as the clock-field is reduced, the switching of the nanomagnets inside the gate begins at the input dots. The middle dot switches after "A", "B" and "C", and it is followed by the "out". Figure 9.10 summarizes the different MFM images that demonstrate the final

states of the majority gate operation for all the eight input combinations. The MFM data shows correct alignment of the magnetic moments in the images displayed here.

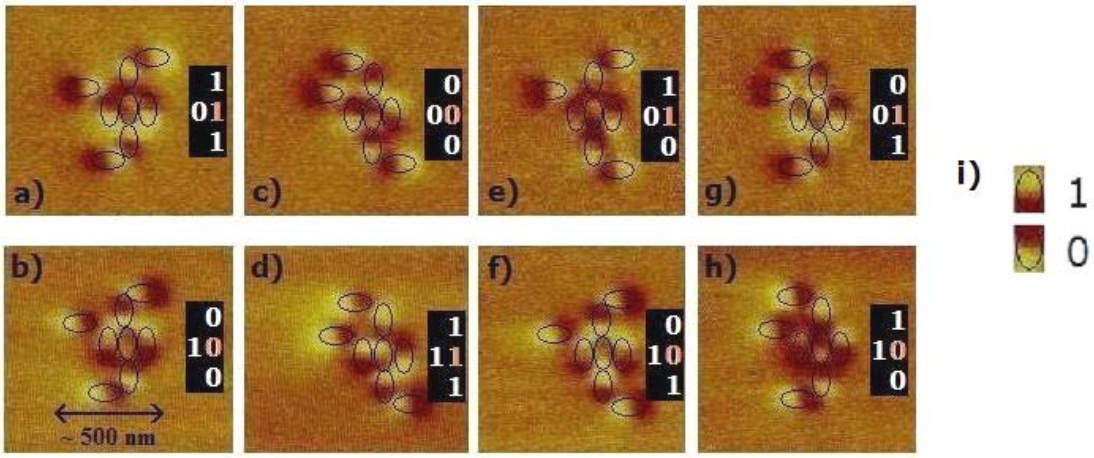

Figure 9.10 (a) - (h) MFM images of the magnetic state of majority gates fabricated by e-beam lithography and lift-off. The approximate location of the magnets is drawn superimposed on the MFM data. The clock-field was applied horizontally to the right for cases (a),(c),(e),(g) and to the left for (b),(d),(f),(h). The numbers in the black sub-windows correspond to the magnetic states of the three input dots and the middle dot, if the binary values are assigned to the magnetic states as shown in (i).

The following micromagnetic simulations are provided for the four different gate designs. The simulations were run on the bitmap file used for electron-beam lithography in the fabrication process. A cornered symmetric-shape nanomagnet was chosen as a building block to provide stronger coupling to the antiferromagnetically-coupled main chain [57]. Also, having the middle of the dots narrowed ensures a single-domain final state. The separations between the dots were chosen after several previous simulations. The material parameters were set for polycrystalline permalloy with 30 nm film thickness and 3 nm cell size. In all four cases, the gates were exposed to the same clock-field magnetization process, in which a horizontally applied external magnetic field was reduced from 500 mT to 0 mT in 50 steps. The switching of the central dot occurred at around 160 mT external field in all simulations.

Figure 9.11 illustrates the operation of the majority gate geometry that was designed for a 011 or a 100 input. Figure 9.11(a) shows that all three horizontal input dots align with the 500 mT external magnetic field, while the dots in the majority geometry are in the null-state. The operation starts below 200 mT applied field with the magnetization of dots "B" and "C" turning according the their inputs in Fig. 9.11(b). Dots "B" and "C" then try to align the central dot in the same direction, whence the central dot and dot "A" are switching to their final state at the same time together in Fig. 9.11(c). The output dot switches last in Fig. 9.11(d). Finally, Fig. 9.11(e) shows the relaxed magnetic state of the gate at the end of the clocking cycle.

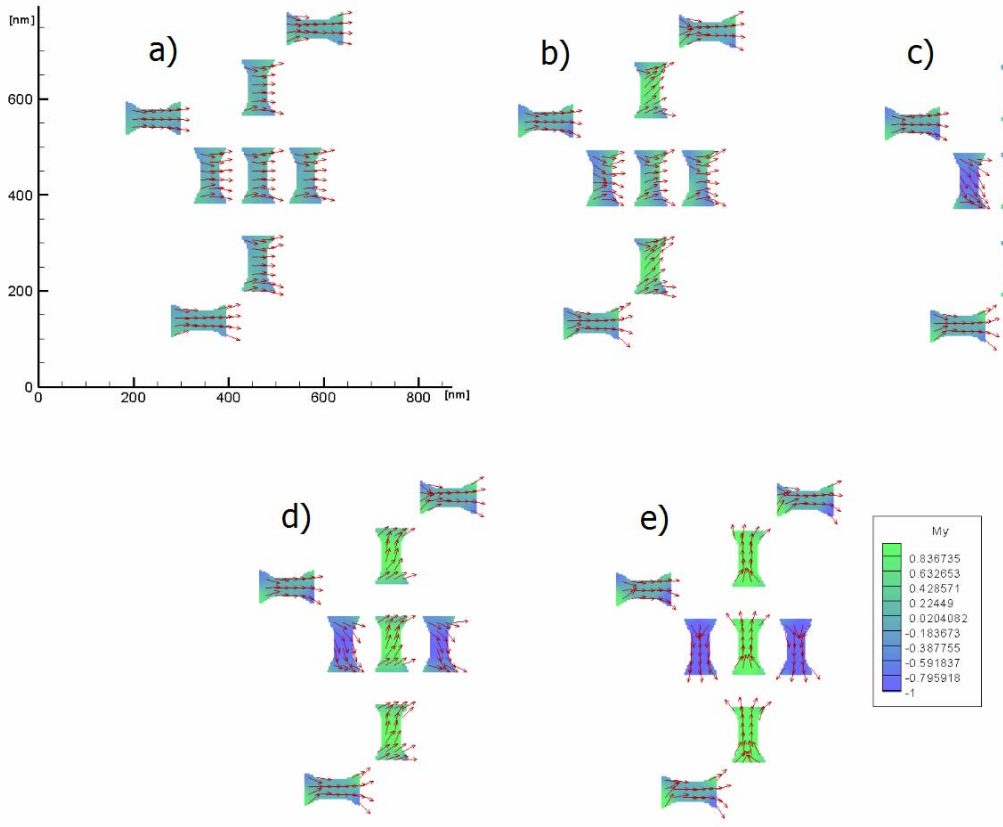

Figure 9.11 Simulated dynamics of the majority operation for the inputs (011) and (100). The figures from (a) to (e) show the time-evolution of the magnetic state of the gate as the external magnetic field ramps down from 500 mT (a) to zero (e).

Figure 9.12 illustrates the operation of the majority gate geometry that was designed for a 000 or a 111 input. Figure 9.12(a) shows that all three horizontal input dots align with the 500 mT external magnetic field, while the dots in the majority geometry are in the null-state. The operation starts below 200 mT applied field with the magnetization of dots “B” and “C” turning according the their inputs in Fig. 9.12(b). Dots “B” and “C” then try to align the central dot in the same direction, however in this case this is against the third input. As a result, dot “A” switches to its final state a little bit sooner than the central dot, this is also in Fig. 9.12(b). The output dot switches last in Fig. 9.12(d). Finally, Fig. 9.12(e) shows the relaxed magnetic state of the gate at the end of the clocking cycle.

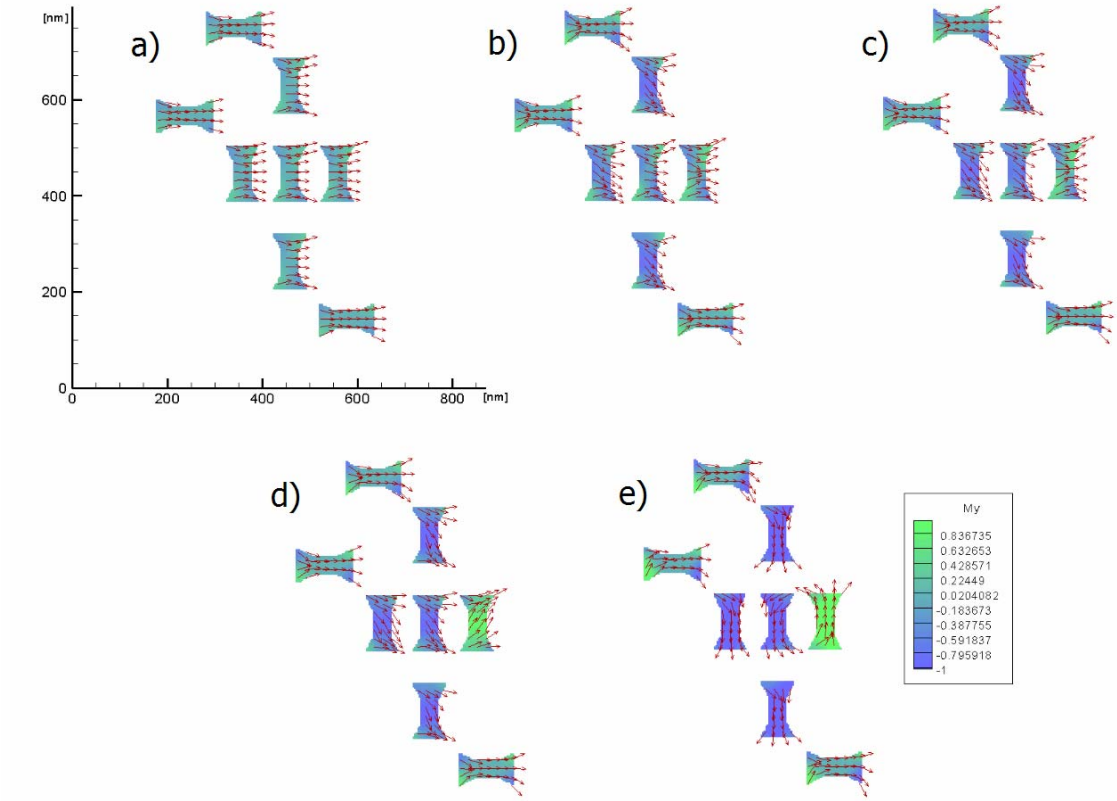

Figure 9.12 Simulated dynamics of the majority operation for the inputs (000) and (111). The figures from (a) to (e) show the time-evolution of the magnetic state of the gate as the external magnetic field ramps down from 500 mT (a) to zero (e).

Figure 9.13 illustrates the operation of the majority gate geometry that was designed for a 010 or a 101 input. Figure 9.13(a) shows that all three horizontal input dots align with the 500 mT external magnetic field, while the dots in the majority geometry are in the null-state. The operation starts below 200 mT applied field with the magnetization of dots "B" and "C" turning according the their inputs in Fig. 9.13(b). Dots "B" and "C" then try to align the central dot in the opposite direction, whence the central dot stays undecided. The switching of dot "A" according to its input occurs next in Fig. 9.13(c), followed by the central dot and the output dot in Fig. 9.13(d). Finally, Fig. 9.13(e) shows the relaxed magnetic state of the gate at the end of the clocking cycle.

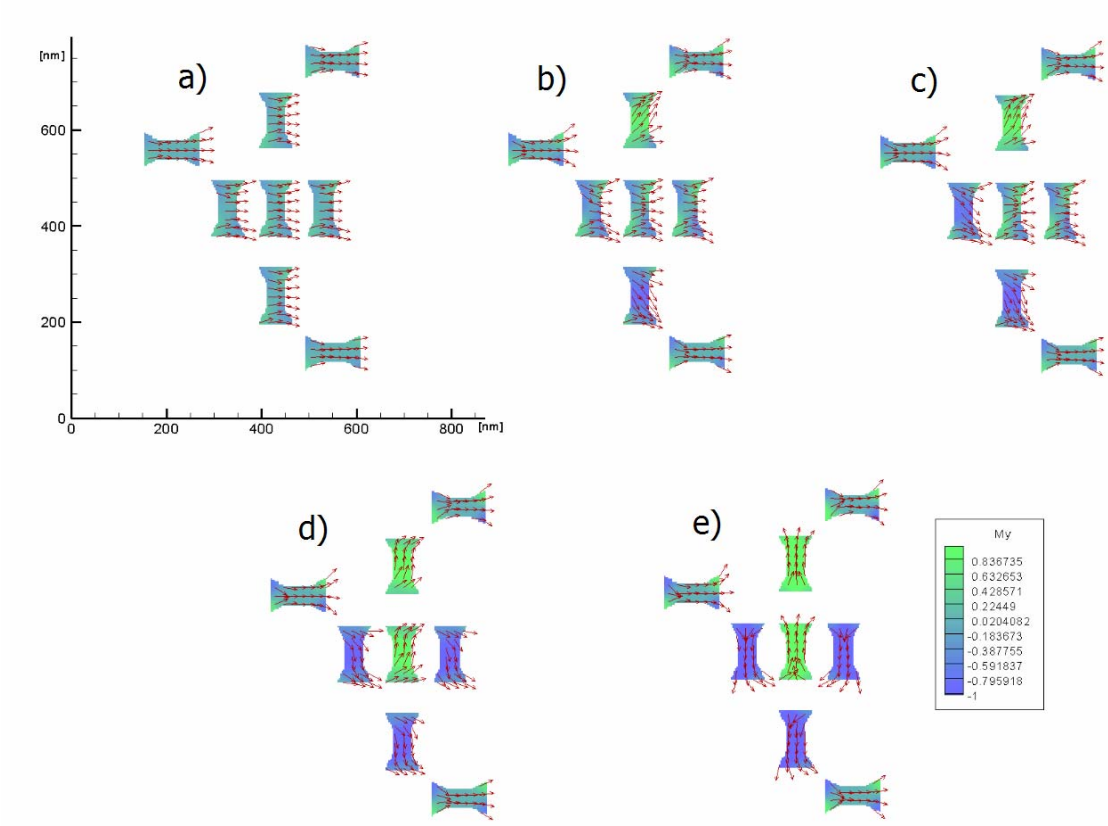

Figure 9.13 Simulated dynamics of the majority operation for the inputs (010) and (101). The figures from (a) to (e) show the time-evolution of the magnetic state of the gate as the external magnetic field ramps down from 500 mT (a) to zero (e).

Figure 9.14 illustrates the operation of the majority gate geometry that was designed for a 001 or a 110 input, which exhibits the same dynamic behavior as the previous gate in Fig. 9.13, except that dots “B” and “C” switch roles.

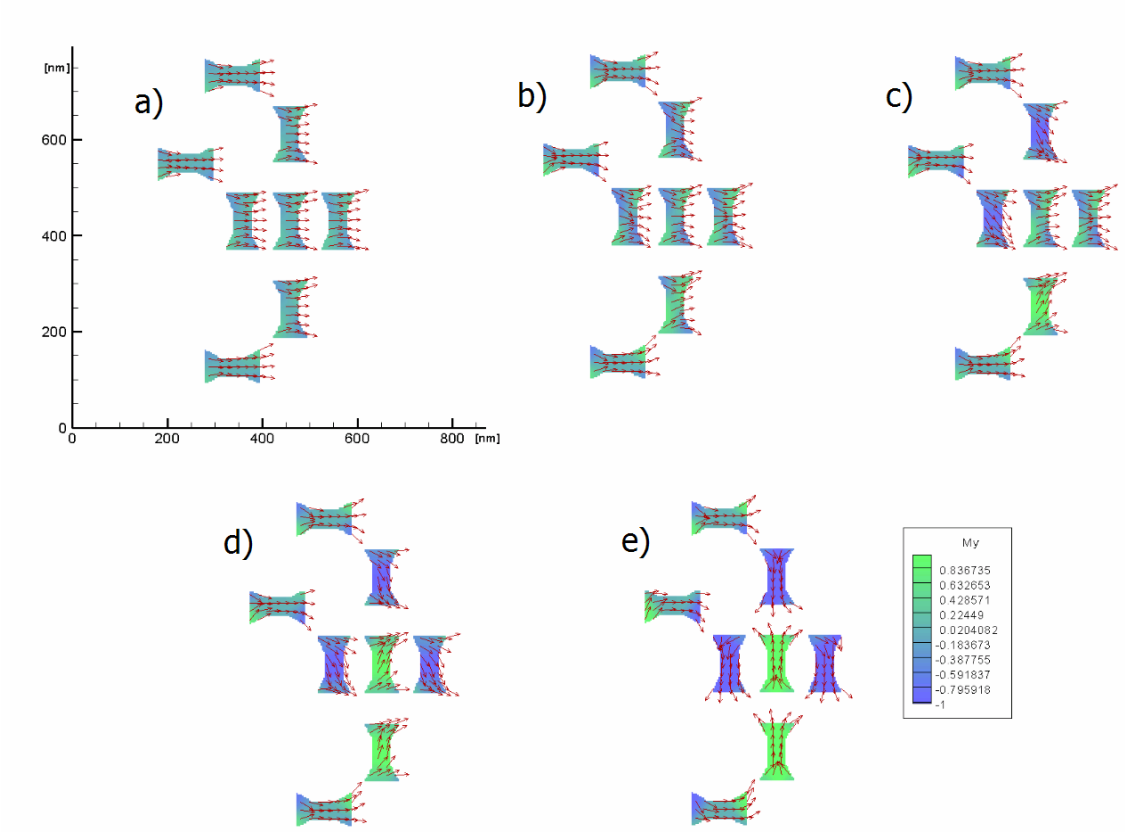

Figure 9.14 Simulated dynamics of the majority operation for the inputs (001) and (110). The figures from (a) to (e) show the time-evolution of the magnetic state of the gate as the external magnetic field ramps down from 500 mT (a) to zero (e).

The above OOMMF simulations estimate a switching time of 2 – 3 ns for reliable operation, which allows 200 MHz clock-field frequency considering a complete clock cycle to last for 5 ns. The clock frequency may be chosen even smaller, in order to minimize energy dissipation. Our theoretical studies on power dissipation and energy flow in the MQCA system was published in [61] and [62].

We demonstrated working majority gates. However there are critical requirements for the fabrication technology that need to be fulfilled in order to provide reliable nanomagnet circuits for mass production. In our experiment, 56 majority gates were tested, 14 of each input designs. Magnetic force microscopy images were taken after

many repeated, independent clock-field magnetizations of the sample. We found that approximately 25% of the gates were performing majority logic operation correctly, however those were working reliably. The low yield is most probably the result of our inadequate lithography control.

CHAPTER 10

SUMMARY

We introduced the concept of magnetic quantum-dot cellular automata (MQCA), which implements networks of field-coupled nanomagnets whose magnetization can be switched between two stable states. The nanomagnets are placed closely in arrays, so the ground state of the interacting system is ordered. An external time-varying magnetic field is applied to control the magnetic relaxation of the system to the ground state. The relaxation itself is used to propagate and process information. Logical functionality can be achieved at room temperature by certain physical arrangements of the nanomagnets.

Within this dissertation:

- Different fabrication techniques and different ferromagnetic material systems were investigated for application to MQCA.
- Different shapes of rings and elongated dots with flux-closure and quasi-single domain magnetization were investigated for reliable QCA operation.
- Dipolar ordering and correlation length of antiferromagnetically-coupled nanomagnet chains were studied with respect to the shape of the nanomagnets.
- Logic devices, such as inverter and majority gate featuring field-coupled nanomagnets were demonstrated.

APPENDIX

PUBLICATIONS

Results of the research that is presented in this dissertation were published in journal articles and conference manuscripts that are listed below:

JOURNAL PUBLICATIONS

A. Imre, G. Csaba, G. H. Bernstein, W. Porod, and V. Metlushko, "Investigation of shape-dependent switching of coupled nanomagnets," *Superlattices and Microstructures* **34,** 513-518 (2003).

A. Imre, G. Csaba, V. Metlushko, G. H. Bernstein, and W. Porod, "Controlled domain wall motion in micron-scale permalloy square rings," *Physica E* **19,** 240-245 (2003).

G. Csaba, **A. Imre**, G. H. Bernstein, W. Porod, and V. Metlushko, "Nanocomputing by field-coupled nanomagnets," *IEEE Trans on Nanotechnology* **1,** 209-211 (2002).

CONFERENCE PRESENTATIONS AND PUBLICATIONS

E. Horváth, **A. Imre**, A. L. Tóth, and W. Porod, "Patterning Magnetic Nanoobjects by FIB," poster to be presented at the XII International Conference on Electron Microscopy of Solids (EM'2005), Kazimierz Dolny, Poland, June 5-9, 2005.

A. Imre, G. Csaba, L. Ji, A. Orlov, G. H. Bernstein, V. Metlushko, and W. Porod, "Field-coupled nanomagnets for logic applications," to be presented at the Microtechnologies for the New Millennium 2005 Symposium, at the Nanotechnology conference (EMT103), Seville, Spain, May 9-11, 2005.

(Invited) **A. Imre**, L. Ji, G. Csaba, A. Orlov, G. H. Bernstein, and W. Porod, "Magnetic Logic Devices Based on Field-Coupled Nanomagnets," presented at the Second Conference on Nanoscale Devices & System Integration (NDSI 2005), Houston, Texas, April 4-6, 2005.

CONFERENCE PRESENTATIONS AND PUBLICATIONS (CONTINUED)

P. DasKanungo, **A. Imre**, B. Wu, A. Orlov, G. L. Snider, W. Porod, and N. P. Carter, "Gated Hybrid Hall Effect Device on Silicon," poster presented at the Fifth International Conference on Low Dimensional Structures and Devices (LDSD), Cancun, Mexico, December 2004.

A. Imre, G. Csaba, P. Lugli, G. H. Bernstein, V. Metlushko, and W. Porod, "Magnetic Logic Devices," presented at the Advanced Heterostructure Workshop, Kohala Koast, Hawaii, December 2004.

(Invited) G. H. Bernstein, **A. Imre**, V. Metlushko, A. Orlov, L. Zhou, L. Ji, G. Csaba, and W. Porod, "Magnetic QCA systems," presented at European Micro and Nano Systems 2004 (EMN04), ESIEE, Paris, France, October 2004.

E. Horváth, **A. Imre**, A. L. Tóth, and W. Porod, "Application of Focused Ion Beam Milling for Shaping Nanomagnets," poster presented at the 2nd Szeged International Workshop on Advances in Nanoscience, Szeged, Hungary, October 2004.

A. Imre, L. Zhou, A. Orlov, G. Csaba, G. H. Bernstein, W. Porod, and V. Metlushko, "Application of mesoscopic magnetic rings for logic devices," presented at the Fourth IEEE International Conference on Nanotechnology – IEEE-NANO 2004, Munich, Germany, August 2004.

A. Imre, G. Csaba, G. H. Bernstein, W. Porod, and V. Metlushko, "Shape Engineering of Dipole-Coupled Nanomagnets for Magnetic Logic Devices," poster presented at the 2004 Silicon Nanoelectronics Workshop, Honolulu, Hawaii, June 2004.

A. Imre, G. Csaba, L. Zhou, A. Orlov, G. H. Bernstein, W. Porod and V. Metlushko, "Shape Engineering of Dipole-Coupled Nanomagnets for Magnetic Logic Devices," poster presented at the 62nd Device Research Conference (DRC), University of Notre Dame, Indiana, June 2004.

A. Imre, G. Csaba, G. H. Bernstein, W. Porod, and V. Metlushko, "Shape Engineering of Dipole-Coupled Nanomagnets for Magnetic Logic," poster presented at the Metallic Multilayers Symposium, Boulder, Colorado, June 2004.

(Invited) V. Metlushko, U. Welp, V.Vlasko-Vlasov, G. Crabtree, M. Grimsditch, V. Novosad, J. Hiller, N. Zaluzec, P. Vavassori, B. Ilic, X. Zhu, P. Grütter, **A. Imre**, G. H. Bernstein, W. Porod, J. Bekaert, V. V. Moshchalkov, and Y. Bruynseraede "Magnetic Ring Devices for Memory and Logic Applications," IEEE Nanoscale Devices and System Integration (NDSI) 2004, Miami, February, 2004.

CONFERENCE PRESENTATIONS AND PUBLICATIONS (CONTINUED)

L. Zhou, **A. Imre**, G. Csaba, A. Orlov, G. H. Bernstein, and W. Porod, "Magnetoresistive Measurement of Patterned Nanomagnet Films," poster presented at the joint 6th International Conference on New Phenomena in Mesoscopic Structures and the 4th International Conference on Surfaces and Interfaces in Mesoscopic Devices – NPMS-6/SIMD-4, Maui, Hawaii, December 2003.

A. Imre, G. Csaba, A. Orlov, G. H. Bernstein, W. Porod, and V. Metlushko, "Investigation of Shape-Dependent Switching of Coupled Nanomagnets," presented at the joint 6th International Conference on New Phenomena in Mesoscopic Structures and the 4th International Conference on Surfaces and Interfaces in Mesoscopic Devices – NPMS-6/SIMD-4, Maui, Hawaii, December 2003.

G. Csaba, **A. Imre**, G. H. Bernstein, A. Csurgay, and W. Porod, "Circuit Simulations for Single-Domain Field-Coupled Nanomagnets," presented in the Special Session 'Nanoelectronic Circuits' at the European Conference on Circuit Theory and Design - ECCTD'03, Krakow, Poland, September 2003.

U. Welp, V. V. Vlasko-Vlasov, G. Crabtree, M. Grimsditch, V. Novosad, J. Hiller, N. Zaluzec, B. Llic, X. Zhu, P. Grutter, G. Csaba, **A. Imre**, G. H. Bernstein, W. Porod, J. Bekaert, V. Moshchalkov, Y. Bruynseraede, and V. Metlushko, "High-density Arrays of Magnetic Ring Elements," Third IEEE Conf. on Nanotechnology, San Francisco, California, August, 2003.

A. Imre, G. Csaba, A. Orlov, G. H. Bernstein, W. Porod, and V. Metlushko, "Investigation of Antiferromagnetic Ordering along Chains of Coupled Nanomagnets," presented at the IEEE International Conference on Nanotechnology – IEEE-NANO 2003, San Francisco, California, August 2003.

A. Imre, G. Csaba, V. Metlushko, G. H. Bernstein, and W. Porod, "Switching Behavior of Magnetically-Coupled Rings," poster presented at the 2003 Silicon Nanoelectronics Workshop, Kyoto, Japan, June 2003.

G. Csaba, **A. Imre**, G. H. Bernstein, V. Metlushko, and W. Porod, "Application of Magnetic Rings for Field–Coupled Computing," presented at the Fourth International Symposium on Nanostructures and Mesoscopic Systems (NanoMES), Tempe, Arizona, February 2003.

G. Csaba, **A. Imre**, G. H. Bernstein, W. Porod, and V. Metlushko, "Signal Processing with Coupled Ferromagnetic Dots," presented at IEEE-NANO' 2002, the Second IEEE Conference on Nanotechnology, Washington, D.C., August 2002.

CONFERENCE PRESENTATIONS AND PUBLICATIONS (CONTINUED)

G. Csaba, **A. Imre**, G. H. Bernstein, W. Porod, and V. Metlushko, "Nanocomputing by Field-Coupled Nanomagnets," poster presented at the 2002 Silicon Nanoelectronics Workshop, Honolulu, Hawaii, June 2002.

OTHER PUBLICATIONS

A. Imre, G. Csaba, G. H. Bernstein, and W. Porod, "Magnetic Quantum-dot Cellular Automata (MQCA)," chapter in "Quantum Cellular Automata: theory, experimentation and prospects," edited by Massimo Macucci, Imperial College Press, in press.

Publications related to the demonstration of the majority gates are in preparation.

BIBLIOGRAPHY

[1] C. S. Lent, P. D.Tougaw, W. Porod and G. H. Bernstein, "Quantum cellular automata," *Nanotechnology* **4**, 49 (1993)

[2] A. I. Csurgay, W. Porod, and C. S. Lent, "Signal processing with near-neighbor-coupled time-varying quantum-dot arrays," *IEEE Trans. On Circuits and Systems I* **47**, 1212 (2000)

[3] A. O. Orlov, I. Amlani, G. H. Bernstein, C. S. Lent, and G. L. Snider, "Realization of a functional cell for Quantum-dot Dot Cellular Automata," *Science* **277**, 928 (1997)

[4] I. Amlani, A. O. Orlov, G. Toth, G. H. Bernstein, C. S. Lent, and G. L. Snider, "Digital logic gate using Quantum-dot Cellular Automata," *Science* **284**, 289 (1999)

[5] R. K. Kummamuru, A. O. Orlov, R. Ramasubramaniam, C.S. Lent, G. H. Bernstein, and G. L. Snider, "Operation of a Quantum-dot Cellular Automata (QCA) shift register and analysis of errors," *IEEE Trans. On Electron Devices* **50**, 1906 (2003)

[6] C. S. Lent and B. Isaksen, "Clocked Molecular Quantum-dot Cellular Automata," *IEEE Trans. On Electron Devices* **50**, 1890 (2003)

[7] G. Csaba and W. Porod, "Simulation of Field-Coupled Architectures Based on Magnetic Dot Arrays," *Journal of Computational Electronics* **1**, 87 (2002)

[8] György Csaba, Alexandra Imre, Gary H. Bernstein, Wolfgang Porod, and Vitali Metlushko, "Nanocomputing by field-coupled nanomagnets," *IEEE Trans on Nanotechnology* **1**, 209 (2002)

[9] H. W. Gschwind, "Design of digital computers" © 1967 by Springer-Verlag, page 459-498

[10] http://www.sri.com/about/timeline/allmagnetic-logic.html

[11] A. Hubert and R. Schafer, *Magnetic Domains*, Springer- Verlag Berlin Heidelberg 1998.

[12] A. H. Eschenfelder, "Magnetic bubble technology" ©1980 by Springer-Verlag

[13] C. C. Faulkner, D. A. Allwood, M. D. Cooke, G. Xiong, D. Atkinson, and R. P. Cowburn, "Controlled switching of ferromagnetic wire junctions by domain wall injection," *IEEE Trans. Mag.* **39**, 2860 (2003)

[14] D. A. Allwood, G. Xiong, M. D. Cooke, C. C. Faulkner, D. Atkinson, and R. P. Cowburn, "Characterization of submicrometer ferromagnetic NOT gates," *Journ. Appl. Phys.* **95**, 8264 (2004)

[15] A. Ney, C. Pampuch, R. Koch, and K. H. Ploog, "Programmable computing with a single magnetoresistive element," *Nature* **425**, 485 (2003)

[16] R. P. Cowburn and M. E. Welland, "Room temperature magnetic quantum cellular automata," *Science* **287**, 1466 (2000)

[17] D. A. Allwood, Gang Xiong, M. D. Cooke, C. C. Faulkner, D. Atkinson, N. Vernier and R. P. Cowburn, "Submicrometer ferromagnetic NOT gate and shift register," *Science* **296**, 2003 (2002)

[18] György Csaba, "Computing with field-coupled nanomagnets," PhD dissertation, University of Notre Dame, 2004.

[19] Slaughter, J. M., Dave, R. W., DeHerrera, M., Durlam, M., Engel, B. N., Janesky, J., Rizzo, N. D. and Tehrani, S. "Fundamentals of MRAM technology," *Journ. Superconductivity* **15,** 19-25, (2002).

[20] Ross, C. A. "Patterned magnetic recording media," *Annu. Rev. Mater. Res.* **31,** 203-235 (2001).

[21] D. A. Thompson and J. S. Best, "The future of magnetic data storage technology," *IBM Journ. Res. Develop.* **44**, 311 (2000)

[22] C. T. Rettner, S. Anders, T. Thomson, M. Albrecht, Y. Ikeda, M. E. Best, and B. D. Terris, "Magnetic characterization and recording properties of patterned Co70Cr18Pt12 perpendicular media," *IEEE Trans. Mag.* **38**, 1725 (2002)

[23] G. Xiong, D. A. Allwood, M. D. Cooke, and R. P. Cowburn, "Magnetic nanoelements for magnetoelectronics made by focused-ion beam milling," *Appl. Phys. Lett.* **79,** 3461 (2001)

[24] C. A. Ross, M. Hwang, M. Shima, J. Y. Cheng, M. Farhoud, T. A. Savas, H. I. Smith, W. Schwarzacher, F. M. Ross, M. Redjdal, and F. B. Humphrey, "Micromagnetic behavior of electrodeposited cylinder arrays," *Phys. Rev. B.* **65**, 144417 (2002)

[25] O. Donzelli, D. Palmeri, L. Musa, F. Casoli, F. Albertini, L. Pareti, and G. Turilli, "Perpendicular magnetic anisotropy and stripe domains in ultrathin Co/Au sputtered multilayers," *Journ. Appl. Phys.* **93**, 9908 (2003)

[26] J. R. Barnes, S. J. O'Shea, M. E. Welland, J. Y. Kim, J. E. Evetts, and R. E. Somekh, "Magnetic force microscopy of Co-Pd multilayers with perpendicular anisotropy," *Journ. Appl. Phys.* **76**, 2974 (1994)

[27] T. Aoyama, K. Uchiyama, T. Kagotani, K. Hattori, Y. Wada, S. Okawa, H. Hatate, H. Nishio, I. Sato, "Fabrication and properties of CoPt patterned media with perpendicular magnetic anisotropy," *IEEE Trans. Mag.* **37**, 1646 (2001)

[28] V. F. Puntes, K. M. Krishnan, and A. P. Alivisatos, "Colloidal nanocrystal shape and size control: The case of cobalt," *Science* **291,** 2115 (2001)

[29] W-W Ma, Y. Yang, C-T Chong, A. Eggerman, S. N. Piramanayagam, T-J Zhou, T. Song, and J-P Wang, "Synthesis and magnetic behavior of self-assembled Co nanorods and nanoballs," *Journ. Appl. Phys.* **95,** 6801 (2004)

[30] J. J. De Yoreo and P. M. Dove, "Shaping crystals with biomolecules," *Science* **306,** 1301 (2004)

[31] M. Abe, T. Ishihara, and Y. Kitamoto, "Magnetite film growth at 30 degree C on organic monomolecular layer, mimicking bacterial magnetosome synthesis," *Journ. Appl. Phys.* **85,** 5705 (1999)

[32] C. J. Smith, M. Field, C. J. Coakley, D. D. Awschalom, N. H. Mendelson, E. L. Mayes, S. A. Davis, and S. Mann, "Organizing nanometer-scale magnets with bacterial threads," *IEEE trans. Magnetics* **34,** 988 (1998)

[33] J. Moritz, S. Landis, J. C. Toussaint, P. Bayle-Guillemaud, B. Rodmacq, G. Casali, A. Lebib, Y. Chen, J. P. Nozieres, and B. Dieny, "Patterned media made from pre-etched wafers: a promising route toward ultrahigh-density magnetic recording," *IEEE Trans. Mag.* **38**, 1731 (2002)

[34] S. Landis, B. Rodmacq, and B. Dieny, "Magnetic properties of Co/Pt multilayers deposited on silicon dot arrays," *Phys. Rev. B* **62**, 012271 (2000)

[35] E. Horváth, A. Imre, A. L. Tóth, and W. Porod, "Application of Focused Ion Beam Milling for Shaping Nanomagnets," poster presented at the 2nd Szeged International Workshop on Advances in Nanoscience, Szeged, Hungary, October 2004.

[36] http://www.microchem.com/products/pdf/PMMA_Data_Sheet.pdf

[37] J. S. Greeneich, *J. Electrochem. Soc.* **122**, 970 (1975)

[38] http://www.jcnabity.com/

[39] G. H. Bernstein, D. A. Hill and W. P. Liu, "New High-Contrast Developers for PMMA Resist," *Journ. Appl. Phys.* **71**, 4066 (1992)

[40] C. L. Dennis, R. P. Borges, L. D. Buda, U. Ebels, J. F. Gregg, M. Hehn, E. Jouguelet, K. Ounadjela, I. Petej, I. L. Prejbeanu, and M. J. Thornton, "The defining length scales of mesomagnetism: a review," *Journ. Phys.: Condensed Matter* **14**, R1175-R1262 (2002)

[41] J. M. D. Coey, "Materials for spin-electronics," *Lecture Notes in Physics* **569**, 277-297 (2001)

[42] Digital Instruments, "Magnetic Force Microscopy" *Support Note* **229**, page 2 (1996)

[43] G. Csaba, and W. Porod, "Restoration of magnetization distributions from joint Magnetic Force Microscopy measurements and micromagnetic simulations," *Journ. Cmputational Electronics* **2**, 225 (2003)

[44] M. J. Donahue and D. G. Porter, "OOMMF User's Guide, Version 1.0," *Interagency Report NISTIR 6376* http://math.nist.gov/oommf/

[45] J. Rothman, M. Kläui, L. Lopez-Diaz, C. A. F. Vaz, A. Bleloch, J. A. C. Bland, Z. Cui, and R. Speaks, "Observation of a Bi-Domain State and Nucleation Free Switching in Mesoscopic Ring Magnets," *Phys. Rev. Lett.* **86**, 1098 (2001)

[46] A. Imre, G. Csaba, V. Metlushko, G. H. Bernstein, and W. Porod, "Controlled domain wall motion in micron-scale permalloy square rings," *Physica E* **19**, 240 (2003)

[47] J. G. Zhu, Y. Zheng, and G. A. Prinz, "Ultrahigh density vertical magnetoresistive random access memory (invited)," *J. Appl. Phys.* **87**, 6668-6673 (2000)

[48] R. D. McMichael, and M. J. Donahue, "Head to head domain wall structures in thin magnetic strips," *IEEE Trans. Magn.* **33**, 4167-4169 (1997)

[49] Imre, A.; Zhou, L.; Orlov, A.; Csaba, G.; Bernstein, G.H.; Porod, W.; Metlushko, V.; "Application of mesoscopic magnetic rings for logic devices," Nanotechnology, 2004. 4th IEEE Conference on , 16-19 Aug. 2004 Pages:137 – 139

[50] R. P. Cowburn, "Magnetic nanodots for device applications (invited)," *Journ. Magnetism and Magnetic Materials* **242**, 505 (2002)

[51] B. D. Cullity, "Introduction to magnetic materials," Addison-Wesley Pub. 1972.

[52] U. Welp, V. K. Vlasko-Vlasov, G. W. Crabtree, J. Hiller, N. Zaluzec, V. Metlushko, and B. Ilic, "Magnetization reversal in arrays of individual and coupled Co-rings," *J. Appl. Phys.* **93**, 7056-7058 (2003)

[53] U. Welp, V. K. Vlasko-Vlasov, J. M. Hiller, N. J. Zaluzec, V. Metlushko, and B. Ilic, "Magnetization reversal in arrays of cobalt rings," *Phys. Rev. B.* **68**, 054408.1-8 (2003)

[54] R. P. Cowburn, A. O. Adeyeye, and M. E. Welland, "Controlling magnetic ordering in coupled nanomagnet arrays," *New Journ. Physics* **1**, 161 (1999)

[55] R. P. Cowburn, "Probing antiferromagnetic coupling between nanomagnets," *Phys. Rev. B* **65**, 092409 (2002)

[56] X. Zhu, P. Grutter, V. Metlushko, B. Ilic, "Micromagnetic study of electron-beam-patterned soft permalloy particles: technique and magnetization behavior," *Phys. Rev. B.* **66,** 024423 (2002)

[57] A. Imre, G. Csaba, G. H. Bernstein, W. Porod, and V. Metlushko, "Investigation of shape-dependent switching of coupled nanomagnets," *Superlattices and Microstructures* **34**, 513 (2003)

[58] Imre, A.; Csaba, G.; Bernstein, G.H.; Porod, W.; Metlushko, V., "Investigation of antiferromagnetic ordering along chains of coupled nanomagnets," Nanotechnology, 2003. IEEE-NANO 2003. 2003 Third IEEE Conference on , Volume: 1 , 12-14 Aug. 2003 Pages:20 - 23 vol.2

[59] Imre, A.; Csaba, G.; Ling Zhou; Orlov, A.; Bernstein, G.H.; Porod, W.; Metlushko, V., "Shape engineering of dipole-coupled nanomagnets for magnetic logic devices," Device Research Conference, 2004. 62nd DRC. Conference Digest, 21-23 June 2004 Pages:73 - 74 vol.1

[60] M. C. B. Parish and M. Forshaw, "Physical constraints on magnetic quantum cellular automata," *Appl. Phys. Lett.* **83**, 2046 (2003)

[61] G. Csaba, W. Porod, and A. I. Csurgay, "A computing architecture composed of field-coupled single domain nanomagnets clocked by magnetic field," *International Journ. Circuit Theory and Applications* **31**, 67 (2003)

[62] Csaba, G.; Lugli, P.; Porod, W.; "Power dissipation in nanomagnetic logic devices," Nanotechnology, 2004. 4th IEEE Conference on , 16-19 Aug. 2004 Pages:346 – 348